Ulm University Medical Center
Department of Internal Medicine II
Head: Prof. Dr. W. Rottbauer

Simulation and Prototyping of an X-Nuclei MR Coil

Dissertation to Obtain the Doctoral Degree
of Human Biology (Dr. biol. hum.)
of the Medical Faculty of Ulm University

Andreas Horneff
Heidelberg

2019

Acting Dean: Prof. Dr. rer. nat. Thomas Wirth
First Reviewer: Prof. Dr. rer. nat. Volker Rasche
Second Reviewer: Prof. Dr. rer. nat. Gerhard Glatting
Date of Graduation: 02.07.2020

Contents

Abbreviations

ASIC	Application Specific Integrated Circuit.
CEM	Computational Electromagnetic Method.
CMOS	Complementary Metal-Oxide-Semiconductor.
CND	Coil Noise Dominant.
CST-MWS	CST MICROWAVE STUDIO.
dB	Decibel.
EM	Electro-Magnetic.
EMF	Electromagnetic Field.
FID	Free Induction Decay.
FOV	Field of View.
GaAsFET	Gallium Arsenide Field-Effect Transistor.
GRE	Gradient Echo Sequenze.
iSNR	intrinsic Signal-to-Noise-Ratio.
LNA	Low Noise Amplifier.

MR	Magnetic Resonance.
MRI	Magnetic Resonance Imaging.
MRS	Magnetic Resonance Spectroscopy.
NEMA	National Electrical Manufacturers Association.
NF	Noise Figure.
NMR	Nuclear Magnetic Resonance.
NR	Non Resonant.
PCB	Printed Circuit Board.
PIN	Positive Intrinsic Negative.
PPM	parts per million.
PXIe	Peripheral Component Interconnect eXtensions for Instruments.
RF	Radio Frequency.
RMS	Root Mean Square.
ROI	Region of Interest.
Rx	Receive.
SAR	Specific Absorption Rate.
SND	Sample Noise Dominant.
SNR	Signal to Noise Ratio.
TEM	Transverse Electromagnetic.
TRL	Transmission Line.
TTL	Transistor-Transistor Logic.
Tx	Transmit.
Tx/Rx	Transmit/Receive.

Varactor Variable Capacitor Diode.

Abstract

Multi-nuclei imaging (X-nuclei Magnetic Resonance Imaging (MRI)) applications based on different nuclei such as carbon ^{13}C, fluorine ^{19}F, sodium ^{23}Na or phosphor ^{31}P, offers a wide-range of methods for studies of e.g. metabolic processes or non-^{1}H contrast agents. For this purpose, Radio Frequency (RF) coils with their resonance frequency adjusted to the different Larmor frequencies of the corresponding nuclei are required. In this thesis, a new approach of a X-nuclei receive chain (incorporating the RF coil and the Low Noise Amplifier (LNA), respectively) is introduced.

Therefore, a new simulation-based Magnetic Resonance (MR) coil design flow is introduced in this thesis as a basis for defining the requirements for the new X-nuclei receive chain. This design flow takes the entire MR imaging process into account and is validated using a manufactured prototype coil, whose Signal to Noise Ratio (SNR) performance was optimized based on the presented design flow, by comparing the coil's measured performance against the simulated results. Due to safety aspects, custom built coils can not be connected plug and play on a clinical MR system. To get around these limitations, a vendor independent receive-only system, which operates in parallel to an clinical MRI system (host system) is introduced. Comparing the afore mentioned simulation with corresponding measured results, the mean μ and the standard deviation σ of the relative error between the simulated and measured coil sensitivity pattern was found to be $\mu = 1.79\,\%$ and $\sigma = 3.15\,\%$, whereas the deviation between the simulated and measured voxel SNR was found to be less than $4\,\%$. This validates the proposed simulations-based design flow, since the simulations are in good accordance with the measured results.

Abstract

Based on the simulated requirements determined by the proposed design flow, a new approach towards a broadband X-nuclei receive coil in combination with an custom built high impedance Complementary Metal-Oxide-Semiconductor (CMOS) LNA is introduced. The resonance frequency of the proposed coil can be adjusted between 34 MHz and 104 MHz by integrated electronically switchable capacitor banks within a switching-time of 60 µs. The custom built CMOS LNA has a measured passband voltage gain of approximately 45 dB from a differential LNA input into a 50 Ω load. The lower and upper passband corner frequencies were measured as 1 MHz and 200 MHz, respectively. The measured Noise Figure (NF) of the setup was found to be less than 0.8 dB. The performance of the proposed setup was validated in hydrogen (61.0 MHz at 1.43 T and 42.6 MHz at 1.0 T) and fluorine (57.3 MHz at 1.43 T) imaging experiments by comparing against a state-of-the-art reference surface coil setup in combination with a low noise figure 50 Ω-LNA, tuned to a fix Larmor frequency. In these experiments, the mean and the standard deviation of the relative error between the coil sensitivity map of the reference setup and the proposed setup were found to be less than $\mu = 0.45\,\%$ and $\sigma = 1.2\,\%$, respectively. Furthermore, the SNR deviation between the reference setup and the proposed setup was found to be 7 %-10 %. Considering the high flexibility of the switchable coil, the slight reduction of the SNR while maintaining the sensitivity pattern appears acceptable.

Due to the proposed receive chain's topology, the SNR performance of the setup depends on the input referred voltage noise spectral density of the CMOS LNA. Using a revised CMOS LNA, the measured input referred voltage noise spectral density was improved from 900 pV/$\sqrt{\text{Hz}}$ to 200 pV/$\sqrt{\text{Hz}}$. This in turn results in an enhanced LNA NF of approximately 0.45 dB which is comparable to current used MRI LNAs.

1 Introduction

1.1 Motivation and Aim of this Thesis

MRI and Magnetic Resonance Spectroscopy (MRS) are well established techniques for the non-invasive preclinical and clinical assessment of disease progression. Over the past decade, with continuous advances in hardware, MR imaging of nuclei other than hydrogen has seen tremendous progress, allowing e.g. image-based cell tracking, monitoring of extracting targeted drug delivery and in monitoring of metabolic disease/processes [17, 11].

X-nuclei applications based on different nuclei such as carbon ^{13}C, fluorine ^{19}F, sodium ^{23}Na or phosphor ^{31}P, require RF coils with their resonance frequency adjusted to the different Larmor frequencies. For this purpose, double-tuned [15, 33] and triple-tuned [3, 49] RF coil designs have been proposed in the literature. These coils enable the acquisition of signals from different nuclei without changing between different hardware setups, which improves the co-registration and minimizes the patient manipulation [29]. Furthermore, the development and optimization of these X-nuclei (or naturally single tuned) RF coils and the design of the receive paths including the LNAs can be a challenging task, especially for an increasing number of measured nuclei. This results in the manufacturing of many hardware prototypes during the design process, until e.g. the coils' SNR in the corresponding Field of View (FOV), their penetration depth or their tuning and matching are optimized.

For this reason, an a priori prediction of the coils' performance and the entire receive chain would help to greatly economize and speed up the design and optimization process of RF coils. In spite of the fact that Computational Electromagnetic Methods (CEMs) based coil design flows including the calculation of e.g. B_1-field pattern [39], field homogeneity [32] or power requirements [28] are well known in literature, the simulation of the entire MR imaging process is not taken into account. Beside the development and design process of an RF coil, custom manufactured coils and particularly an entire custom manufactured X-nuclei receive chain can not be connected plug an play to any clinical MR system without hardware modifications, since every MRI vendor offers its own RF coils with special connectors/protocols and especially their own receive chain. This complicates their application and benchmarking.

The purpose of this thesis is to investigate the feasibility of a broadband X-nuclei receive chain to circumvent the limitations of current X-nuclei coil designs. As a part of this aim, a new simulation based RF coil design flow is introduced, taking into account the entire MR imaging process. The proposed design flow is validated using a manufactured prototype coil, whose performance was optimized regarding its SNR performance based on the presented design flow, by comparing the coil's measured performance against the simulated results. For interfacing the prototype coils to the clinical MR system, an independent receive-only system (receive chain and image acquisition system) which operates in parallel to a clinical MRI system is introduced.

Based on the simulated results by the new design flow, a broadband X-nuclei Receive (Rx) coil in combination with an custom built high impedance LNA is introduced. This receive chain is benchmarked against a single frequency receive chain by ^{1}H and ^{19}F MRI experiments at different field strengths.

1.2 Thesis Outline

Chapter 2 gives a brief introduction to MRI and the fundamental hardware of an MR system, as well as an introduction to MR coils, LNAs and image quality.

Chapter 3 gives a brief insight into the theory of X-nuclei imaging.

Chapter 4 gives a conclusion of the methods used in this work.

Chapter 5 to 8 contain the reprinted journal articles:

In Chapter 5 the new EM simulation based design flow for custom-built MR coils is proposed, which includes the full geometric and material properties of both the coil and the sample as well as the target MR sequences.

In Chapter 6 a new vendor independent receive-only system for image acquisition and benchmarking of custom built MR coils is introduced.

In Chapter 7 a new X-nuclei MR coil approach is introduced, based on an electronically tunable X-nuclei surface coil in combination with a high impedance broadband LNA.

Chapter 8 introduces the revised version of the LNA proposed in Chapter 7.

Chapter 9 summarizes the results of the reprinted publications whereas Chapter 10 discusses the results and gives an unified conclusion of the findings.

2 Theory

2.1 General aspects of Magnetic Resonance Imaging

In this chapter, a compact introduction to MRI physics, MR hardware and MR imaging is given. Detailed information of the principles and concepts of MRI can be found in [9, 31] and [8], which are also used as base references for this chapter. Notwithstanding that the principles of MRI are based on a quantum mechanical phenomenon, most of its processes can be described accurately applying classical mechanics assuming a large number of protons is considered [42]. Hence, this assumption is used in the following introduction.

2.1.1 Magnetic Resonance Imaging

MR Signal Generation and Image Contrast

MRI is an imaging technique that produces images of biological tissues, based on the Nuclear Magnetic Resonance (NMR) phenomenon. Every atom consists of an electronic cloud and an atomic nucleus, which consists of protons and neutrons. One quantum-mechanical property of these protons is their spin. MRI uses this quantum-mechanical property of nuclear spins for image generation. Every proton spin can be modeled as a microscopic magnetic moment, spinning around its own axis. Only atoms with an odd number of protons can be used for imaging, because this results in a non-zero nucleus spin, that can be measured outside the nucleus / the atom.

Hydrogen ^{1}H is the typical atom used for classical MR Imaging because it is abundant in the human body mainly in form of water and fat. Other useable atoms are e.g. carbon ^{13}C, fluorine ^{19}F, sodium ^{23}Na or phosphor ^{31}P.

Considering a spin ensemble consisting of a huge number of atoms which is exposed to an external magnetic field $\vec{B}_0 = (0, 0, B_0)^{\mathrm{T}}$ (vector oriented along the z-axis), the protons' spins are aligned parallel (spin-up) as well as antiparallel (spin-down) with respect to $\vec{B}_0$. Because of the lower energy state of the parallel orientation, the ratio is slightly towards this ratio which results in a net magnetization vector $\vec{M}_0 = (0, 0, M_0)^{\mathrm{T}}$ oriented in the direction of $\vec{B}_0$.

The maximum available magnetization M_0 is given by

$$M_0 = \frac{\rho\gamma^2\hbar^2 B_0}{4k_{\mathrm{B}}T_{\mathrm{sample}}}, \tag{2.1}$$

where ρ is the proton density, γ is the gyromagnetic ratio (e.g. for ^{1}H, $\gamma/2\pi = 42.56\,\mathrm{MHz/T}$ [31]), k_B is the Boltzmann constant, T_{sample} is the temperature of the sample and $\hbar$ is the reduced Planck constant ($\hbar = h/2\pi$).

The magnetization $\vec{M}_0$ precess about $\vec{B}_0$ with the Larmor frequency

$$\omega_0 = |\gamma \cdot B_0| \,. \tag{2.2}$$

The temporal evaluation of the magnetization vector $\vec{M} = (M_x, M_y, M_z)^{\mathrm{T}}$ is described by the Bloch equation as a function of time

$$\frac{d\vec{M}_{x,y}(t)}{dt} = \left(\vec{M}(t) \times \gamma\vec{B}(t)\right)_{x,y} - \frac{M_{x,y}(t)}{T_2}, \tag{2.3}$$

and

$$\frac{d\vec{M}_{z}(t)}{dt} = \left(\vec{M}(t) \times \gamma\vec{B}(t)\right)_{z} + \frac{M_0 - M_z(t)}{T_1}, \tag{2.4}$$

where the magnetic field $\vec{B}(t) = \vec{B}_{\mathrm{G}}(t) + \vec{B}_0$ consists of a static main field $\vec{B}_0$ and a time dependent magnetic field $\vec{B}_{\mathrm{G}}(t)$. T_1 is the tissue specific so-called longitudinal relaxation time, respectively, T_2 describing the tissue specific transverse relaxation time.

To rotate the magnetization $\vec{M}$ out of the z-direction into the transverse plane (xy-plane), a magnetic field $\vec{B}_1$ is used. This field rotates at the Larmor frequency and is aligned perpendicular to $\vec{B}_0$. The strength and the duration of $\vec{B}_1$ (usually called RF-pulse) defines the so-called flip angle α between $\vec{M}$ and the z-axis. In the following, an RF-pulse is assumed which results in a flip angle of $\alpha = 90°$ leading to a magnetization vector that rotates in the transverse plane. This rotating transverse magnetization (or rather the transverse component of the net magnetization, if $\alpha \neq 90°$) will have the potential to induce a detectable RF current in nearby conductors.

Figure 1 shows the net magnetization vector $\vec{M}$ of any spin ensemble, its longitudinal component M_z and its precessing transverse component $M_{x,y}$, which generates a time-varying magnetic field at the corresponding Larmor frequency. This in turn will induce a current in the coil which results in a voltage signal V_{s} which can be detected at the coil's terminals.

After the RF-pulse is applied, the system will return to thermal equilibrium and the longitudinal magnetization will be building up again. The relaxation of M_z over the time t is represented in Fig. 2 and can be described by:

$$M_z(t) = M_0 \cdot \left(1 - e^{-t/T_1}\right). \tag{2.5}$$

T_1 describes the tissue-dependent time until 63 % of the original longitudinal magnetization M_0 is recovered.

The reduction of the transverse magnetization M_{xy} over the time t can be derived by

$$M_{xy}(t) = M_0 \cdot e^{-t/T_2}, \tag{2.6}$$

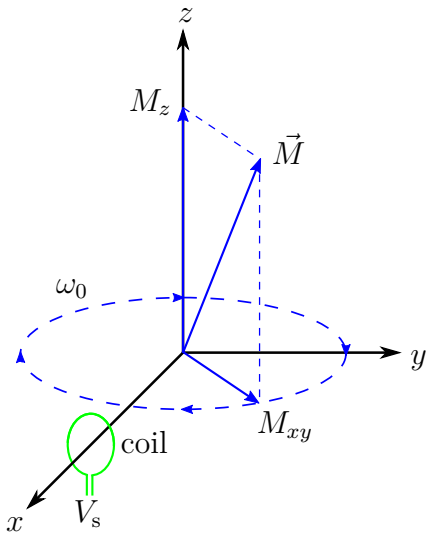

Figure 1: The transverse component M_{xy} of the net magnetization $\vec{M}$ is precessing at the Larmor frequency in a z-orientated static magnetic field. This induces a current into the coil (green) which results in a voltage signal V_s at the coil's terminals.

as illustrated in Fig. 2. In this case, T_2 describes the tissue-dependent time until the transverse magnetization decreases to 37 %. During the transverse and longitudinal relaxation, the magnetization vector $\vec{M}$ still precesses at the Larmor frequency and emits an Electromagnetic Field (EMF). Because of the proportionality of $M_{xy}(t)$ and the strength of the emitted EMF, the decay of this field is specific to the tissue-dependent parameter T_1 and T_2. This relation is the origin of contrast between tissues in MRI.

Signal localization

The base to create an MR image is the spatial location of single spin ensembles, which reflect e.g. the respective anatomical structures. This can be achieved by locally changes of the static $\vec{B}_0$-field. This results in a locally change of the Larmor frequency, which allows a spatial location.

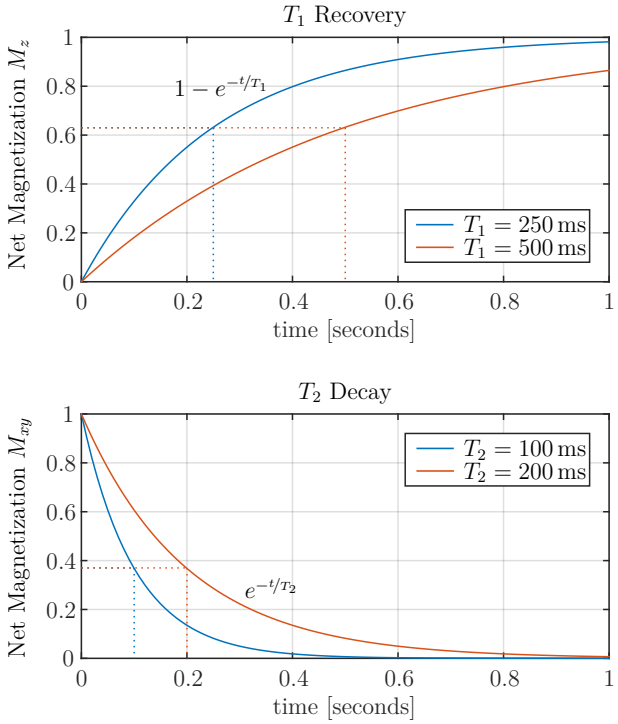

Figure 2: Example of two different M_z magnetization relaxation curves (T_1 recovery) and two M_{xy} magnetization relaxation curves (T_2 decay). The parameter T_1 as well as the parameter T_2 are tissue-dependent. Because of the magnetization's exponential relaxation, the function can be described by a single time constant, that is defined at the point $1 - 1/e = 63.2\,\%$ (T_1 recovery) or $1/e = 36.8\,\%$ (T_2 decay). This point is indicated by the dotted lines. Reprinted from [52] with permission from Stefan Wundrak.

Thus, special gradient coils are used to create a field linearly dependent on the location, which is also referred to as gradient field [5]

$$\vec{G} = \frac{dB_z}{dx}\vec{e}_x + \frac{dB_z}{dy}\vec{e}_y + \frac{dB_z}{dz}\vec{e}_z = (G_x, G_y, G_z)^{\mathrm{T}}\,, \tag{2.7}$$

which results in a locally variable magnetic field $\vec{B}_{\mathrm{G}}(r)$ that describes the variation of the z-component of the magnetic field for each location and is superimposed to $\vec{B}_0$, see Figure 3a. This locally changes the Larmor frequency which allows spatial encoding of the excitation an the received signal. The basic principles on how to achieve spacial

encoding in MRI were first introduced by Lauterbur and Mansfield in 1973 [19] [34] and is achieved in two steps:

1. Selection of a subvolume by using a "Slice Selection Gradient".
2. 2D or 3D spatial encoding of the selected subvolume by using a "Frequency Encoding Gradient" and a "Phase Encoding Gradient".

These gradients are explained in the next sections in detail.

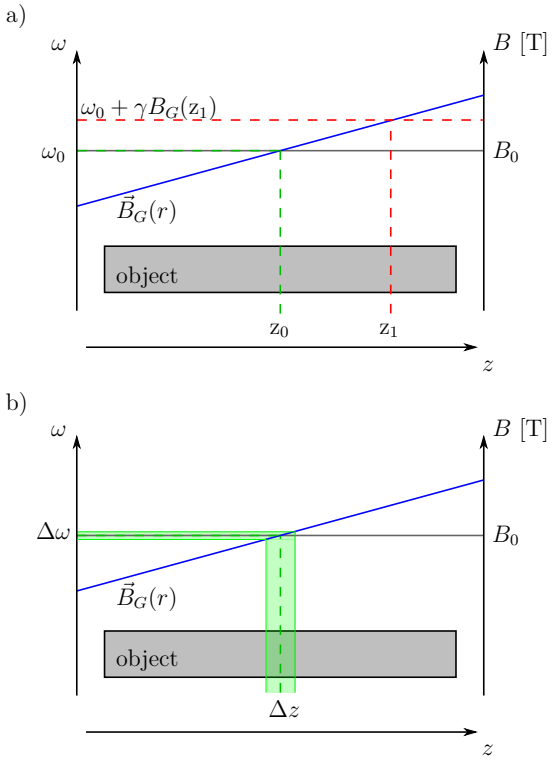

Figure 3: Schematic representation of a slice selection. (a) Superimposing a gradient $\vec{B}_G(r)$ to the B_0-field allows the spatial selection of a slice by variation of the excitation frequency ω because of the location dependent Larmor frequency in the object. (b) The width of the slice is achieved by the bandwidth $\Delta\omega$ of the excitation pulse.

Slice Selection Gradient

The aim of MRI is to create cross sections (or slabs) of an object (e.g. a human body) at different positions, as shown in Figure 3a. Therefor, a linear field gradient G_z is

superimposed to $\vec{B_0}$. The width of the slap must be adjustable. This could be achieved by adding a corresponding bandwidth $\Delta\omega$ to the center frequency ω_0, as illustrated in Figure 3b.

Dependent on the slope of the gradient and the bandwidth, the width of the slab can be adjusted, whereas the position is set by the center frequency. This allows the selective excitation of a subvolume (or slab) of the object.

Frequency Encoding Gradient

The spatial encoding of the selected sub-volume can be achieved by superimposing a linear gradient G_x in x-direction, which results in a spatially varying precessing frequency of

$$\omega(x) = \gamma G_x x. \tag{2.8}$$

The Frequency Encoding Gradient is applied during the read-out, which leads to a dephasing along the x-axis. The corresponding phase at position x and time t can be expressed by

$$\phi(x,t) = \int_0^t \omega(x,\tau)\,\mathrm{d}\tau = \gamma \int_0^t G_x(\tau) x\,\mathrm{d}\tau. \tag{2.9}$$

This can be expressed by the k-space notation. Therefor the time t is normalized to the substituted k_x by

$$k_x = \gamma \int_0^t G_x(\tau)\,\mathrm{d}\tau. \tag{2.10}$$

Equation 2.9 can be expressed in k-space notation as

$$\phi(x,k_x) = k_x x. \tag{2.11}$$

The measured signal of the FOV by the receiver coil is the integrated signal of all locations x of the object's transverse magnetization $m(x) = M_{xy}(x)$ described by the

complex one-dimensional signal equation

$$s(k_x) = \int_{\text{FOV}} m(x) e^{-i2\pi k_x x} \, \mathrm{d}x. \tag{2.12}$$

Phase Encoding Gradient

The second dimension y is encoded very similar to the frequency encoding. In comparison with frequency encoding, phase encoding is achieved by applying the gradient G_y for a short time span T after the excitation pulse, leading to a controlled dephasing along the y-axis. By using (2.9) (2.11), using T instead of t and k_y instead of k_x leads to

$$s(k_y) = \int_{\text{FOV}} m(x) e^{-i2\pi k_y y} \, \mathrm{d}y. \tag{2.13}$$

As k_y is time constant during readout, only one single phase shift will be acquired during each readout. Hence, for every different value of k_y the readout has to be repeated.

2.1.2 MR Hardware - Overview

Every MRI system is a mix of several subsystems that each provide necessary functionality to generate images of an object. A schematic illustration of a clinical MRI system is shown in Figure 4. The device consists of coaxial elements, where the outermost one is the superconductive magnet coil generating the static magnetic main B_0-field with a typically field strength between 0.5 T and 3.0 T for clinical use, which is uniform over the volume of interest. For human research studies, field strengths up to 9.4 T are used [48], with inhomogeneities of the order of a few parts per million (PPM) over a spherical volume of 50 cm in diameter. Since the main magnet does usually not generate sufficient homogeneity, shim-coils are frequently utilized inside the magnet. These shim-coils are used to superimpose additional magnetic fields, which improved the homogeneity of the B_0-field. In this way, the shims can be set to carry gradients which cancel the inhomogeneous components of the B_0-field [31].

Inside the superconductive magnet coil a set of three gradient coils is located, generating gradient fields for spatial encoding, which is superimposed upon the main field.

The innermost part of the MR system is the whole-body RF coil for spin excitation and detection. During spin excitation, several kilowatts of RF power can be driven into such a whole-body coil. To guarantee patient safety, the maximum RF field strength and deposited heat energy (Specific Absorption Rate (SAR)) are controlled by federal standards [1, 16]. When studying a defined anatomical region such as a knee, local Transmit/Receive (Tx/Rx)- or Rx-only coils are typically utilized for higher SNR.

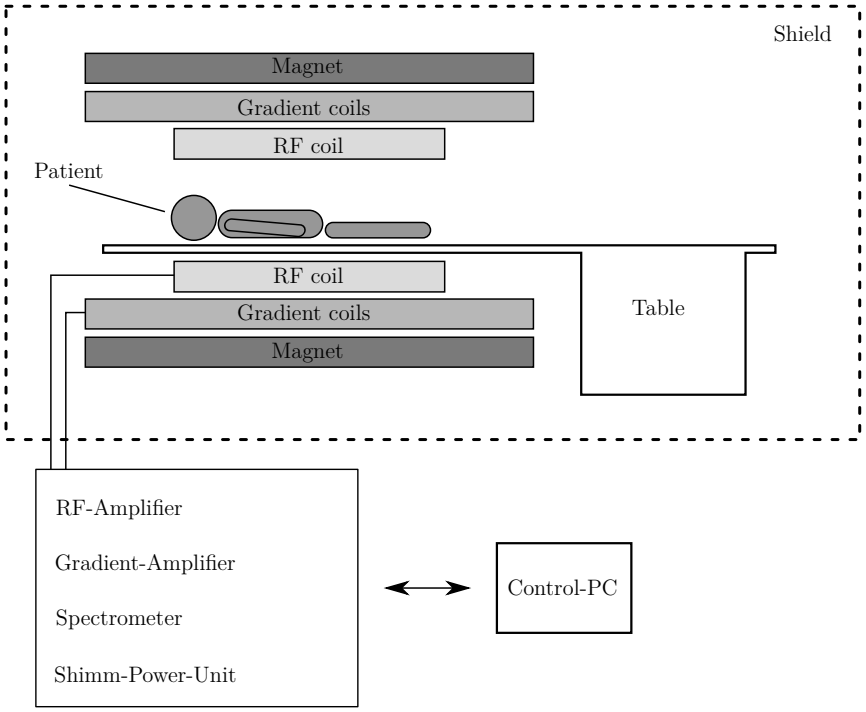

Figure 4: A schematic illustration of a clinical MRI system and a overview of its main electronic components.

MR RF coils and RF coil design

In general, RF coils (also known as RF resonators or RF probes) act like a broadcasting station: they transmit and receive signals. Thus, an RF coil can be carried out as a Transmit (Tx) coil, a Rx coil or both and the designs of constructions are multiple.

The combination of a transmit and receive coil in a single device can be useful for applications with X-nuclei MRI. Nevertheless, it represents a trade-off, since a separation of the two functionalities provides the advantage of individually optimizing the coil design in terms of the receive and the transmit function.

In general, the Tx coil generates the RF-pulse, whereas the Rx coil detects the precessing magnetization. Depending on e.g. the type of examination, the Region of Interest (ROI), the need for high SNR or the need for high uniformity of the transmitted field, a customized type of coil is needed. Thus, RF coils are typically application specific products, serving the needs of the point of use. Generally speaking, RF coils can be subdivided into two main categories: volume RF coils and surface RF coils.

Volume coils

Volume coils are placed at a certain distance to the surface of the sample and are used to cover a large volume. Due to their geometry, the main advantage of the volume coils is their very homogeneous transmit and receive sensitivity. The type of design depends on the range of application and is defined based on parameters as the anatomic coverage (diameter, length), requirement concerning the homogeneity, target Larmor frequency, and so on.

The main known designs are the birdcage coil and the Transverse Electromagnetic (TEM) coil. The birdcage coil was invented in the early 1980s and is typically used for field-strengths up to 3 T. In general, TEM coils can be used at any field strength but provide a number of advantages over other designs for 3 T and above [46].

Usually, in today's clinical MRI systems of almost every manufacturer, a large Tx/Rx volume coil (body-coil) is embedded inside the bore (cf. chapter 2.1.2).

Surface coils

In general, a surface coil design is based on a loop shape, which is in its simplest form for example a circular or a rectangular shape. In contrast to the volume coils, a surface coil is placed as close as possible to the ROI. Due to the geometry of the coil, the sensitivity near its surface is very high. This in turn results in a high SNR near the surface of the coil; nevertheless, the FOV and the penetration depth are reduced.

The FOV can be extended by combining more surface coils into an array. One major advantage of a surface coil is the flexibility, since the coil (coil array) can be placed on different positions within the bore, as long as the surface coil is aligned perpendicular to the main magnetic field.

2.1.3 RF transmission and reception

According to Ampere's law, a steady electric current produces a static magnetic field, which is described by [31]

$$\oint_C \vec{B}_1(t)\,\mathrm{d}l = \mu_0 I(t), \tag{2.14}$$

where C in an arbitrarily closed contour and $\mathrm{d}l = \hat{l}\mathrm{d}l$ with $\hat{l}$ denoting the unit vector tangential to C. Furthermore, the permeability of free space μ_0 is defined as $4\pi \times 10^{-7}\,\mathrm{H/m}$ and $I(t)$ is the total electric current passing through a wire (e.g. an RF coil) bounded by C.

To this end, the sensitivity of a coil can be described as

$$\vec{B}_\mathrm{u} = \frac{\vec{B}_1(t)}{I_\mathrm{coil}(t)}, \tag{2.15}$$

where $\vec{B}_1(t)$ is the magnetic field produced by the coil current $I_\mathrm{coil}(t)$.

This $\vec{B}_{\mathrm{u}}$ field can be decomposed into two counter rotating components $\vec{B}_{\mathrm{u}}^{+}$ and $\vec{B}_{\mathrm{u}}^{-}$. The $\vec{B}_{\mathrm{u}}^{+}$ component is referred to as the transmit[1] or excitation sensitivity of the coil, since it is the right circularly polarized component of the $\vec{B}_{\mathrm{u}}$-field, which rotates in a plane perpendicular to the static magnetic B_0-field. It can be expressed as

$$\vec{B}_{\mathrm{u}}^{+} = \frac{\vec{B}_{\mathrm{u},x} + i\vec{B}_{\mathrm{u,y}}}{2}, \tag{2.16}$$

where $\vec{B}_{\mathrm{u},x}$ and $\vec{B}_{\mathrm{u},y}$ are the x- and y-components of the $\vec{B}_{\mathrm{u}}$-field.

On the other hand, the $\vec{B}_{\mathrm{u}}^{-}$ component is the left circularly polarized component of the $\vec{B}_{\mathrm{u}}$-field. Based on the Principle of Reciprocity, it is referred to as the receive[1] sensitivity of the coil, which has to be used in calculations of received signal strength. It is defined by

$$\vec{B}_{\mathrm{u}}^{-} = \frac{\left(\vec{B}_{\mathrm{u},x} - i\vec{B}_{\mathrm{u,y}}\right)^{*}}{2}, \tag{2.17}$$

where the asterisk denotes a complex conjugate [26].

Spin excitation

As described in section 2.1.1, the net magnetization $\vec{M}$ must be perturbed from its equilibrium state, which is accomplished by an oscillation magnetic field generated by a Tx RF coil. Therefore, an RF-amplifier that is connected to the Tx coil generates the coil current $I_{\mathrm{coil}}(t)$ which results in a magnetic field $B_1(t)$. The angle between the magnetization vector and the main magnetic field is known as the flip angle α and is given by

$$\alpha = \int_0^{\tau} \gamma \vec{B}_u^{+} \cdot I_{\mathrm{coil}}(t)\,\mathrm{d}t, \tag{2.18}$$

where τ is the duration of the RF pulse. In reality, the flip angle across an image is not uniform, since it is affected significantly by e.g. off-resonance excitations, B_0

[1] Assuming a gyromagnetic ratio $\gamma > 0$

field inhomogeneities as well as inhomogeneities in the $\vec{B}_u^+$ field. These effects become particularly problematic as field strengths are increased up to 3.0 T and above.

Signal detection

After an RF pulse is applied, the rotating transverse component $\vec{M}_{xy}$ of the net magnetization $\vec{M}$ creates an electric field due to the changing magnetic flux. This in turn results in an induced electromotive force in a conductor loop (in that case a receiver coil, cf. Fig. 1) according to Faraday's law of induction. This induced electromotive force can be measured as a terminal voltage V_{signal} (which is also called Free Induction Decay (FID)) at the receive coil according to

$$V_{\text{signal}} = -\frac{\mathrm{d}}{\mathrm{d}t}\Phi_{\mathrm{A}}, \tag{2.19}$$

where Φ_{A} is the magnetic flux through the coil. It is denoted by

$$\Phi_{\mathrm{A}} = \int\limits_{\text{coil area}} \vec{B}\,\mathrm{d}\vec{A}, \tag{2.20}$$

where $\mathrm{d}\vec{A}$ is an infinitesimal vector element of the coil area.

By using Eq. (2.1) and (2.17), the absolute value of the induced voltage originating from a single voxel is given by [31]

$$V_{\text{signal,vox}} = \omega_0 \int\limits_{V_{\text{voxel}}} |B_{\mathrm{u}}^-| \cdot |M_0|\,\mathrm{d}V. \tag{2.21}$$

The signal picked by the receiver coil is then processed by the MRI system. While a transmitter coil must generate a rotating magnetic field as homogenous as possible, a receive coil must provide a high signal sensitivity at the Larmor frequency of the nucleus of interest.

2.1.4 MR coils – An RF resonator

In general, an RF coil is required to couple an electronic connection (a receiver / transmitter) to the EMF. A typical MR RF coil is designed as a resonant structure, which is tuned to the Larmor frequency of interest (cf. chapter 2.1.4 – *Tuning*). Thus, the resonance frequency of the coil depends on the nucleus under investigation as well as the B_0 field strength, similar to Eq 2.2.

RF coils are assembled as an oscillation circuit, according to the principle of an LCR tank. The inductance L is defined by the shape of the coil, since it results from the geometry of the conductor. In order to generate an oscillating current, a capacitor C is connected to the conductor in series or parallel. The resistance R is composed of losses inserted by the resistance of the conductor, the parasitical resistance of the capacitors and ohmic losses induced by the sample, what is described in detail in chapter 2.1.5 – *The loss mechanism.*

The impedance Z of the coil consists of a real and an imaginary part and is in its Cartesian form given as

$$Z = R + jX, \tag{2.22}$$

where R is the resistance of the RF coil and X is its reactance, which is in turn the sum of the capacitive and inductive reactances. X is defined by

$$X = X_{\mathrm{L}} + X_{\mathrm{C}}, \tag{2.23}$$

where

$$X_{\mathrm{L}} = \omega_0 L, \tag{2.24}$$

and

$$X_{\mathrm{C}} = -\frac{1}{\omega_0 C}. \tag{2.25}$$

Due to its setup, an MRI RF coil represents a series LCR circuit as illustrated in Fig. 5a. Resonance occurs if the reactance of the coil is zero ($X_{\mathrm{L}} + X_{\mathrm{C}} = 0$). From this

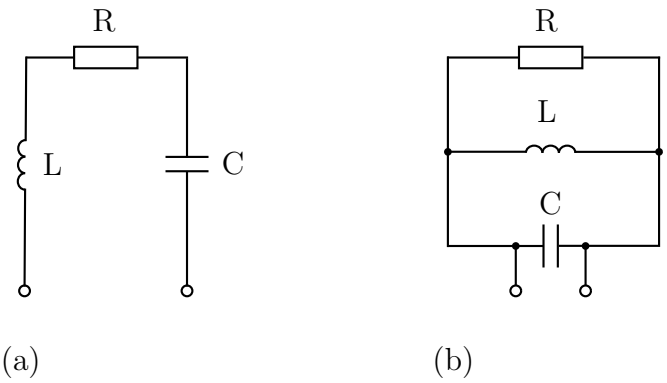

Figure 5: Different LCR circuits configurations. (a) represents a series LCR circuit, (b) represents a parallel LCR circuit.

assumption follows the resonance frequency f_{LC} of the coil, which is given by

$$f_{\mathrm{LC}} = \frac{\omega_{\mathrm{LC}}}{2\pi} = \frac{1}{2\pi\sqrt{LC}}. \tag{2.26}$$

Thus, at the resonance frequency, the impedance of the circuit is minimized and a purely resistive value, due to the associated resistance of the components inside the coil. This results in a maximum current. The energy inside the coil can be stored as magnetic energy in the conductor's inductance or as electric energy in the capacitor.

In contrast to a series LCR circuit, the impedance of a parallel LCR circuit (illustrated in Fig. 5b) is at its maximum at the resonance frequency. Due to this theoretical infinite impedance (which is reduced to a finite value in real circuits), the current flow is blocked. Therefore, parallel LCR circuits are popular detuning circuits (cf. chapter 2.1.4 – *Detuning – trap*).

Tuning

Since the geometry is given based on the coils specific requirements (which in turn defines the coils inductance L_{coil}), the resonance frequency f_{LC} is typically tuned by modifying C_{tune} to achieve $f_{\mathrm{LC}} \approx f_0$. This in turn boosts both the signal and the noise

level of the coil compared to the initially induced EMF and the coil noise level. The quantity of the amplification is defined by the quality factor Q of the resonant circuit, which is explained in a more detailed way in chapter 2.1.4 – *Quality factor*.

Moreover, RF coil elements longer than $\lambda/10$ start to radiate electromagnetic waves, which increases the loss compared to a low frequency inductor with only ohmic losses [47] (cf. chapter chapter 2.1.5 – *Sample loss*). In general, these losses can be reduced by splitting the coil into multiple segments using series capacitors (cf. Fig. 9, C_{coil}). The total capacitance C_{tot} of the coil can then be calculated by

$$C_{\text{tot}} = \frac{1}{\sum_{n=1}^{N} \frac{1}{C_n}}, \tag{2.27}$$

where N is the total number of capacitors mounted in the coil.

Detuning

Due to Faraday's law of induction (cf. chapter 2.1.3 – *Signal detection*), the EMF of one coil induces a current in other coils, placed near to each other. Assuming two coils tuned to the same Larmor frequency, e.g. a transmission coil and a Rx coil which are located close to each other, a current is induced in the Rx coil during transmission.

This in turn would result in a manipulation of the transmission B_1-field which will result in artifacts or in variation of the flip angle. To make matters worse, the induced RF current flowing in the receive coil can destroy parts of the receive chain, e.g. the LNA.
Conversely, the current induced in the Rx coil by the EMF of the MR signal results in an RF current flowing in the Tx coil, which on the other hand results in a decrease of the SNR.

Therefore, idle coils have to be switched off, which is called detuning. Detuning can be achieved in different ways, whereat detuning by means of Positive Intrinsic Negative (PIN)-diodes is the most popular way. As an example of the theory of operation, two different PIN-diode detune techniques (series PIN-diode, trap) are illustrated in Fig. 6. In this connection, a PIN-diode can be assumed as an RF switch. It is switched to its "on" state, while the PIN-diode is forward biased by a DC current and to its "off" state, while the PIN-diode is reverse biased.

Detuning – series PIN-diode

A PIN-diode can be used as a simple on/off switch, when implemented in series inside the coil, which is schematically illustrated in Fig. 6a(i). In this illustration, the two inductors L_1 and L_2 act as RF chokes.
In this configuration, the coil is tuned (switch to its "on" state) if the PIN-diode is forward biased. Since a PIN-diode can not be assumed as an ideal switch, it behaves like a small resistor, while the PIN diode is forward biased (cf. Fig. 6a(ii)). Naturally, the resistance depends on the used type. The PIN-diode (MADP-000235-10720T, MACOM, Lowell, USA) used in the work presented at the next chapters has a "on" resistance of $R_{\mathrm{PIN}} \approx 0.5\,\Omega$.

Assuming a reverse biased PIN-diode, the PIN-diode represents a small capacitor[2] of only a few pico farad. Using Eq. (2.22), this capacitor adds up to a resistor of a few kilo Ohm, located in series within the coil. Thus, the coil is switched to its "off" state, cf. Fig. 6a(iii).

The main advantage of this detuning method is the very simple design and its broadband capability. Nevertheless, this type of active detuning is more suitable for Tx coils, due to the SNR drop caused by the resistance of the forward driven PIN-diode.

[2] According to its datasheet, the capacitance of the used MADP-000235-10720T PIN-diode is $C_{\mathrm{PIN}} \approx 1.2\,\mathrm{pF}$

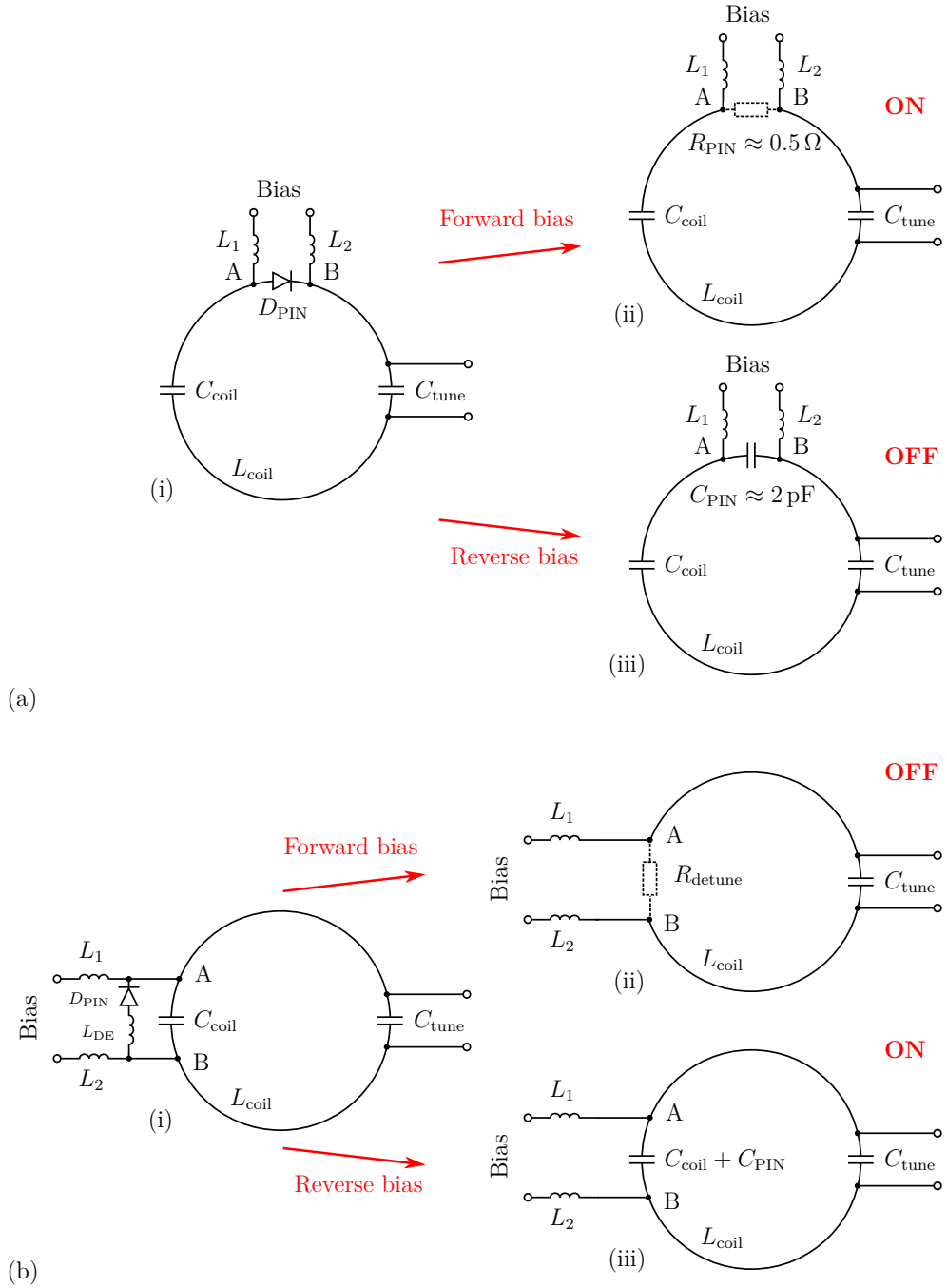

Figure 6: Illustration of two common PIN-diode detuning methods. (a) Schematic illustration of a coil detuning using a PIN-diode in series with the coil (popular in Tx coils) and (b) a coil detuned using a PIN-diode trap (popular in Rx coils).

Detuning – trap

Another common type of an active PIN-diode detuning circuit is illustrated in Fig. 6b(i). Here, a PIN-diode in series with an inductor (L_{DE}) is set in parallel to a capacitor of the coil (C_{coil}).

If the PIN-diode is forward biased, this configuration forms a parallel LC circuit. By using Eq. (2.26), L_{DE} is determined in a way that the resonance frequency of the detuning circuit is set to the Larmor frequency. Since the impedance of a parallel LC circuit is at its maximum at the resonance frequency (cf. chapter 2.1.4 – *MR coils – An RF resonator*), the coil is switched to its "off" state, cf. Fig. 6b(ii).

In contrast, if reverse biased, the capacitance of the PIN-diode C_{PIN} is in parallel with the capacitor of the coil, resulting in a $C_{\mathrm{coil}'} = C_{\mathrm{coil}} + C_{\mathrm{PIN}}$, as illustrated in Fig. 6b(iii).

Compared to the detuning by a PIN-diode in series, the lossy PIN-diode is not part of the coils LCR circuit. Hence, the SNR is not affected if the PIN-diode is reverse biased, thus this detune circuit is basically used in Rx coils. The design of the detuning trap is cumbersome compared to the PIN-diode used in series. Another disadvantage is the frequency selective property of this detune circuit.

Quality factor

The quality factor Q is a dimensionless parameter, describing how underdamped an RF coil is. Thus, a higher Q-factor indicates a lower rate of energy loss relative to the stored energy of the coil. The Q-factor of an unloaded RF coil is given by

$$Q_{\mathrm{u}} = \frac{\omega_0 \cdot L_{\mathrm{coil}}}{R_{\mathrm{coil}}}, \tag{2.28}$$

where R_{coil} are the resistive losses of the coil (cf. chapter 2.1.5 – *Resistive loss*). Accordingly, the Q-factor of a loaded coil can be calculated by

$$Q_{\text{l}} = \frac{\omega_0 \cdot L_{\text{coil}}}{R_{\text{loss}}}, \tag{2.29}$$

where R_{loss} are the resistive losses of the coil and the losses induced by the sample (cf. chapter 2.1.5 – *The loss mechanism*).

In the case where Q_{u} is dominated by ohmic losses and Q_{l} is dominated by electromagnetic losses induced through inductive coupling to the sample (according to chapter 2.1.5 – *Resistive loss* and chapter 2.1.5 – *Sample loss*), Q_{l} can be written as [21]

$$Q_{\text{l}} = \frac{\omega_0 \cdot L_{\text{coil}}}{a\,\omega_0^2 + b\,\sqrt{\omega_0}}, \tag{2.30}$$

where a and b are constants quantifying the amount of resistance due to inductive coupling and due to the coil itself, respectively.

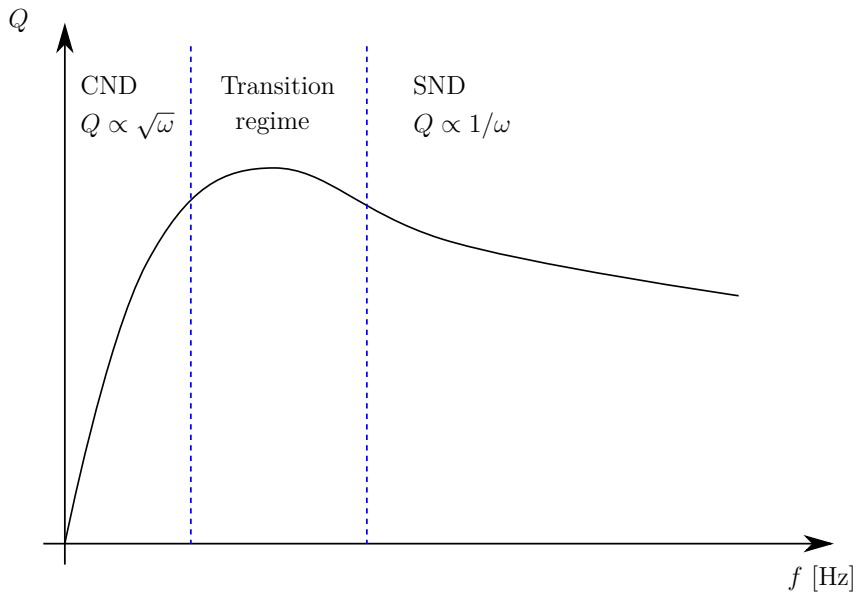

Figure 7: A theoretical curve of the quality factor Q as a function of frequency f, divided into the Coil Noise Dominant (CND) regime, the transition regime and the Sample Noise Dominant (SND) regime. Modified from [21], copyright © 2008 Wiley Periodicals, Inc.

The qualitative behavior of Q as a function of frequency is plotted in Fig. 7. At low frequencies, the ohmic losses of the coil are dominant compared to the electromagnetic sample losses. This is called the Coil Noise Dominant *(Coil Noise Dominant (CND))* regime, since the term $b\sqrt{\omega_0}$ is dominant. With increasing frequency, in the transition regime, the ohmic losses and the electromagnetic losses are approximately equal distributed. At high frequencies, the sample losses are dominant. This in turn is called the Sample Noise Dominant *(Sample Noise Dominant (SND))* regime, whereat the term $a\,\omega_0^2$ is dominant [21].

The loading factor LF of a coil can be determined by measurements of Q by

$$\mathrm{LF} = 1 - \frac{Q_\mathrm{l}}{Q_\mathrm{u}} \tag{2.31}$$

and results by using Eq. (2.28) and Eq. (2.29) in

$$\mathrm{LF} = 1 - \frac{R_\mathrm{coil}}{R_\mathrm{coil} + R_\mathrm{sample}}. \tag{2.32}$$

Thus, the loading factor provides a convenient tool for estimating the relative contributions of the coil and sample resistance:

$$IF = \begin{cases} 0 & R_\mathrm{sample} \ll R_\mathrm{coil} \\ 0.5 & R_\mathrm{sample} = R_\mathrm{coil} \\ 1 & R_\mathrm{sample} \gg R_\mathrm{coil} \end{cases} \tag{2.33}$$

The crossover between a coil dominated resistance and a sample dominated resistance (and thus a coil dominated or sample dominated noise, respectively) is indicated by $IF = 0.5$.

Since both, the signal as well as the noise are boosted by the resonant RF coil, the total Root Mean Square (RMS) noise voltage $V_{\mathrm{n,tot}}$ (cf. Eq. (2.46)) can be written as

$$V_{\mathrm{n,tot}} = \left(\frac{Q_{\mathrm{l}}}{2}\right) \cdot \sqrt{4\, k_{\mathrm{B}}\, T\, \left(R_{\mathrm{coil}} + R_{\mathrm{sample}}\right)\, \Delta f}. \tag{2.34}$$

LNA

As illustrated in Fig. 4, most active hardware components of an MRI system are located outside the shielded MR scanner room to reduce any interferences. Since the RF coil has to be located as near as possible to the ROI, the connection line between the spectrometer and the coil has a length of several meters.

To enable an effective transmission of the induced EMF, the coil is connected to a LNA (or preamplifier), which is located as near as possible to the coil to reduce additional signal losses. The task of a LNA is the amplification of a very low-power signal without significantly degrading its SNR. An amplifier always increases both, the power of the input signal as well as the input noise. Even though low-noise components are typically used in LNA designs, every amplifier decreases the SNR by its noise factor F (due to the inherent noise of the LNA) which is defined by [53]

$$F = \frac{\mathrm{SNR_{in}}}{\mathrm{SNR_{out}}}, \tag{2.35}$$

where $\mathrm{SNR_{in}}$ is the signal-to-noise-ratio at the input of the LNA and $\mathrm{SNR_{out}}$ is the signal-to-noise-ratio at its output. Assuming the SNR quantities to be voltage ratios, the NF in Decibel (dB) is given by [53, 31]

$$\mathrm{NF} = 20 \log\left(F\right) = 20 \log\left(\frac{\mathrm{SNR_{in}}}{\mathrm{SNR_{out}}}\right) = \mathrm{SNR_{in,dB}} - \mathrm{SNR_{out,dB}}, \tag{2.36}$$

where $SNR_{\mathrm{in,dB}}$ and $SNR_{\mathrm{out,dB}}$ are given in dB.

Assuming a voltage amplification, $\mathrm{SNR}_{\mathrm{out}}$ can be calculated based on Eq. (2.36) by [53]

$$\mathrm{SNR}_{\mathrm{out}} = \frac{\mathrm{SNR}_{\mathrm{in}}}{10^{\frac{\mathrm{NF}}{20}}}. \tag{2.37}$$

Based on the input referred noise voltage $V_{\mathrm{n,LNA}}$ of the LNA and the additionally added noise voltage by the signal source $V_{\mathrm{n,input}}$ (e.g. thermal noise of the connected RF coil, cf. chapter 2.1.5 – *The loss mechanism*), the NF can be estimated by [53]

$$\mathrm{NF} = 20 \log \left(\sqrt{1 + \left(\frac{V_{\mathrm{n,input}}}{V_{\mathrm{n,LNA}}} \right)^2} \right). \tag{2.38}$$

Since the LNA has to be placed within the B_0-field, all used components of the LNA-module are non-magnetic, in order to avoid any metal artifacts or B_0-field distortions. Nowadays, a off-the-shelf MRI LNA provides a NF between 0.4 dB and 0.6 dB and a gain of approximately 30 dB.

Considering the entire receive chain, more amplifiers are in series with the first LNA, until the NMR signal is preprocessed and can be digitized. The overall NF of these cascaded amplifiers can be found with Friis' formula [53]

$$\mathrm{NF} = 20 \log \left(F_1 + \frac{F_2 - 1}{G_1} + \frac{F_3 - 1}{G_1 G_1} + \cdots + \frac{F_n - 1}{G_1 G_2 \cdots G_{n-1}} \right), \tag{2.39}$$

where F_n is the NF for the n-th device and G_n is the linear (not in dB) power gain of the n-th device. A schematic illustration of an MR receive chain consisting of three amplifiers is illustrated in Fig 8.

Considering Eq. (2.39), the noise factor and thus the NF of the first amplifier (indicated as LNA, 1$^{\mathrm{st}}$-stage in Fig. 8) in a receive chain usually has the most significant effect on the total NF as the NF of the following stages are reduced by the amplifier gains. Consequently, the first amplifier should have a NF which is as small as possible, whereas the NF requirements of subsequent amplifiers are usually more relaxed.

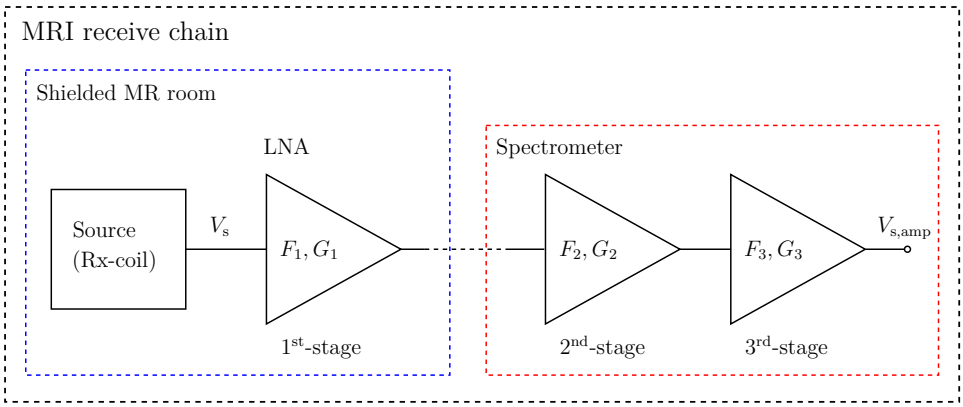

Figure 8: Schematic illustration of a MRI receive chain with three amplification stages. The Rx coil and the LNA are located inside the shielded MR room and connected to the spectrometer by a TRL. The NMR signal V_s is amplified three times in this example (resulting in $V_{s,amp}$) and can than be used by further signal processing tasks.

Narrowband 50 Ω-LNA

A schematic illustration of a narrowband MRI preamplifier architecture according to [10], as it is used in the work presented in the following chapters, is depicted in Fig. 9. The essential part of almost every LNA (module) are active devices (e.g. Gallium Arsenide Field-Effect Transistor (GaAsFET)). The input impedance Z_{in} is matched by an input noise matching network to 50 Ω (popular in single coil configurations) or to a low input impedance of a few Ohm to allow preamplifier decoupling used in coil arrays. The output impedance Z_{out} is matched to 50 Ω by the output gain matching network to avoid losses on the TRL. Even though, the active devices used on the LNA are broadband by itself, the passive input noise matching network and the passive output gain matching network are frequency selective. This in turn results in narrowband, frequency selective properties of the LNA module.

The LNA modules used in this work have a NF of typically 0.6 dB, a gain of typically 28.5 dB and a bandwidth of approximately 3 MHz around the center frequencies, according to the data-sheets.

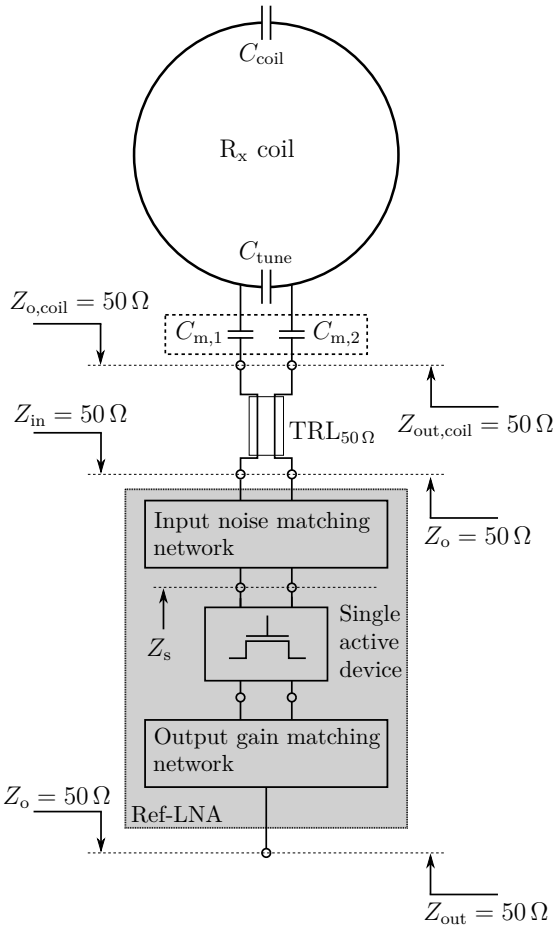

Figure 9: Schematic illustration of a simple MRI Rx only receive chain setup including a LNA and a surface coil. The architecture of a conventional MRI preamplifier according to [10] is depicted.

Broadband LNA

Compared to a narrowband LNA, a broadband high impedance LNA offers a much broader bandwidth. This in turn offers many interesting areas of applications regarding the signal acquisition in MR systems, such as multi-nuclei imaging, since a broadband amplifier enables an amplification of signals with different frequencies which are within the operation range of the amplifier.

Due to the architecture of a high impedance broadband LNA, the frequency selective passive matching networks are not required. This topic is investigated in chapter 2.2 – *Special aspects of X-nuclei imaging* in a more detailed way.

Transmission lines and matching

The EMF (signal) induced into the coil is transmitted to the LNA through a TRL, as depicted in Fig. 9. A TRL is composed of two conductors arranged either in asymmetric (e.g. coaxial, microstrip, stripline, coplanar waveguide) or in balanced (e.g. linear or twisted wires) configuration.

Efficient power transfer is given when the TRL functions in the so-called differential mode. In this mode, the currents in the two conductors flow in opposite directions, which results in an extinction of the electromagnetic field outside the line.
In the so-called common mode, the currents in both conductors flow in the same direction, which results in an undesired electromagnetic field outside the TRL. This radiated electromagnetic energy outside the cable results in additional losses or RF interferences and can, in the worst case, even lead to patient burning in clinical MR scanners. For this reasons, this mode should obviously be avoided [30]. In the following, only the differential mode will be addressed.

A TRL has a characteristic impedance of $Z_{\mathrm{TRL}} = 50\,\Omega$, which is widespread in communication technology applications, since this represents a trade-off between the lowest losses (attenuation), the highest electrical strength and the best power transfer capability [7]. In order to avoid additional losses and to provide a sufficient power transfer, it is crucial to match the impedance $Z_{\mathrm{out,coil}}$ (cf. Fig. 9) of the coil and the TRL, since an unmatched coil connected to a TRL will result in reflections of the EMF (signal) that is supposed to be receipted by the coil. This in turn will result in a signal loss. The reflection coefficient Γ is defined as [46]

$$\Gamma = \frac{Z_{\mathrm{out,coil}} - Z_{\mathrm{TRL}}}{Z_{\mathrm{out,coil}} + Z_{\mathrm{TRL}}}. \tag{2.40}$$

On condition that $\Gamma = 0$, all power is transmitted since all reflections are eliminated. Regarding Eq. (2.40), this condition is achieved if $Z_{\mathrm{out,coil}} = Z_{\mathrm{TRL}}$.

Depending on the geometry of the coil, the number of capacitors and their values, the initial impedance $Z_{\mathrm{out,coil}}$ is most likely different from the impedance of the TRL. Thus it appears that a matching network has to be implemented, which adapts the different impedances. In literature, many different architectures of matching networks are known [46, 30]. As an example, a simple technique of matching a coil is depicted in Fig. 9. It is realized by adding two capacitors ($C_{\mathrm{m,1}}$ and $C_{\mathrm{m,2}}$) in series with the shield and the signal-line of the TRL, located close to the tuning capacitor C_{tune}.

2.1.5 The loss mechanism

The effective resistance (noise source) of a coil loaded by a sample (e.g. a phantom or a patient) is composed of contributions originating from the coil (resistive losses - R_{coil}) and from the sample (sample losses - R_{sample}). The effective coil resistance is caused by the random thermal motion of electrons in the RF coil and from radiation being emitted and absorbed by the RF coil. The sample resistance arises from inductive and dielectric coupling between the RF coil and the sample. The total loss of a loaded coil is thus given by

$$R_{\mathrm{loss}} = R_{\mathrm{coil}} + R_{\mathrm{sample}}. \tag{2.41}$$

Resistive loss

The resistive losses R_{coil} are induced by the losses of the coil conductor itself, the coil components (connectors, capacitors, PIN-diodes, etc.) and their soldering joints. Since the skin effect occurs at high frequencies, the current flows mainly between the outer surface of the conductor and a level called skin depth. The skin depth decreases at

higher frequencies resulting in a reduction of the effective cross-section of the conductor. This in turn results in an increase of the effective resistance proportional to the frequency ($R_{\mathrm{coil}} \propto \sqrt{\omega}$).

Copper is predominantly used for coil conductors due to its very high conductivity of ($58 \times 10^6\,\mathrm{S/m}$). The conductivity can further be improved by using silver. Its conductivity is again 5 % higher than the conductivity of copper ($61 \times 10^6\,\mathrm{S/m}$). However, since the resistive losses are typically not a major concern in coils for human imaging at higher field strengths, this conductivity improvement doesn't improve the overall losses mentionably[3] (cf. chapter 2.1.4 – *Quality factor*).

Sample loss

An electric field in the near field of the coil results in a displacement current in a dielectric sample (e.g. human tissue) placed in the RF field of the coil. This causes an equivalent resistance R_{sample} modeling the dielectric sample losses. R_{sample} can be computed by

$$P_{\mathrm{sample}} = R_{\mathrm{sample}} \cdot I_{\mathrm{coil}}^2, \tag{2.42}$$

where P_{sample} is the power dissipated in the sample produced by the coil current I_{coil}. The loss in the sample is produced from conductive and dielectric losses due to the finite sample conductance. P_{sample} can also be calculated according to [36, 38]

$$P_{\mathrm{sample}} = \int\limits_{\mathrm{V_{sample}}} |\vec{E}_{\mathrm{rms}}|^2 \cdot \sigma_{\mathrm{e}}\,\mathrm{d}V, \tag{2.43}$$

where $\vec{E}_{\mathrm{rms}}$ is the root mean square of the electric field inside the sample. Here, σ_{e} is the total sample conductance $\sigma_{\mathrm{e}} = \sigma_{\mathrm{s}} + \omega_0\epsilon''$, where σ_{s} is the electrical conductivity of the sample and $\omega_0\epsilon''$ is the imaginary part of its complex permittivity.

[3] For this reason, gryo-cooled coils doesn't cause any mentionable advantages in sample dominated MRI applications as human imaging.

By replacing the E-field in Eq. (2.43) with an unitary E-field similar to the unitary magnetic field B_u (cf. chapter 2.1.3 – *RF transmission and reception*) according to:

$$\vec{E}_\mathrm{rms} = \vec{E}_\mathrm{u} \cdot I_\mathrm{coil}(t), \tag{2.44}$$

R_sample can be computed from

$$R_\mathrm{sample} = \int_{\mathrm{V_{sample}}} \vec{E}_\mathrm{u}^2 \cdot \sigma_\mathrm{e}\, \mathrm{d}V. \tag{2.45}$$

Eq. (2.45) shows that the equivalent resistance R_sample depends on the sample conductivity σ_e, which is of course depending on the sample (tissue) properties, and on the E-field distribution of the coil. Even though generating an E-field is unavoidable, the amount of R_sample can be manipulated by the coil design. This can be illustrated by e.g. a simple loop coil with a single capacitor and an induced voltage plotted as a function of the distance x around the coil as shown in Fig. 10a.

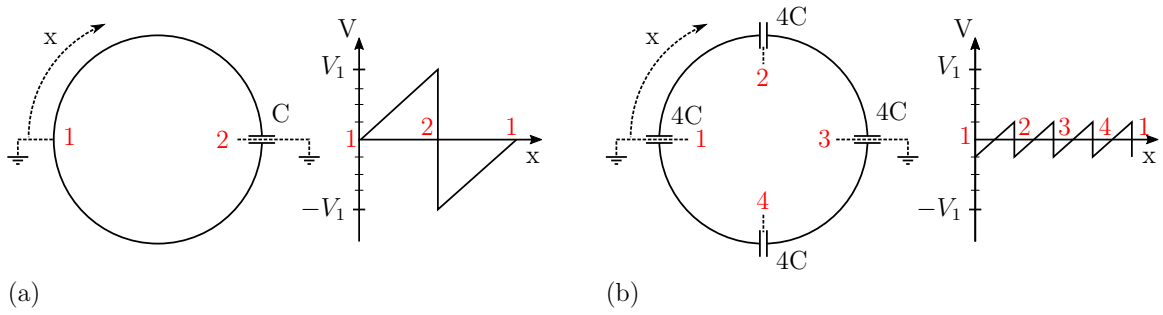

Figure 10: Simple loop coil with a single capacitor (a) / four capacitors (b) and the voltage distribution as a function of the distance x around the coil.

The voltage distribution (potential difference) along the coil and at the capacitor generates an E-field which depends on the amount of the potential difference.

Assuming a coil with the same geometric design as the coil in Fig. 10a, the amount of the potential difference (and thus the amount of the resulting E-field) can be reduced by splitting the coil with further capacitors. Considering a series combination of four coil capacitors which are uniformly distributed as depicted in Fig. 10b, the maximum potential difference will fall to $1/4^{\text{th}}$ of the amount of Fig. 10a.

Even though, distributed capacitors will minimize losses, every additional capacitor raises the resistance of the coil (R_{coil}) due to its equivalent series resistance which is present in the capacitor itself and the soldered connections. Therefore, a compromise has to be found between the number of capacitors segmenting the coil and the rising resistance of the coil for maximizing the effect of that method. As a rule of thumb, the length of each segment should be in the range of $\lambda_0/10$ to $\lambda_0/20$, where λ_0 is the wavelength of the Larmor frequency.

Assuming a constant sample conductivity, the equivalent resistance R_{sample} is proportional with the square of the frequency ($R_{\text{sample}} \propto \omega^2$).

Noise

Corresponding to chapter 2.1.5 – *The loss mechanism*, the noise sources can ideally be separated into the thermal noise of the coil ($V_{\text{n,coil}}$) and the thermal noise associated with losses in the sample ($V_{\text{n,sample}}$). However, in any realistic system, the noise floor is also affected by the NF of the electronics in the receive chain, which will be accounted at the end of this chapter.

Assuming these two noise sources to be uncorrelated, the total RMS noise floor $V_{\text{n,tot}}$ can be calculated by adding their corresponding variances according to [6]

$$V_{\text{n,tot}} = \sqrt{V_{\text{n,coil}}^2 + V_{\text{n,sample}}^2}. \tag{2.46}$$

Based on the fluctuation dissipation theorem [50], the RMS noise voltage of the coil can be calculated as

$$V_{\mathrm{n,coil}} = \sqrt{4\, k_{\mathrm{B}}\, T\, R_{\mathrm{coil}}\, \Delta f}, \tag{2.47}$$

where k_{B} is the Boltzmann constant ($k_{\mathrm{B}} = 1.38 \times 10^{-23}\,\mathrm{J/K}$), T is the temperature in Kelvin, R_{coil} is the real part of the coil impedance at the frequency of interest and Δf is the corresponding bandwidth (pixel-bandwidth).

According to the RMS noise voltage of the coil, the RMS noise voltage of the sample is given by

$$V_{\mathrm{n,sample}} = \sqrt{4\, k_{\mathrm{B}}\, T\, R_{\mathrm{sample}}\, \Delta f}, \tag{2.48}$$

where R_{sample} is the equivalent sample resistance calculated in Eq. (2.45).

2.1.6 Signal-to-Noise ratio

One of the main objective tasks of an RF coil and accordingly of an MR RF receive chain is to achieve as much SNR as possible. In this chapter, the SNR calculation and the SNR measurement are explained in detail.

SNR calculation

The SNR of each voxel of a phantom can be calculated using [2]

$$\mathrm{SNR}_{\mathrm{voxel}} = \frac{V_{\mathrm{signal,vox}}}{V_{\mathrm{n,tot}}} \sqrt{N_{\mathrm{PE}}} \sqrt{N_{\mathrm{avg}}}, \tag{2.49}$$

where N_{PE} is the number of phase encoding steps and N_{avg} is the number of averages for each phase encoding step, respectively.

Intrinsic SNR

The intrinsic Signal-to-Noise-Ratio (iSNR) of a coil/sample setup describes the maximum SNR performance of this setup, achievable at the ports of the coil. Assuming N_{PE} and N_{avg} to be one, Eq. (2.49) results in $\mathrm{iSNR} = V_{\mathrm{signal}}/V_{\mathrm{n,tot}}$.

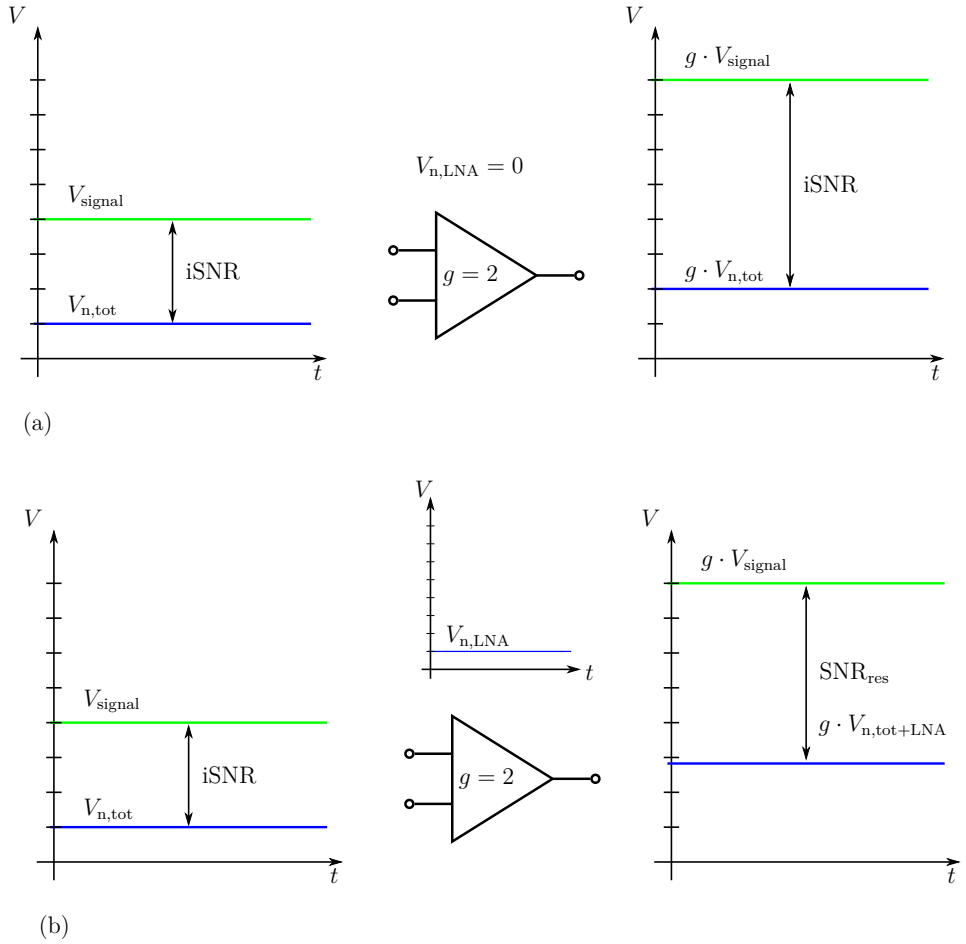

Figure 11: The iSNR of a coil/sample setup boosted by a ideal LNA with no inherent noise results in the same SNR at the output and at the input of the LNA (a), whereas the inherent noise of a real LNA causes a unavoidable SNR reduction at the LNA's output compared to the SNR at its input (b).

The noise voltage $V_{\mathrm{n,tot}}$ (noise-floor) of a measurement setup is given by the coil/sample combination (cf. chapter 2.1.5 – *Noise*) and is illustrated in Fig. 11a (blue) as a function over time. Assuming an optimized coil/sample setup, the amount of this noise voltage can no longer be reduced. The EMF signal voltage V_{signal} of the sample under

investigation is illustrated in Fig. 11a (green), respectively, which results in the iSNR. Assuming an ideal LNA (with no inherent noise), the resulting SNR at the output of the LNA is the same as the SNR at the input, since no additional noise is added, as illustrated in Fig. 11a.

Assuming the same conditions as in Fig. 11a combined with a real (same gain, but inherent noise $V_{\mathrm{n,LNA}}$) LNA, the EMF signal voltage V_{signal} results in the same amplitude at the output of the LNA, as shown in Fig. 11b. However, in contrast to Fig. 11a, the input referred noise voltage of the LNA is unequal zero.

This results in a noise floor $g \cdot V_{\mathrm{n,tot+LNA}} = g \cdot \sqrt{V_{\mathrm{n,tot}}^2 + V_{\mathrm{n,LNA}}^2}$, with $g \cdot V_{\mathrm{n,tot+LNA}} > g \cdot V_{\mathrm{n,tot}}$, which results in a SNR reduction at the output of the LNA ($\mathrm{SNR_{res}} < \mathrm{iSNR}$).

This SNR reduction caused by the LNA cannot be prevented, but its influence can be reduced if $V_{\mathrm{n,tot}} \gg V_{\mathrm{n,LNA}}$, which can be achieved by optimizing the LNA design to reduce the amount of $V_{\mathrm{n,LNA}}$ or by using a resonant coil structure. In this case, both, the noise voltage $V_{\mathrm{n,tot}}$ as well as the MR signal V_{signal}, are boosted by $Q_{\mathrm{l}}/2$ according to Eq. (2.34), which results in $V_{\mathrm{n,tot}} \gg V_{\mathrm{n,LNA}}$ again.

SNR measurement

The SNR determination of MR images is described by the standardized methods in the National Electrical Manufacturers Association (NEMA) Standard Publication MS 1-2008 [37]. All comparative SNR measurements in the following chapters presented at this work are calculated based on magnitude images, thus, method number 4 of the standard is used.

According to the NEMA standard, the standard deviation of the noise in the complex domain $\hat{\sigma}_{\mathrm{N}}$ can be found in two different ways:

- Estimation based on the standard deviation of the measured noise according by

$$\hat{\sigma}_{\mathrm{N},\sigma} = \frac{\hat{\sigma}\left(I_{\mathrm{N},1}, \ldots, I_{\mathrm{N},i}\right)}{0.66}, \tag{2.50}$$

where $I_{\mathrm{N},1}, \ldots, I_{\mathrm{N},i}$ describes the intensity levels of each noise voxel i.

- Estimation based on the measured mean noise level $\hat{\mu}$ given by

$$\hat{\sigma}_{\mathrm{N},\mu} = \frac{\hat{\mu}\left(I_{\mathrm{N},1}, \ldots, I_{\mathrm{N},i}\right)}{1.25}. \tag{2.51}$$

The additional index σ indicates the estimation based on the standard deviation, whereas the index μ indicates the estimation based on the mean noise level.

The signal intensity $\hat{S}$ of the image is determined from the mean voxel value $\hat{S} = \hat{\mu}\left(I_{\mathrm{S},1}, \ldots, I_{\mathrm{S},i}\right)$ inside a signal ROI, with a signal intensity $I_{\mathrm{S},i} \geq 6 \cdot \sigma_{\mathrm{N}}$.

The SNR of the magnitude image can be calculated using

$$\mathrm{SNR} = \frac{\hat{S}}{\hat{\sigma}_{\mathrm{N},\sigma,\mu}}. \tag{2.52}$$

In general, assuming high frequencies, the net magnetization M_0 is proportional to the static magnetic field B_0. Furthermore, ω_0 is also proportional to B_0, which results in [12]

$$\hat{S} \propto \omega_0 M_0 \propto B_0^2. \tag{2.53}$$

Since coil losses are negligible at high frequencies (cf. chapter 2.1.4 – *Quality factor*), R_{sample} is proportional to B_0. Using Eq. (2.48), this results in

$$V_{\mathrm{n,sample}} \propto B_0. \tag{2.54}$$

Dividing (2.53) by (2.54) results in

$$\mathrm{SNR} \propto B_0. \tag{2.55}$$

Because of the RF skin effect, the equivalent noise resistance from the coil is proportional to $\sqrt{B_0}$, therefore, assuming high frequencies, sample losses must dominate.

At low frequencies, when R_{coil} becomes significant compared to R_{sample}, the SNR is proportional to $B_0^{7/4}$ [12].

2.1.7 Simulation

A major problem when designing custom-made RF coils is a priori missing information on its sensitivity pattern, its penetration depth and of course its final SNR performance.

In a first step, the E-field and H-field of a coil, that naturally depends on the coil's geometry, can be simulated by CEMs – including the full geometric and material properties of both the coil and the sample under investigation – using CST MICROWAVE STUDIO (CST-MWS). Based on these information, the coil properties including the achievable SNR performance (cf. chapter 2.1.6 – *Signal-to-Noise ratio*) can be estimated.

In a second step, a resulting MR image can be simulated under investigation of the target MR sequence using Jemris [43].

2.1.8 Decoupling of Coil Arrays

As discussed in chapter 2.1.4 – *Detuning*, coils tuned to the same resonance frequency f_0 interact between each other. In contrast to the example mentioned in chapter 2.1.4 – *Detuning* (typically used for a combination of a transmit coil and a receive coil at which only one coil is tuned while the second coil is detuned) there are applications where multiple coils have to be tuned at the same time.

A typical application of multi coil elements is a phased array coil, offering the SNR and resolution of a small surface coil but covering a large FOV [41]. Assuming two identical resonant loops – as the simplest implementation of a phased array coil – tuned to the same resonance frequency f_0, which are placed near each other. As indicated in Fig. 12, the mutual inductance between the coils causes the resonances to split [41]. This mutual

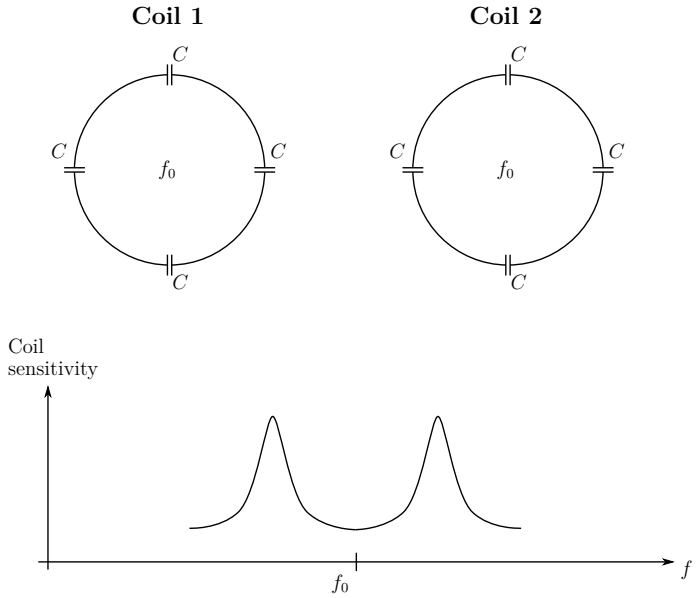

Figure 12: Schematic illustration of the sensitivity split of two equivalent surface coils tuned to the same frequency f_0 located next to each other. The coils sensitivity is significantly reduced at the original resonance frequency f_0 due to mutual coupling. Modified from [41], copyright © 1990 Wiley-Liss, Inc., A Wiley Company.

coupling and hence the splitting results in a loss of sensitivity at the original resonance frequency f_0, and signal and noise transfer between the coil elements. This coupling is reduced in classic coil array designs by overlapping nearest neighboring coil array elements, and using low impedance LNAs to perform preamp-decoupling [41].

Geometrical decoupling

The easiest way to force the mutual inductance to zero is to overlap nearest neighboring coil array elements, as depicted in Fig. 13. By overlapping two coil elements, the current in the overlapping area is flowing in the opposite direction. Assuming a pair of identical resonant loops with the same current I_{coil} flowing in both coils, a distance of $0.75 \cdot r$ of the coils center results in an overlap which sets their mutual inductance to zero and thus eliminates the problem of splitting resonances for nearest neighbors. For coil elements with a more complex geometrical shape, the optimal overlap can be simulated e.g. by

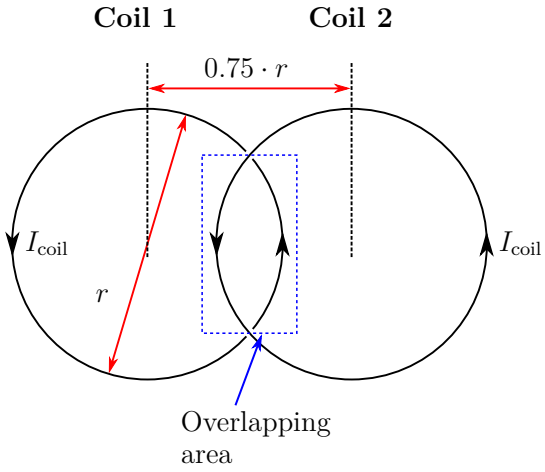

Figure 13: Decoupling of adjacent coil elements by overlapping to eliminate their mutual inductance. Modified from [41], copyright © 1990 Wiley-Liss, Inc., A Wiley Company.

CEM simulations (cf. chapter 2.1.7 – *Simulation*) and thus being taken into account during the development and design process.

Preamplifier decoupling

Even in case of geometrical decoupling, a small but significant interaction between neighboring and more distant coil elements still remains, which naturally can not be eliminated by geometrical overlapping. These interactions can be reduced to negligible levels by preamplifier decoupling. Therefore, in current coil array designs all coil elements are connected to low impedance LNAs with a typical impedance of a few Ohms. This low impedance is transformed into a high impedance which is in parallel with the RF coil (LCR-circuit), which causes a reduction of the current flowing in the coil during reception. The theory of operation is explained based on two equal surface coils which are located with a distance d next to each other, as illustrated in Fig. 14. Coil B is connected to a low impedance LNA with an input impedance R_{p}, connected to the coil in series with an inductor. The basic principle of preamplifier decoupling is a

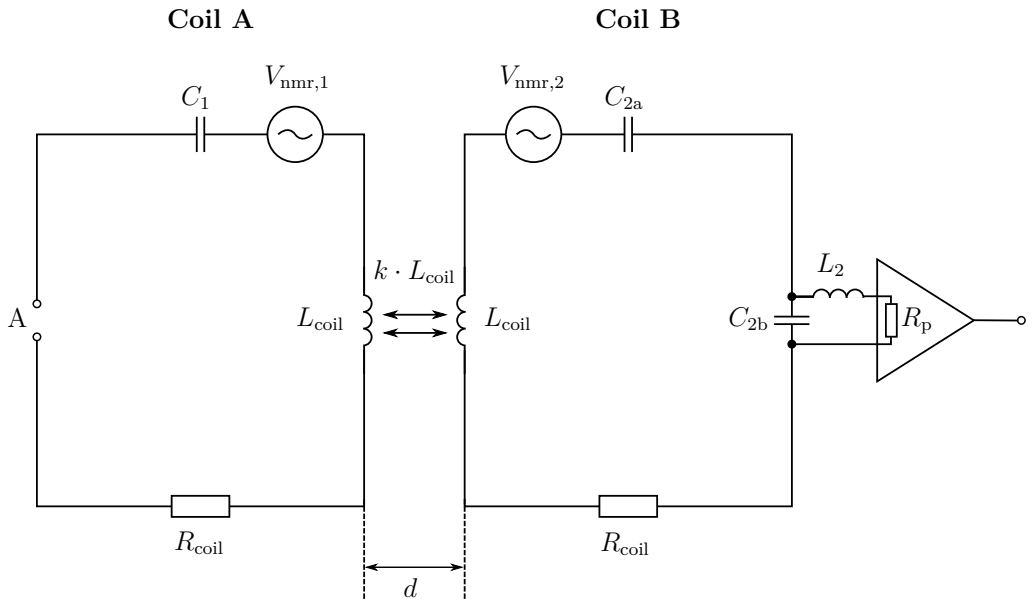

Figure 14: Schematic illustration of two interacting surface coils, one of which is connected to a LNA. The induced NMR voltages are illustrated by $V_{\mathrm{nmr,1}}$ and $V_{\mathrm{nmr,2}}$, respectively. Modified from [41], copyright © 1990 Wiley-Liss, Inc., A Wiley Company.

matching network, that is designed as a resonance circuit (LCR-circuit). This matching network (including $C_{2\mathrm{b}}$, L_{L2} and R_{p}), which is tuned to the Larmor frequency of the coil, results in a high impedance in series of the coil. The quality factor Q_{decouple} of the matching network is mostly determined by the input impedance R_{p} of the LNA. A low input impedance results in a huge quality factor Q_{decouple}, which in turn results in a huge impedance in series of the coil. As described in chapter 2.1.4 – *MR coils – An RF resonator*, resonance of the matching network is achieved by choosing $|X_{\mathrm{C_{2b}}}| = |X_{\mathrm{L_2}}| \equiv X_2$.

With this coil B being present and connected to a LNA, the impedance as viewed from the terminals at port A of coil A is then given by [41]

$$Z_{\mathrm{A}} = R_{\mathrm{coil}} + \frac{\omega^2 L_{\mathrm{coil}}^2 k^2}{R_{\mathrm{coil}} + (X_2^2/R_{\mathrm{p}})}, \tag{2.56}$$

where k is the mutual inductance coupling constant of the coils and ω is the resonance frequency. The second term of Eq. (2.56) describes the noise power coupling transferred between the coils. This term approaches zero if either k is made zero (by increasing the distance between the coil) or R_p is made zero. This results in a noise resistance R_coil, which is equal to the noise resistance of a single isolated coil [41].

The coupling of the NMR signal between coils is given by [41]

$$V_\mathrm{A} = V_\mathrm{nmr,1} + V_\mathrm{nmr,2} \cdot \frac{j\,\omega\,L_\mathrm{coil}\,k}{R_\mathrm{coil} + (X_2^2/R_\mathrm{p})}, \tag{2.57}$$

equal to noise power coupling. Again, by setting the mutual conductance or the LNA input impedance to zero, the coupling of the NMR signal is suppressed, as well [41].

2.2 Special aspects of X-nuclei imaging

In this chapter, the special aspects of X-nuclei imaging are specified and announced.

2.2.1 Requirements towards broadband receive coils

As an alternative approach towards multi-nuclei coils, the feasibility of a Non Resonant (NR) coil in combination with a broadband, high impedance LNA is investigated. This represents a tremendous simplification of the multi nuclei RF coil and the receive path, respectively, since the design of multi-nuclei coils which are tuned to different Larmor frequencies including the receive path with its narrowband tuned LNAs for each resonance frequency can be cumbersome.

As per description in chapter 2.1.6 – *Intrinsic SNR*, the iSNR is independent on the coils tuning. Tuning is used for ensuring a negligible noise contribution of the subsequent LNA. Instead of boosting the noise floor of the coil/sample combination significantly above the inherent noise of the LNA by using a resonant coil (which is currently the state-of-the-art solution), in this approach, the inherent noise of the LNA should be reduced to achieve $V_{\mathrm{n,tot}} \gg V_{\mathrm{n,LNA}}$.

By using a broadband LNA with a high impedance input, the current flowing inside the coil can be reduced by attaching the LNA immediately in series with the NR coil. This resulting short electrical connection in principle removes the need for an impedance match to a long transmission line. To ensure compatibility with the existing MR infrastructure, the output impedance of the LNA is set to $50\,\Omega$.

For obtaining the requirements of the input referred voltage noise spectral density of the broadband, high impedance LNA, a coil/sample setup as illustrated in Fig. 15 is simulated, based on the theory and tools introduced in chapter 2.1 – *General aspects of Magnetic Resonance Imaging*.

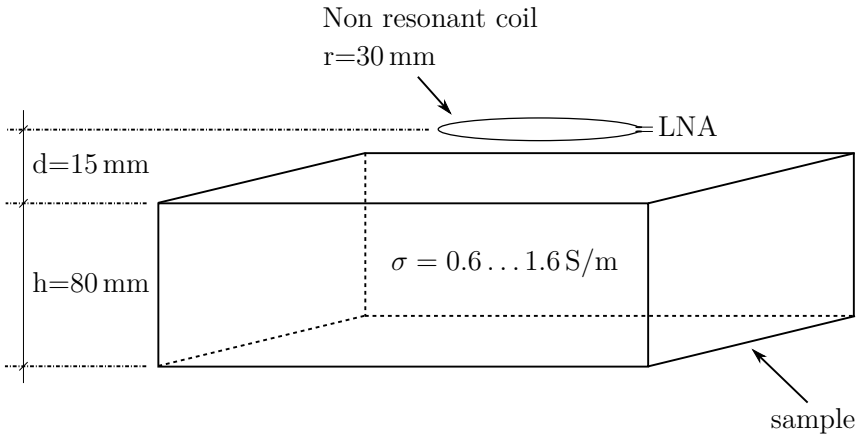

Figure 15: Schematically illustration of the NR coil/sample setup. The coil has a radius of 30 mm and is located with a distance of 15 mm above a phantom, whose conductance is varied from $\sigma = 0.6\,\mathrm{S/m}$ to $\sigma = 1.6\,\mathrm{S/m}$ by simulations.

A NR coil with a radius of $r = 30\,\mathrm{mm}$ is located with a distance of $d = 15\,\mathrm{mm}$ above a sample, which represents a typical use of a surface coil in a clinical MRI system (surface coil with its coating, located on a patient). The conductivity σ of the sample is varied in $0.2\,\mathrm{S/m}$ steps within a range of $\sigma = 0.6\,\mathrm{S/m}$ to $\sigma = 1.6\,\mathrm{S/m}$. Since the broadband, high impedance LNA is attached to the coil without any matching network, the impedance connected to its input results as the sum of the impedance of the coil R_{coil} and of the equivalent impedance of the sample R_{sample} (cf. Eq. (2.41)). Based on Eq. (2.45), the equivalent impedance of the sample depends on the sample's conductivity σ as well as the E-field generated by the coil and is simulated as described in chapter 2.1.7 – *Simulation*.

The resulting NFs of the broadband LNA based on different combinations of sample conductivities σ and different input referred voltage noise spectral densities $U_{\mathrm{n,LNA}}$ of the broadband, high impedance LNA (cf. Eq.(2.38)) are given in Table 1.

In contrast to a homogeneous phantom with a defined electronic conductance, in clinical applications the conductivity of human tissue is not distributed equally. In Table 2, a selection of the electronic conductivity of different human tissues is given which is in the

Table 1: Simulated NF of the broadband, high impedance LNA depending on the sample conductance σ and the LNA's input referred voltage noise spectral density $U_{\mathrm{n,LNA}}$, relating to the setup depicted in Fig. 15.

	$U_{\mathrm{n,LNA}}$ $\left[\mathrm{pV}/\sqrt{\mathrm{Hz}}\right]$				
σ [S/m]	120	100	80	60	50
0.6	2.5 dB	1.8 dB	1.3 dB	0.8 dB	0.5 dB
0.8	2.1 dB	1.6 dB	1.1 dB	0.6 dB	0.4 dB
1.0	1.8 dB	1.4 dB	0.9 dB	0.5 dB	0.4 dB
1.2	1.7 dB	1.2 dB	0.8 dB	0.5 dB	0.3 dB
1.4	1.5 dB	1.1 dB	0.7 dB	0.4 dB	0.3 dB
1.6	1.4 dB	1.0 dB	0.7 dB	0.4 dB	0.3 dB

range of $\sigma_{\mathrm{Liver}} = 0.49\,\mathrm{S/m}$ and $\sigma_{\mathrm{Fat}} = 1.38\,\mathrm{S/m}$. Since the broadband, high impedance LNA is connected to the coil without any matching networks, the inductance of the sample and thus the sample conductivity immediately affects the achievable NF of the LNA.

Based on the simulations and the tissue's electronic conductivities, Table 1 can be used to determine the necessary input referred voltage noise spectral density $U_{\mathrm{n,LNA}}$ of the LNA to achieve a desired NF. Assuming an average electronic conductivity of e.g. $\sigma_{\mathrm{avg}} = 1.0\,\mathrm{S/m}$, $U_{\mathrm{n,LNA}}$ must be in the region of $50\,\mathrm{pV}/\sqrt{\mathrm{Hz}}$ to $60\,\mathrm{pV}/\sqrt{\mathrm{Hz}}$ to achieve a NF between 0.4 dB and 0.5 dB in order to provide the similar performance as a state-of-the-art tuned surface coil in combination with a narrowband LNA.

Since the electronic conductivity is defined by the sample under investigation, the only parameter to relax the burden of the noise performance of the LNA while using a NR coil is the coil's diameter. Assuming a phantom, which size (width and height) is much larger than the diameter of the coil, an increasing coil diameter will lead to an increase of the sample inductance and the coil inductance. This results in a decrease of the

Table 2: Electronic conductivity σ of human tissues, given in $[S/m]$ at a frequency of 64.0 MHz, corresponding to the proton Larmor frequency at 1.5 T MRI systems.

Tissue	Elec. Cond. σ [S/m]
Blood	1.23 [20]
Brain	0.79 [20]
Fat	1.38 [20]
Heart Muscle	0.73 [20]
Kidney	0.81 [44]
Liver	0.49 [20, 44]
Muscle	0.71 [20, 44]

NF (according to Eq. 2.46 and Eq. (2.38)) without any changes in the input referred voltage noise spectral density of the broadband, high impedance LNA.

Beside the discontinuation of a degree of freedom during the coil development process, the maximum coil diameter is defined by the self resonance of the coil, occurring due to the coil's inductance L_{coil} and the input capacitance $C_{\text{in,LNA}}$ of the LNA, which is typically within the range of 1 pF to 3 pF.

2.2.2 Electronically tunable/switchable RF coils

As a possible alternative solution, an electronically tunable/switchable RF coil represents a potentially compromise to realize multi-frequency MR coils. For this purpose, the coil is designed as a resonant LCR circuit, whose resonance frequency can be adjusted within a defined range. In combination with a broadband, high impedance LNA as described in chapter 2.2.1 – *Requirements towards broadband receive coils*, this approach provides the flexibility of a NR coil regarding the usable bandwidth but relaxes greatly the burden of the LNA's noise performance.

Since, in this approach, the broadband, high impedance LNA is also connected to the coil without any matching network (as mentioned in chapter 2.2.1 – *Requirements towards broadband receive coils*), the noise figure of this LNA is solely depending on the relation of the coil/sample noise and the LNA's input referred voltage noise spectral density (cf. Eq. (2.38)). As described in chapter 2.1.4 – *Quality factor*, the signal and noise are boosted by a factor of $Q_\mathrm{l}/2$ by the LCR circuit, significantly. This in turn results in a boosted coil/sample noise $V_{\mathrm{n,tot,boosted}}$, which is significant larger than the equivalent noise voltage of the LNA.

For the realization of switchable/adjustable MR Rx coils, approaches based on PIN diodes to switch between different capacitors [35, 23], Variable Capacitor Diodes (Varactors) or even motor driven capacitors [27] are introduced in literature. In this thesis, the feasibility of tuning a coil by using electronic controllable capacitor arrays is investigated.

Nevertheless, using a resonant circuit relaxes greatly the burden of the LNA's noise performance, an improvement (reduction) of the input referred voltage noise spectral density will result in a significant increase of the SNR at the output of the LNA, if the sample under investigation has a low electronic conductivity or a coil with a poor filling factor is used.

3 Summary of published articles

In this chapter, the methods and the hardware used in this thesis are summarized.

3.1 An EM simulation based design flow

In the first part of this work, an EM simulation based design flow for custom-built MR coils is introduced. For specific applications, the development of dedicated MR coils is required, since a highly specialized geometry is necessary to achieve an optimal SNR inside the specific ROI [36]. This in turn is a cumbersome task which typically requires several hardware manufacturing iterations/adaptations.

The introduced design flow provides an a priori prediction of the coils' sensitivity pattern, their SNR performance and their B_1-field pattern which is simulation by CEMs. Furthermore, the entire MR imaging process including all geometric and material properties of the coil and the sample, the thermal noise as well as the MR sequences are simulated.

This EM simulation based design flow is illustrated in Fig. 16 in comparison to a conventional design flow. Due to the a priori information of the coils' performance, this design flow helps to greatly reduce the required hardware manufacturing iterations, which in turn speeds up the developing process and reduces the total development costs.

The proposed simulation-based design flow is evaluated using a manufactured prototype coil, whose SNR performance is optimized by the CEM-based approach. The

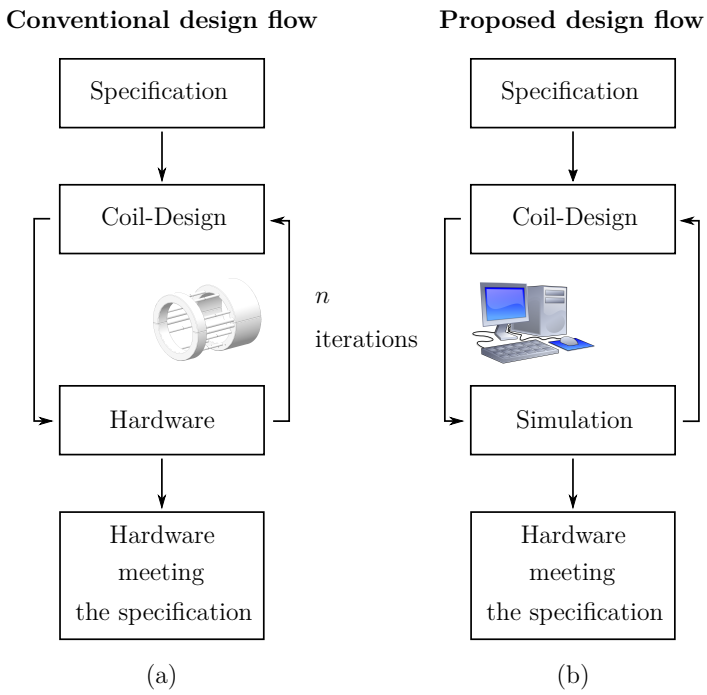

Figure 16: Comparison of a conventional hardware-oriented coil design flow (a) and the introduced simulation-based design flow (b). – [25], copyright © 2018 IEEE.

performance of the approach is validated by comparing the measured performance of the prototype coil against its simulated performance.

3.2 A signal acquisition setup in parallel on unmodified clinical MRI systems

The second part of this work is a vendor independent receive-only system (receive chain and image acquisition system), which operates in parallel to a clinical MRI system (host system).

The setup is based on standard industrial measurement equipment for handling Transistor-Transistor Logic (TTL) signals and data acquisition. The synchronization of the introduced receive-only system (guest system) is achieved by a local oscillator clock

reference and a RF pulse timing reference provided by the host system, respectively. Thus, there are no mechanical or electrical modifications required on the host system.

Since the imaging sequences are executed on the host system without any modifications, the pre-scan procedures (e.g. pulse power optimization and shimming), as well as the spin excitation and the SAR control during the scan are performed by the unmodified host system.

The receive-only system presented in chapter 4.2 - *A Signal Acquisition Setup Operating in Parallel on Unmodified Clinical MRI Scanners* offers both, an image acquisition setup for ultrashort echo time imaging as well as a vendor independent coil testing, optimization and development framework. Thus, this system was used in this thesis for image acquisition of any custom-built coils.

3.3 High impedance CMOS LNA with an input referred voltage noise spectral density of $200\,\mathrm{pV}/\sqrt{\mathrm{Hz}}$

The limiting factor regarding the SNR performance of the receive chain introduced in chapter 4.3 - *Extended studies – An Electronically Tunable X-nuclei Surface Coil* is the input referred voltage noise spectral density of the used CMOS broadband, high impedance LNA.

The last part of this work is an enhancement of the CMOS broadband, high impedance LNA, achieving an input referred voltage noise spectral density of $200\,\mathrm{pV}/\sqrt{\mathrm{Hz}}$, which is in turn an improvement of approximately factor 5 related to the input referred voltage noise spectral density of the LNA used in chapter 4.3 - *Extended studies – An Electronically Tunable X-nuclei Surface Coil*.

4 Published articles and extended studies

4.1 An EM Simulation-Based Design Flow

This article [25] was published as

Horneff, A., Eder, M., Hell, E., Ulrici, J., Felder, J., Rasche, V. and Anders, J. An EM Simulation-Based Design Flow for Custom-Built MR Coils Incorporating Signal and Noise. *IEEE Transactions on Medical Imaging* 37.: 527–535, 2018

Own contribution:

Development of the simulation-based process for the design of MR coils. Implementation of simulations and the related calculations. Design and construction of the reference setup (construction of an MR coil and a suitable phantom) for comparative measurements. Carrying out the MRI measurements. Analysis and interpretation of the simulated/measured data (together with all co-authors). Writing of the manuscript, incorporating the comments of the co-authors and incorporating the revisions.

An EM Simulation-Based Design Flow for Custom-Built MR Coils Incorporating Signal and Noise

Andreas Horneff, Michael Eder, Erich Hell, Johannes Ulrici, Jörg Felder, Volker Rasche, and Jens Anders

***Abstract*— Developing custom-built MR coils is a cumbersome task, in which an *a priori* prediction of the coils' SNR performance, their sensitivity pattern, and their depth of penetration helps to greatly speed up the design process by reducing the required hardware manufacturing iterations. The simulation-based design flow presented in this paper takes the entire MR imaging process into account. That is, it includes all geometric and material properties of the coil and the phantom, the thermal noise as well as the target MR sequences. The proposed simulation-driven design flow is validated using a manufactured prototype coil, whose performance was optimized regarding its SNR performance, based on the presented design flow, by comparing the coil's measured performance against the simulated results. In these experiments, the mean and the standard deviation of the relative error between the simulated and measured coil sensitivity pattern were found to be $\mu = 1.79\%$ and $\sigma = 3.15\%$. Moreover, the peak deviation between the simulated and measured voxel SNR was found to be less than 4%, indicating that simulations are in good accordance with the measured results, validating the proposed software-based design approach.**

***Index Terms*— Software-based MR coil design, MR coil simulation, MR SNR simulation, MR image SNR simulation.**

I. Introduction

MAGNETIC resonance imaging (MRI) is a well-established imaging modality that is used in clinical routine as well as in research. For specific applications, where commercial coils are not available, the development of dedicated MR-coils is required. These custom designs typically provide a highly specialized geometry, to achieve an optimal signal-to-noise ratio (SNR) in the target application [1] as one of the most important performance metrics of an MRI system as well as MR image quality [2].

Therefore, a major problem when designing custom-made coils is the a priori, i.e. prior to manufacturing, missing information on its final SNR performance, its sensitivity pattern and its depth of penetration in the region of interest. Such an a priori knowledge, especially of the resulting SNR performance in the envisaged application, would help to speed up the design process because fewer or even no iterations are needed during the coil design.

Early work by Hoult and Richards [3] laid the theoretical foundations of SNR analysis. Based on this work, Hoult and Lauterbur [4] published the first studies on SNR in human imaging and showed that the SNR is proportional to the B_0-field if sample loss is dominant. Edelstein *et al.* [5] found that there is an upper limit that describes the maximum SNR performance of a coil for a given patient setup in an MRI system, which is called the intrinsic SNR (ISNR). All these methods assumed quasi-static conditions to calculate the B_1-field pattern of the transmit coil and the sensitivity pattern of the receive coil [6], [7]. However, these assumptions lose validity even at moderate field strengths ($\geq$ 0.5 T), because wave effects (e.g. radiation, standing waves) can occur [8], [9].

Although the wave nature of the electromagnetic fields can be taken into account in these methods by using the full Maxwell equations to calculate them, all theoretical approaches published until today had to assume homogenous subjects to simplify the problem and allow for closed form solutions [9], [10].

In contrast, computational electromagnetics methods (CEMs) are not limited to homogenous subjects. CEMs are well known in literature and are used to calculate the specific absorption rate (SAR) as well as the B_1-field pattern [11], [12]. Furthermore, CEMs can e.g. be used to analyze the field homogeneity [13], [14], power requirements [15], B_u^+ efficiency [16], [17] and sensitivity B_u^- [17], [18].

The goal of this paper is to predict the SNR performance of a custom-built MR coil incorporating its position relative to the

Manuscript received August 18, 2017; revised October 6, 2017; accepted October 12, 2017. Date of publication October 18, 2017; date of current version February 1, 2018. *(Corresponding author: Andreas Horneff.)*

A. Horneff is with ExCaVI, University Hospital Ulm, 89081 Ulm, Germany, and also with GME, Sirona Dental Systems, 64625 Bensheim, Germany (e-mail: andreas.horneff@dentsplysirona.com).

M. Eder and V. Rasche are with ExCaVI, University Hospital Ulm, 89081 Ulm, Germany (e-mail: michael.eder@uniklinik-ulm.de; volker.rasche@uniklinik-ulm.de).

E. Hell and J. Ulrici are with GME, Sirona Dental Systems, 64625 Bensheim, Germany (e-mail: erich.hell@sirona.com; johannes.ulrici@sirona.com).

J. Felder is with INM-4, Forschungszentrum Jülich, 52425 Jülich, Germany (e-mail: j.felder@fz-juelich.de).

J. Anders is with the Institute of Microelectronics, University of Ulm, 89081 Ulm, Germany (e-mail: jens.anders@uni-ulm.de).

Color versions of one or more of the figures in this paper are available online at http://ieeexplore.ieee.org.

Digital Object Identifier 10.1109/TMI.2017.2764160

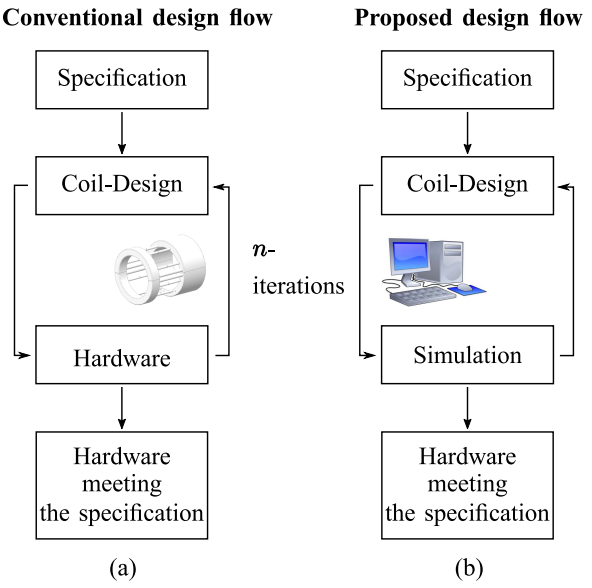

Fig. 1. Comparison of the conventional hardware-oriented coil design flow (a) and the software-based design flow proposed in this paper (b).

sample, its sensitivity pattern and its depth of penetration by CEM simulations before construction. To this end, the resulting MR image is simulated including the full geometric and material properties of both the coil and the phantom under investigation as well as the target MR sequences. Finally, the noise of the setup is calculated from physical principles and added to the simulated image. To validate the proposed simulation-driven design flow, we manufactured a prototype coil, whose SNR performance was optimized using the CEM-based approach, and compared its measured performance against the simulation results.

II. Theory and Methods

Fig. 1 illustrates our proposed coil design flow and contrasts it against the conventional design flow, which typically involves several hardware iterations to arrive at the desired performance.

In both design flows an initial coil design has to be found based on the specifications. Then, in the conventional design flow, a hardware prototype of said coil design is manufactured and its performance is iteratively improved by measuring the performance and modifying following generations of prototype coils accordingly until the specification is finally met. Naturally, using this approach, the required number of (costly) hardware iterations depends on the quality of the initial prototype, which in turn typically strongly depends on design experience.

In contrast, the proposed design flow greatly reduces or even removes the need for expensive hardware manufacturing and testing by executing the required design iterations using inexpensive software simulations. The simulated results can then be optimized using any desired algorithm. Therefore, ideally, only a single prototype has to be manufactured, which directly meets the specification. Naturally, in this design approach, the quality of the first manufactured prototype largely depends on the quality of the EM-simulations and the resulting SNR estimates used to predict the coil performance. Therefore, this topic will be discussed in detail in the following sections.

A. MR Signal Calculation

The first step for the simulation-based SNR estimation is the calculation of the contribution of each phantom voxel $V_{\mathrm{sig,voxel}}$ to the total voltage induced in the detection coil, V_{sig}.

For our calculation we will make the following assumptions, which are typically satisfied in conventional MR imaging experiments:

(i) The phantom is uniformly excited and the spins in each voxel are flipped by a constant flip angle, which, without loss of generality, will be taken as 90° in the following.

(ii) Steady state conditions apply, which can e.g. be ensured by choosing a long repetition time T_{R} compared to the relaxation time T_1, causing all spins in the phantom to be in thermal equilibrium before the next excitation pulse.

For spins after a 90° excitation, the magnetization components along the x- and y-axis, M_x and M_y, can be combined into a complex transversal magnetization phasor M_{trans} according to:

$$M_{\mathrm{trans}} = M_x + iM_y \tag{1}$$

$$= M_{\mathrm{abs}} \cdot \mathrm{e}^{i\varphi_M}, \tag{2}$$

where the transversal M_{abs} is the phasor amplitude and φ_M its phase. Assuming thermal polarization in a static field B_0, the absolute value of the magnetization M_{abs} of a proton spin ensemble is given by [1]:

$$M_{\mathrm{abs}} = \frac{\rho\gamma_{\mathrm{n}}^2\hbar^2\ B_0}{4\ k_{\mathrm{B}}T_{\mathrm{phantom}}}, \tag{3}$$

where ρ is the proton density, γ_{n} is the gyromagnetic ratio (for ^{1}H, $\gamma_{^1\mathrm{H}}/2\pi = 42.55$MHz/T) [19]), k_{B} is the Boltzmann constant, T_{phantom} is the temperature of the phantom and $\hbar$ is the reduced Planck constant ($\hbar = h/2\pi$).

Based on the magnetization of each voxel (see (3)), its contribution to the resulting induced voltage in the receive coil, $V_{\mathrm{sig,voxel}}$, can be calculated based on the reciprocity principle. To this end, the sensitivity B_{u}-field has to be found, which is defined as

$$\mathbf{B}_{\mathrm{u}}(t) = \frac{\mathbf{B}_1(t)}{I(t)}, \tag{4}$$

where $\mathbf{B}_1(t)$ is the magnetic field produced by the coil current $I(t)$.

B_{u}^- is the left circularly polarized component of the B_{u}-field, which rotates in a plane perpendicular to the static magnetic B_0-field [20]. It can be expressed as [20]

$$\mathbf{B}_{\mathrm{u}}^- = \frac{B_{\mathrm{u},x} + iB_{\mathrm{u},y}}{2}, \tag{5}$$

where $B_{\mathrm{u},x}$ and $B_{\mathrm{u},y}$ are the x- and y-components of the B_{u}-field.

From (3) and (5), we find the absolute value of the induced voltage originating from a single pixel according to [19]

$$V_{\mathrm{sig,voxel}} = \omega_0 \iiint\limits_{V_{\mathrm{voxel}}} |\mathbf{B}_{\mathrm{u}}^{-}| \cdot |\mathbf{M}_{\mathrm{trans}}| \, \mathrm{d}V, \tag{6}$$

where ω_0 (see (7)) is the absolute value of the angular Larmor frequency. Assuming proton imaging as the target nucleus, ω_0 is given by [19]

$$\omega_0 = \gamma_{^1\mathrm{H}} B_0, \tag{7}$$

where $\gamma_{^1\mathrm{H}}$ is the gyromagnetic ratio of protons and B_0 is the static magnetic field strength.

B. Noise Calculation

Having calculated the signal generated by the phantom, it remains to assess also the noise floor of the system. Ideally, this noise floor is determined by the thermal noise of the coil, $V_{\mathrm{n,coil}}$, and the thermal noise associated with losses in the sample / phantom, $V_{\mathrm{n,phantom}}$. However, in any real-world system, the noise floor is also affected by the noise figure (NF) of the electronics in the receiver chain, which will be accounted for in section IV-B.

Since these two noise sources are uncorrelated, their corresponding variances need to be added according to

$$V_{\mathrm{n,tot}} = \sqrt{V_{\mathrm{n,coil}}^2 + V_{\mathrm{n,phantom}}^2}, \tag{8}$$

to obtain the total Root Mean Square (RMS) noise floor [21]. To simplify the design flow, one can make use of the fact that, depending on the coil size, one of the two noise sources can largely dominate the total noise floor. A method to estimate the dominant noise source is shown in [22].

Based on the fluctuation dissipation theorem [23], the RMS noise voltage of the coil can be calculated as [9]

$$V_{\mathrm{n,coil}} = \sqrt{4 \, k_{\mathrm{B}} T R_{\mathrm{coil}} \Delta f}, \tag{9}$$

where T is the coil temperature, R_{coil} is the real part of the coil impedance at the frequency of interest and Δf is the pixel bandwidth. In the proposed CEM-based design flow, R_{coil} can be extracted from S-Parameter simulations at the frequency of interest. The RMS noise voltage of the phantom is given by [9]

$$V_{\mathrm{n,phantom}} = \sqrt{4 \, k_{\mathrm{B}} T R_{\mathrm{phantom}} \Delta f}, \tag{10}$$

where R_{phantom} is an equivalent resistance modeling the dielectric sample losses. To compute R_{phantom}, we can define

$$P_{\mathrm{phantom}} = R_{\mathrm{phantom}} \cdot I_{\mathrm{rms}}^2, \tag{11}$$

where P_{phantom} is the power dissipated in the sample. Since the loss in the sample physically originates from conductive and dielectric losses due to the finite sample conductance, P_{phantom} can also be written according to [1], [9]

$$P_{\mathrm{phantom}} = \iiint\limits_{V_{\mathrm{sample}}} |\mathbf{E}_{\mathrm{rms}}|^2 \cdot \sigma_{\mathrm{e}} \, \mathrm{d}V, \tag{12}$$

where $\mathbf{E}_{\mathrm{rms}}$ is the root mean square of the electric field inside the sample and $\sigma_{\mathrm{e}} = \sigma_{\mathrm{s}} + \omega_0 \epsilon''$ is the total sample conductance. Here, σ_{s} is the electrical conductivity of the sample, and ϵ'' is the imaginary part of its complex permittivity. Then, by replacing the E-field in (12) with a unitary E-field similar to the unitary magnetic field B_{u} according to:

$$\mathbf{E}_{\mathrm{rms}}(t) = \mathbf{E}_{\mathrm{u}}(t) \cdot I_{\mathrm{rms}}(t), \tag{13}$$

R_{phantom} can finally be computed from

$$R_{\mathrm{phantom}} = \iiint\limits_{V_{\mathrm{sample}}} \mathbf{E}_{\mathrm{u}}^2 \cdot \sigma_{\mathrm{e}} \, \mathrm{d}V. \tag{14}$$

Having calculated the coil and phantom noise according to (10) and (14), the effect of the noise floor of the receiver chain on the overall SNR needs to be taken into account by its NF to obtain an adequate estimate of the achievable system performance.

C. SNR Calculation and Measurement

In this section, the results of the previous two sections are combined to obtain an estimation of the achievable SNR and the theoretical background, which is required to compare said SNR against measured results, is provided.

1) SNR Calculation: The SNR of each voxel can be written as [24]

$$\mathrm{SNR}_{\mathrm{voxel}} = \frac{V_{\mathrm{sig,voxel}}}{V_{\mathrm{n,tot}}} \sqrt{N_{\mathrm{PE}}} \sqrt{N_{\mathrm{avg}}}, \tag{15}$$

where N_{PE} is the number of phase encoding steps, N_{avg} is the number of averages for each phase encoding step and $V_{\mathrm{sig,voxel}}$ and $V_{\mathrm{n,tot}}$ can be computed according to Sections II-A and II-B, respectively [24].

2) SNR Measurement: The SNR of MR images can be determined by the standardized methods described in the National Electrical Manufacturers Association (NEMA) Standard Publication MS 1-2008 [25]. Since we want to calculate the SNR based on a magnitude image, the method number 4 of the standard is used. Because of the off-center FOV, we determine the image noise from a noise measurement region of interest (NROI) at the bottom of the image as indicated by the blue squares in Fig. 6, to ensure that the NROI is well separated from the signal producing phantom. Since a magnitude image is evaluated, the noise regions will not display a Gaussian distribution because the rectification due to the absolute value operation produces a Rayleigh distribution [24], [25].

According to the NEMA standard, the standard deviation of the noise in the complex domain $\hat{\sigma}_{\mathrm{N}}$ can be found in two different ways:

The first way is the estimation based on the standard deviation of the measured noise given by

$$\hat{\sigma}_{\mathrm{N},\sigma} = \frac{\hat{\sigma}\left(I_{\mathrm{N},1}, \ldots, I_{\mathrm{N},i}\right)}{0.66}, \tag{16}$$

where $I_{\mathrm{N},1}, \ldots, I_{\mathrm{N},i}$ describe the intensity levels of each noise voxel.

The second way to estimate the noise is based on the measured mean noise level $\hat{\mu}$ according to

$$\hat{\sigma}_{\mathrm{N},\mu} = \frac{\hat{\mu}\left(I_{\mathrm{N},1}, \ldots, I_{\mathrm{N},i}\right)}{1.25}. \tag{17}$$

The estimation based on the standard deviation is indicated by the additional index σ, the estimation based on the mean noise level is indicated by the index μ. Although both ways of estimation are valid, the estimation based on $\hat{\sigma}$ is recommended in the standard. For truly Rayleigh-distributed noise both estimates provide the same result, i.e. $\hat{\sigma}_{\mathrm{N},\mu} = \hat{\sigma}_{\mathrm{N},\sigma}$. The advantage of the method based on the mean noise level is a lower sensitivity to image artifacts.

To determine the image signal intensity $\hat{S}$, a signal ROI has to be defined. To this end, all voxels with a signal intensity $I_i \geq 6 \cdot \sigma_{\mathrm{N}}$ are assumed to be signal voxels [24], see Fig. 6, ROI framed by a red line. The image signal intensity is then determined from the mean voxel value $\hat{S} = \hat{\mu}\left(I_{\mathrm{S},1}, \ldots, I_{\mathrm{S},i}\right)$ insight the signal ROI and the SNR can be computed according to

$$\mathrm{SNR} = \frac{\hat{S}}{\hat{\sigma}_{N,\sigma,\mu}}. \tag{18}$$

III. Simulation Tools

In this section, the simulation tools are introduced and their use in the proposed work flow is described in detail.

A. Coil Design and Field Simulation Using CST MICROWAVE STUDIO

In the proposed work flow, the geometry of the coil and the phantom are designed in CST MICROWAVE STUDIO® (CST-MWS) including the different electrical and magnetic properties of the utilized coil and phantom materials. CST-MWS is a tool for 3D electromagnetic simulations of high frequency components [26]. One of the major benefits of the proposed design approach is that elements can be conveniently defined as parametrized geometries, which allows for an easy design modification as well as a fine tuning using a local optimizer and/or parametrized sweeps.

In order to be able to validate the proposed design flow using measured data from a manufactured prototype, we designed a prototype coil with a target operating frequency corresponding to the Larmor frequency of our 3T-MRI scanner (Achieva 3.0T, Philips, Eindhoven, Netherlands). The target Larmor frequency is calculated using (7), resulting in $f_0 = \omega_0/(2 \cdot \pi) = 127.8\,\mathrm{MHz}$ for our system.

In the proposed design methodology, CST-MWS is first used to simulate the unitary B_{u}- and the E_{u}-fields. The EM simulation is performed using the transient solver. The results generated by this solver are based on a hexahedral mesh, hence they can be imported to Jemris and MATLAB without transformation. Using this solver, a Gaussian or rising sinus has to be used as excitation signal, to obtain steady state condition. If the excitation signal is not set to $I(t) = 1\mathrm{A}\sin(\omega_0 t)$, the B_{u}- and the E_{u}-fields have to be divided by the current in the coil at the Larmor frequency ω_0.

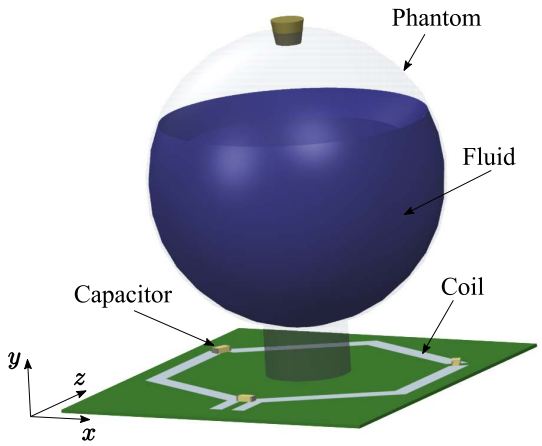

Fig. 2. Coil and phantom setup designed in CST-MWS.

Then, according to Section II-A and II-B, from the unitary fields, the image signal and noise levels can be computed, which finally allows to estimate the achievable SNR.

B. Jemris Toolbox

Jemris is an open-source MRI simulation toolbox. It is an extensible MRI simulation framework which provides an MRI sequence development and simulation environment for the MRI community. Jemris numerically solves the Bloch equation individually for the spin ensemble of each voxel [27] by using the B_{u}-field, which can be exported from CST-MWS as a 3D-array, to incorporate the sensitivity profile of the coil at hand into the simulation. The individual phantom properties can be incorporated in Jemris by exporting a voxel model from CST, whose resolution is determined by the resolution of the CST-MWS simulation. This voxel model of the phantom contains the electromagnetic parameters as well as MR related information (e.g. the relaxation times T_1 and T_2). Based on the B_{u}-field and the phantom voxel model, Jemris can simulate the resulting MR image of the phantom.

IV. Simulation, Data Acquisition, and Verification

In this section, we will illustrate the design flow using the prototype design for our 3T-MRI scanner mentioned above.

A. Simulation of a Coil / Phantom Setup

1) Coil and Field Simulation of the Setup Using CST MICROWAVE STUDIO: Fig. 2 shows the design and the arrangement of the coil and the phantom. The phantom is a hollow glass sphere with a diameter of 80 mm filled with water, which is doped with $CuSO_4$ and NaCl (1 liter H_2O, 3.6 g NaCl and 1.25 g of pure $CuSO_4$) for a convenient adjustment of the relaxation times in the imaging experiments on the manufactured prototype. The sphere is located on a spacer in the center of the surface coil, resulting in a distance of 17 mm between the sphere and the coil. The coil is made from a single copper trace on a printed circuit board (PCB), which is intersected by three series capacitors. To allow for an easy

import of the simulated B_u-fields into Jemris, a hexahedral mesh should be used for the CST-simulations. If a different mesh is used, the simulation results have to be regridded using a numerical mathematics software such as MATLAB (Mathworks Inc., Natick, USA).

The CST-simulations were performed with a resolution (mesh-size) of 0.5 mm × 0.5 mm × 0.5 mm, which then also determines the maximum possible resolution of the Jemris simulations. The CST-simulations were performed on a dedicated simulation PC (2 × 10 core Intel Xeon E5-2650 v3 @ 2.30GHz, 64.0GB RAM, 1 × NVIDIA Quadro K4200, Windows 7) resulting in a simulation time of about 40 min.

The Jemris software was installed under LINUX Ubuntu 14.04 LTS. Using Jemris' built-in multi PC computation feature, we configured the Jemris simulation to run on two of the above mentioned simulation PCs in parallel, leading to a simulation time of approximately 2 h.

2) Simulation of a Phantom Slice Using the Jemris Toolbox: Based on the B_u-field and the phantom voxel model, Jemris was used to simulate an image of a single slice with a thickness of $d = 10$ mm through the center of the phantom. The relaxation times of the phantom fluid were $T_1 = (161 \pm 11)$ ms and $T_2 = (123 \pm 3)$ ms (measured). Because the simulated coil is receive only, in the simulation, a homogeneous excitation from an external coil was assumed, which later in the experiments was produced by the body coil of the scanner.

For the simulation and the experiments, a gradient echo sequence (GRE) was used. The echo time of the sequence was set to $T_E = 15$ ms, the repetition time to $T_R = 1000$ ms and the flip angle was 90°.

Further, we have assumed B_0 is aligned along the $+z$-axis (see Fig. 2). The simulated slice was selected in the x/y-plane. The field of view (FOV) was 120 mm × 120 mm × 10 mm ($x \times y \times z$) with a resolution of 0.5 mm × 0.5 mm × 10 mm, which corresponds to the resolution used for the measurements mentioned above.

3) Calculating the Noise of the Setup: To obtain the simulated SNR, the phantom noise was calculated based on the E_u-field simulated by CST-MWS and $V_{n,tot}$ was then calculated for every voxel as described in chapter II-B, based on the properties of the phantom material. Finally, the simulated noise was added to the Jemris-image in MATLAB.

B. Data Acquisition

In order to validate the proposed design flow, the coil-phantom combination, which was previously simulated in CST-MWS and Jemris, was manufactured and MR imaging experiments were performed on a 3T scanner. To avoid any unknown influence from the manufacturers' front/back-end, a custom-built receive path and a dedicated sampling unit (EVO MRI spectrometer, MR Solutions, Guildford, United Kingdom) were interfaced to the scanner to ensure full knowledge of the receive path.

The structure and the dimensions of the surface coil are shown in Fig. 3. The coil consists of six equal trace elements with a length of 40 mm and a width of 6 mm, arranged as a hexagonal structure with a size of 80 mm by 68 mm.

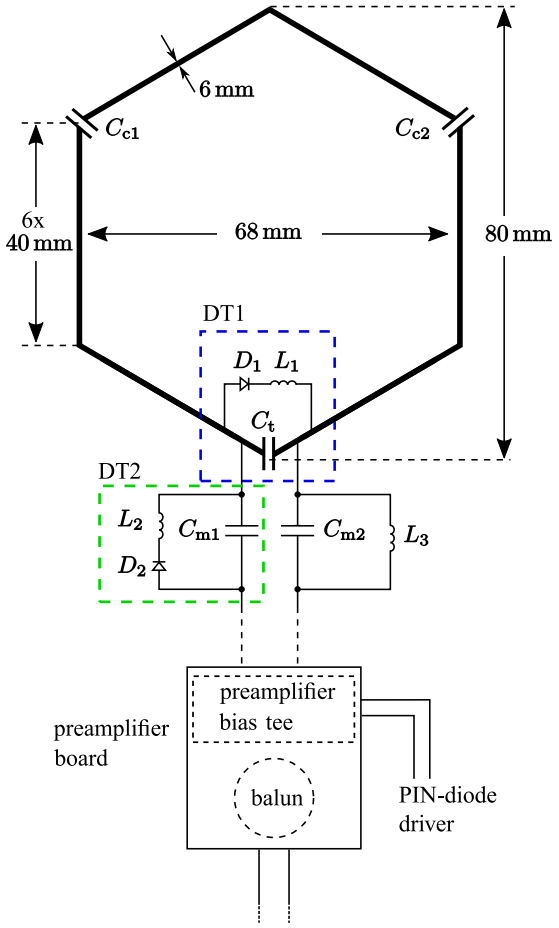

Fig. 3. Schematic illustration of the coil's structure and its dimensions.

The coil is divided into three sections using capacitors C_{c1} and C_{c2}. Tuning and matching to 50Ω are performed using the parallel capacitor C_t and the series capacitors C_{m1} and C_{m2}, respectively. All assembled capacitors are non-magnetic surface-mount devices (SMDs) with a package size of 1111 (EXXELIA TEMEX (CHB-Series), Paris, France).

Capacitors C_{c1} and C_{c2} both have a value of 32 pF. The tuning capacitor C_t has a total value of about 27 pF, made up of a fixed capacitance of 22 pF and a variable capacitor with a range from 3 pF to 10 pF (SGC3S100, Sprague Goodman, New York, USA). Matching capacitors C_{m1} and C_{m2} take on values of 9.7 pF and 4.7 pF, respectively. The coil is detuned using a PIN diode that switches a detune circuit to its on state during the excitation pulse, which is applied by the body coil of the scanner [28], [29]. To provide a sufficient total detuning, there are two detune circuits (DT1 and DT2) used in the setup. DT1 consists of capacitor C_t, a PIN-Diode D_1 (MADP-000235-10720T, MACOM, Lowell, USA) and an inductor $L_1 = 47$ nH (1008CS-Series, Coilcraft, Cary IL, USA). DT2 consists of capacitor C_{m1}, a PIN-Diode D_2 (MADP-000235-10720T, MACOM, Lowell, USA) and an inductor $L_2 = 150$ nH (1008CS-Series, Coilcraft, Cary IL, USA).

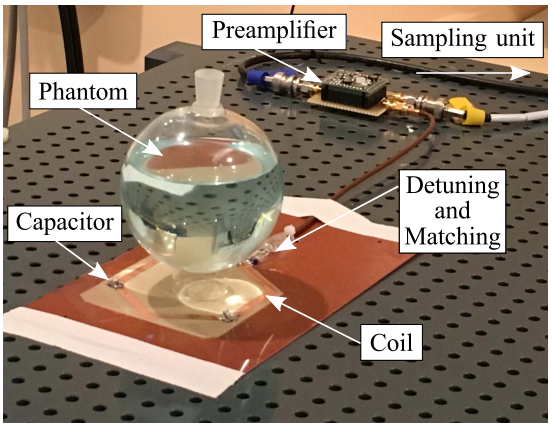

Fig. 4. Measurement setup for the manufactured phantom and coil. The coil is placed on the scanner table and connected to the preamplifier. In the center of the coil, the phantom is placed on a spacer with an distance of 17 mm. The preamplifier is connected to the sampling unit.

The inductor $L_3 = 10\,\mu\text{H}$ (1812CS-Series, Coilcraft, Cary IL, USA) acts as an RF choke, which passes the DC current that switches DT1 and DT2 to their on state by the PIN-diode driver, but blocks any RF signal. The PIN diode driver itself is connected via a bias tee which is included in the preamplifier board.

The assembled measurement setup is shown in Fig. 4. The measured coil quality factor is approximately $Q_{\text{unloaded}} = 115$ in air and $Q_{\text{loaded}} = 50$ when loaded with the phantom. The phantom is placed on top of the coil on the scanner table using a spacer resulting in a coil phantom distance of $d = 17\,\text{mm}$.

The coil is connected to the preamplifier, which is in turn connected to the dedicated sampling unit. According to its data sheet, the NF of the used preamplifier is 0.6 dB.

The connection cable (V45466-B12-G17 (RG316), LEONI Special Cables GmbH, Friesoythe, Germany) between the coil and the preamp has a length of 25 cm. The typical attenuation of this cable is about 27 dB/100 m at 100 MHz (datasheet). With this attenuation, the cable increases the system noise figure by about 0.07 dB.

To allow for a comparison, the settings of the measurements were identical to those of the Jemris-simulations (see chapter IV-A2).

V. Results

A. Signal Intensity Pattern of the Simulated and Measured Image

To be able to compare the intensity pattern of the simulated and the measured MR image, both images were normalized to relative intensities between 0-100% and the simulated image was subtracted from the measured one. Fig. 5a shows the resulting variation of the signal distribution between the measured and the simulated image in percent. Fig. 5b-e shows the deviation of the intensity pattern for every pixel projected along the lines h1, h2, v1 and v2, that are shown in blue in Fig. 5a. The region between the two green lines in Fig. 5b-e is the inner region of the phantom. Here it should be noted

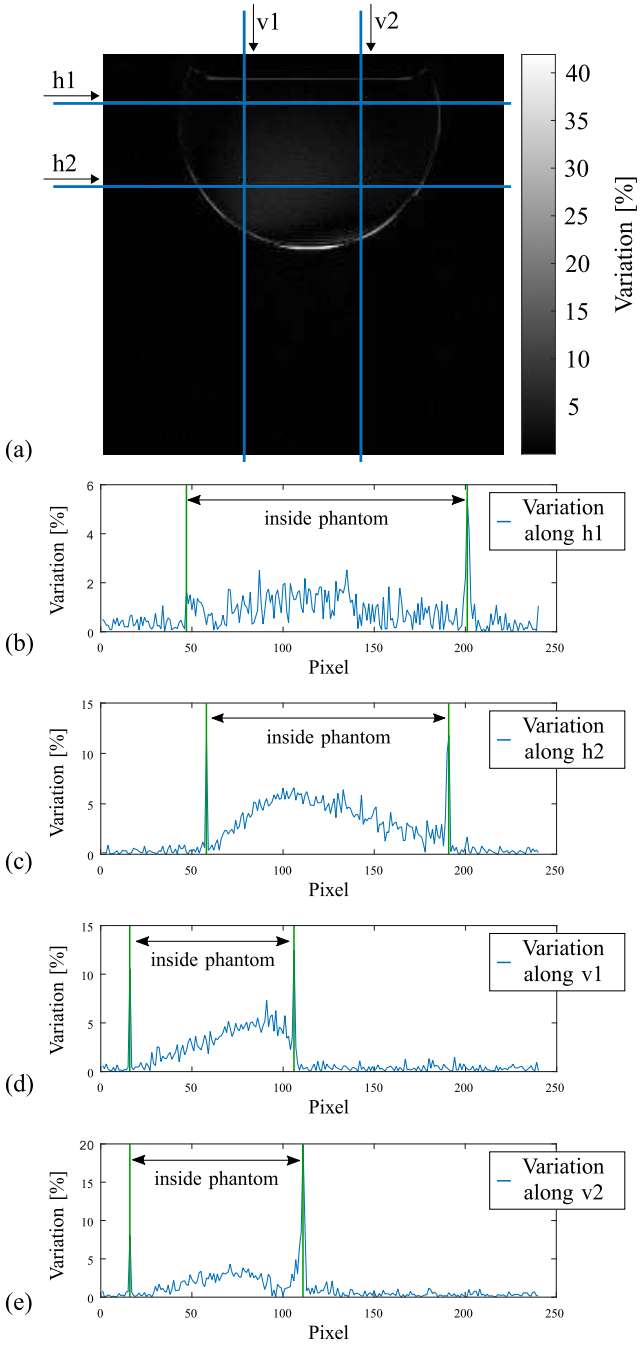

Fig. 5. (a) Differences between simulated and measured phantom in a single slice. (b)-(d) Difference between simulated and measured image projected along lines h1, h2, v1 and v2, shown as blue lines in (a). The region between the green lines in (b)-(e) is the inner region of the phantom.

that the largest mismatches occur in the border region of the phantom, which is affected by the manufacturing tolerances of the glass phantom container.

The resulting mean and the standard deviation of the difference between the simulated and the measured signal intensities (including the mismatches in the border region due to the manufacturing tolerances) are $\mu = 1.79\,\%$ and $\sigma = 3.15\,\%$.

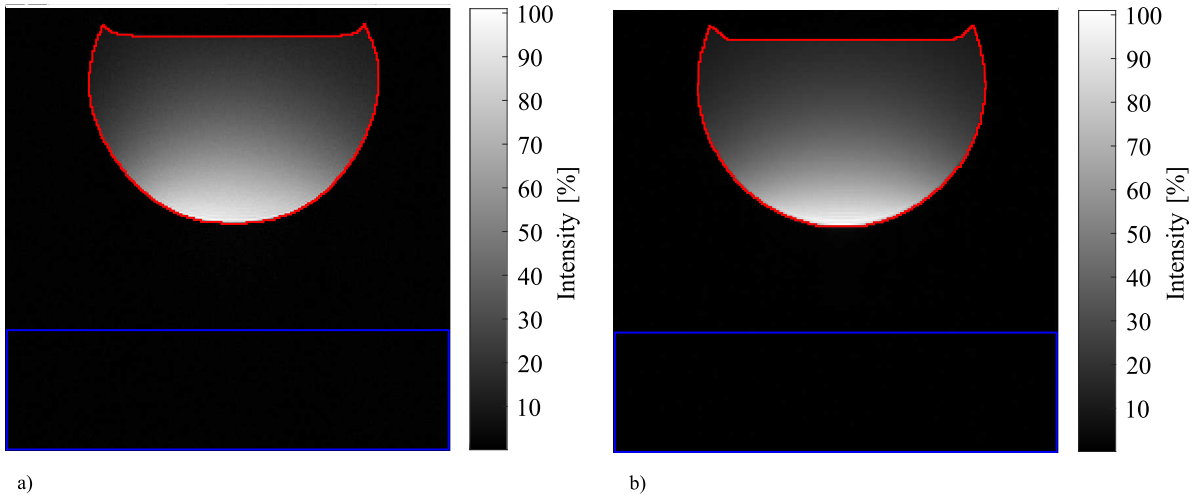

Fig. 6. (a) Measured and (b) simulated MR image. The noise ROIs are indicated by blue squares and the signal ROIs are framed by a red line. The images are not sensitivity corrected.

B. SNR of the Simulated and Measured Image

The image in Fig. 6a shows the measured phantom image, Fig. 6b shows the simulated phantom image. The noise ROIs are indicated by blue squares, the signal ROIs are framed by a red line.

The corresponding SNR values are $\mathrm{SNR}_{\mathrm{sim}} = 56$ for the simulated and $\mathrm{SNR}_{\mathrm{measure}} = 54$ for the measured image. For the simulated noise values, the thermal noise of the coil, the thermal noise of the phantom, the attenuation of the cable between the coil and the preamplifier and the noise figure of the preamplifier (NF = 0.6 dB) were considered in the estimation.

VI. Extension to Coil Arrays

In order to apply the proposed design methodology to arrays of MR coils, which are becoming increasing popular due to their in many cases superior performance [30]–[32], the proposed design flow has to be extended to incorporate the influence of noise coupling between neighboring array coils. The total noise coupling of the array can be calculated from the noise correlation of the array elements and their Z-parameter matrix, which jointly fully describe the array noise originating in the lossy sample and the coil resistance. Here, similar to the single-coil case, three regimes can be distinguished [22]:

(i) sample noise dominated regime,
(ii) coil noise dominated regime,
(iii) a regime in which both noise significantly contribute to the total system noise.

In the following, it will be explained how the array noise coupling can be modeled in these three cases:

A. Sample Noise Dominated Regime

The noise coupling due to sample noise originates from the E-field coupling of the individual array coils, which can be calculated from the unitary E-field of each array coil i, $\mathbf{E}_{\mathrm{u},i}$, by integrating the dot product $\mathbf{E}_{\mathrm{u,i}} \cdot \mathbf{E}_{\mathrm{u,j}}$ over the entire sample volume according to [33]

$$R_{i,j} = \iiint_{V_{\mathrm{sample}}} \mathbf{E}_{\mathrm{u},i} \cdot \mathbf{E}_{\mathrm{u},j} \cdot \sigma_{\mathrm{e}} \, \mathrm{d}V, \tag{19}$$

where $\mathbf{E}_{\mathrm{u},i}$ and $\mathbf{E}_{\mathrm{u},j}$ represents the unitary E-field of array elements i and j and $\sigma_{\mathrm{e}} = \sigma_{\mathrm{s}} + \omega_0 \epsilon''$ is the total sample conductance.

The RMS noise voltage $V_{\mathrm{n,phantom,i}}$ of array element i is then given by

$$V_{\mathrm{n,phantom,i}} = \sqrt{4\, k_{\mathrm{B}} T \sum_{j=1}^{N_{\mathrm{coil}}} R_{i,j} \cdot \Delta f}, \tag{20}$$

where N_{coil} is the number of array (coil) elements.

B. Coil Noise Dominated Regime

In this case, one can use CST-MWS to simulate the Z-parameter matrix corresponding to the coil array to estimate the influence of coil coupling on the overall noise floor. Here the RMS noise voltage $V_{\mathrm{n,coil,i}}$ of array element i can be calculated from

$$V_{\mathrm{n,coil,i}} = \sqrt{4\, k_{\mathrm{B}} T \sum_{j=1}^{N_{\mathrm{coil}}} \mathrm{Re}\left\{Z_{i,j}\right\} \cdot \Delta f}, \tag{21}$$

where $Z_{i,j}$ is the corresponding value of the Z-parameter matrix for array elements i and j.

C. Regime With Significant Contributions From Both Noise Sources

As mentioned in Section II-B, since the two noise sources $V_{\mathrm{n,phantom,i}}$ and $V_{\mathrm{n,coil,i}}$ are uncorrelated, their corresponding

variances can be added and the total RMS noise voltage of array element i therefore becomes:

$$V_{\mathrm{n,tot,i}} = \sqrt{V^2_{\mathrm{n,phantom,i}} + V^2_{\mathrm{n,coil,i}}}. \tag{22}$$

Finally, in addition to the 3D-simulation environment, CST-Microwave Studio also offers a so called "Schematic-Editor". This Editor offers the possibility to simulate the expected performance when connecting the array coils with different electrical circuits. This feature can then be used to also incorporate more circuit related aspects such as preamp decoupling into the proposed design flow.

VII. Discussion

In prior work, several methods were proposed, to evaluate the SNR performance and/or the field homogeneity of a coil. However, these methods focused only on subaspects of a final MR image.

In contrast, in this paper, a method, which allows to both simulate the expected signal pattern, the image noise and thereby also the final SNR performance of a coil in the region of interest was introduced. In addition to estimating the SNR, the proposed design flow also allows for the simulation of the sensitivity pattern and the depth of penetration for a given coil setup. Based on this information and thanks to the very good accuracy of the simulation data, this workflow can be used to optimize a coil for its MR performance in a given target application without the need for costly hardware iterations, i.e. purely based on simulations. The optimization itself can then be carried out using any desired optimization procedure, starting from a simple parameter sweep over using CST's built-in optimizers to using elaborate custom-made optimization algorithms, e.g. implemented in MATLAB.

The simulation of custom-made receive coils including the coil geometry, the phantom properties (including material properties), as well as the thermal phantom and coil noise and the noise figure of the preamplifier was shown to be feasible, thus allowing an a priori estimation of the final MR image and its SNR for specific applications. The remaining differences in the SNR estimation of about 4% may be attributed to the missing information on the NF of the sampling unit, indicating the requirement for better characterized components (e.g. with the method proposed in [34]) and the B_1+ non-uniformity during TX caused by coupling into the surface coil. The reason for the latter is the RF current in the RX coil resulting from a finite impedance in the RX coil termination during TX due to imperfect detune circuits. The difference between the simulated and measured results for the coil sensitivity is very small with a mean and a standard deviation of $\mu = 1.79\,\%$ and $\sigma = 3.15\,\%$. Some remaining mismatches at the border of the phantom can be attributed to manufacturing inaccuracies of the handmade phantom, which was not perfectly spherical and only carries weight at the border of the phantom (see Fig. 5).

The feasibility of the proposed approach was shown on a simple setup only. However, with the presented method it is possible to also simulate more complex phantoms, including human body models, to achieve a better prediction of the SNR in different tissues. This in turn enables the design of a coil for a dedicated application without the need for costly hardware iteration cycles with their required time-consuming measurement-based performance evaluations. A second possible application for the proposed simulation flow is the estimation of the local contrast of transmit / receive coils in phantoms or human body models. Since the presented method embraces a complete MRI simulation framework, it can be used to evaluate the usability of coils for special sequences, too.

References

[1] W. Myers *et al.*, "Calculated signal-to-noise ratio of MRI detected with SQUIDs and Faraday detectors in fields from 10 μT to 1.5 T," *J. Magn. Reson.*, vol. 186, no. 2, pp. 182–192, 2007.

[2] O. Dietrich, J. G. Raya, S. B. Reeder, M. F. Reiser, and S. O. Schoenberg, "Measurement of signal-to-noise ratios in MR images: Influence of multichannel coils, parallel imaging, and reconstruction filters," *Magn. Reson. Imag.*, vol. 26, pp. 375–385, Aug. 2007.

[3] D. I. Hoult and R. E. Richards, "The signal-to-noise ratio of the nuclear magnetic resonance experiment," *J. Magn. Reson.*, vol. 24, no. 1, pp. 71–85, Oct. 1976.

[4] D. I. Hoult and P. C. Lauterbur, "The sensitivity of the zeugmatographic experiment involving human samples," *J. Magn. Reson.*, vol. 34, no. 2, pp. 425–433, 1979.

[5] W. A. Edelstein, G. H. Glover, C. J. Hardy, and R. W. Redington, "The intrinsic signal-to-noise ratio in NMR imaging," *Magn. Reson. Med.*, vol. 3, no. 4, pp. 604–618, 1986.

[6] J. Wang, A. Reykowski, and J. Dickas, "Calculation of the signal-to-noise ratio for simple surface coils and arrays of coils [magnetic resonance imaging]," *IEEE Trans. Biomed. Eng.*, vol. 42, no. 9, pp. 908–917, Sep. 1995.

[7] P. B. Roemer and W. A. Edelstein, "Ultimate sensitivity limits of surface coils," in *Proc. SMRM 6th Annu. Meet.*, New York, NY, USA, 1987, p. 410.

[8] G. Glover *et al.*, "Comparison of linear and circular polarization for magnetic resonance imaging," *J. Magn. Reson.*, vol. 64, no. 2, pp. 255–270, 1985.

[9] O. Ocali and E. Atalar, "Ultimate intrinsic signal-to-noise ratio in MRI," *Magn. Reson. Med.*, vol. 39, no. 3, pp. 462–473, 1998.

[10] H. Vesselle and R. E. Collin, "The signal-to-noise ratio of nuclear magnetic resonance surface coils and application to a lossy dielectric cylinder model—Part I: Theory," *IEEE Trans. Biomed. Eng.*, vol. 42, no. 5, pp. 497–509, May 1995.

[11] D. Šimunić, P. Wach, W. Renhart, and R. Stollberger, "Spatial distribution of high-frequency electromagnetic energy in human head during MRI: Numerical results and measurements," *IEEE Trans. Biomed. Eng.*, vol. 43, no. 1, pp. 88–94, Jan. 1996.

[12] Y. Pang, E. W. Wong, B. Yu, and X. Zhang, "Design and numerical evaluation of a volume coil array for parallel MR imaging at ultrahigh fields," *Quant Imag. Med. Surg.*, vol. 4, no. 1, pp. 50–56, 2014.

[13] J. M. Jin, J. Chen, W. C. Chew, H. Gan, R. L. Magin, and P. J. Dimbylow, "Computation of electromagnetic fields for high-frequency magnetic resonance imaging applications," *Phys. Med. Biol.*, vol. 41, no. 12, p. 2719, 1996.

[14] J. Jin and J. Chen, "On the SAR and field inhomogeneity of birdcage coils loaded with the human head," *Magn. Reson. Med.*, vol. 38, no. 6, pp. 953–963, 1997.

[15] T. Ibrahm and L. Tang, "Insight into RF power requirements and B_1 field homogeneity for human MRI via rigorous FDTD approach," *J. Magn. Reson. Imag.*, vol. 25, no. 6, pp. 1235–1247, 2007.

[16] N. Avdievich, A. Pfrommer, I. Giapitzakis, and A. Henning, "Analytical modeling of the coupling within a human head surface loop transmit phased array at ultra-high fields," in *Proc. ISMRM*, 2016, p. 3525.

[17] X. Yan, X. Zhang, L. Wei, and R. Xue, "Magnetic wall decoupling method for monopole coil array in ultrahigh field MRI: A feasibility test," *Quant. Imag. Med. Surg.*, vol. 4, no. 2, pp. 79–86, 2014.

[18] Y. Pang, B. Wu, C. Wang, D. B. Vigneron, and X. Zhang, "Numerical analysis of human sample effect on RF penetration and liver MR imaging at ultrahigh field," *Concepts Magn. Reson. B, Magn. Reson. Eng.*, vol. 39B, no. 4, pp. 206–216, 2011.

[19] J. Jin, *Electromagnetic Analysis and Design in Magnetic Resonance Imaging*, vol. 1. Boca Raton, FL, USA: CRC Press, 1999, p. 14.

[20] P.-M. Robitaille and L. Berliner, *Ultra High Field Magnetic Resonance Imaging*, vol. 26. New York, NY, USA: Springer, 2006, p. 186.
[21] M. Blencowe, *Designing High-Fidelity Valve Preamps*, vol. 1. Chantilly, VA, USA: Merlin Blencowe, 2016, p. 192.
[22] K. M. Gilbert, T. J. Scholl, and B. A. Chronik, "RF coil loading measurements between 1 and 50 MHz to guide field-cycled MRI system design," *Magn. Reson. Eng.*, vol. 33B, no. 3, pp. 177–191, 2008.
[23] J. Weber, "Fluctuation dissipation theorem," *Phys. Rev.*, vol. 101, no. 6, pp. 1620–1626, 1956.
[24] J. Anders, J. Handwerker, M. Ortmanns, and G. Boero, "A low-power high-sensitivity single-chip receiver for NMR microscopy," *J. Magn. Reson.*, vol. 266, pp. 41–50, May 2016.
[25] *Determination of Signal-to-Noise Ratio (SNR) in Diagnostic Magnetic Resonance Imaging*, NEMA Standard MS 1-2008 (R2014), 2015.
[26] CST MICROWAVE STUDIO. (2016) *CST—Computer Simulation Technology*. [Online]. Available: https://www.cst.com/products/CSTMWS/
[27] T. Stöcker, K. Vahedipour, D. Pflugfelder, and N. J. Shah, "High-performance computing MRI simulations," *Magn. Reson. Med.*, vol. 64, no. 1, pp. 186–193, 2010.
[28] W. A. Edelstein, C. J. Hardy, and O. M. Mueller, "Electronic decoupling of surface-coil receivers for NMR imaging and spectroscopy," *J. Magn. Reson.*, vol. 67, no. 1, pp. 156–161, 1986.
[29] M. Twieg, M. A. de Rooij, and M. A. Griswold, "Active detuning of MRI receive coils with GaN FETs," *IEEE Trans. Microw. Theory Techn.*, vol. 63, no. 12, pp. 4169–4177, Dec. 2015.
[30] P. B. Roemer, W. A. Edelstein, C. E. Hayes, S. P. Souza, and O. M. Mueller, "The NMR phased array," *Magn. Reson. Med.*, vol. 16, no. 2, pp. 192–225, 1990.
[31] H. Fujita, "New horizons in MR technology: RF coil designs and trends," *Magn. Reson. Med. Sci.*, vol. 6, no. 1, pp. 29–42, 2007.
[32] B. Keil and L. L. Wald, "Massively parallel MRI detector arrays," *J. Magn. Reson.*, vol. 229, pp. 75–89, Apr. 2013.
[33] C. M. Collins and Z. Wang, "Calculation of radiofrequency electromagnetic fields and their effects in MRI of human subjects," *Magn. Reson. Med.*, vol. 65, no. 5, pp. 1470–1482, 2011.
[34] P. Kellman and E. R. McVeigh, "Image reconstruction in SNR units: A general method for SNR measurement," *Magn. Reson. Med.*, vol. 54, no. 6, pp. 1439–1447, 2005.

4.2 A Signal Acquisition Setup Operating in Parallel on Unmodified Clinical MRI Scanners

This article [13] was published as

Eder, M., Horneff, A., Paul, J., Storm, A., Wunderlich, A., Hell, E., Ulrici, J., Anders, J. and Rasche, V. A signal acquisition setup for ultrashort echo time imaging operating in parallel on unmodified clinical MRI scanners achieving an acquisition delay of 3 µs. *IEEE Transactions on Medical Imaging* 39.: 218–225, 2020

Own contribution:

Design, construction and implementation of the single-loop MR receive coil. Design of the coil's detune circuits. Assistance regarding the performed MR measurements. Editing and reviewing of the manuscript.

A Signal Acquisition Setup for Ultrashort Echo Time Imaging Operating in Parallel on Unmodified Clinical MRI Scanners Achieving an Acquisition Delay of 3 μs

Michael Eder, Andreas Horneff, Jan Paul, Alexander Storm, Arthur Wunderlich, Erich Hell, Johannes Ulrici, Jens Anders, and Volker Rasche

***Abstract*— Ultrashort echo time imaging on clinical systems is still limited by the rather long radio frequency switching times achievable with standard front end concepts. In this contribution, an independent parallel receive-only system is interfaced to an unmodified clinical MRI system, enabling imaging of species with ultrashort relaxation times, such as bone, tendon, teeth, or lung tissue. Synchronization of the system is achieved by an electronically decoupled one-way trigger line, a clock reference signal, and RF pulse tracking, thus ensuring minimal interference with the host system. With the proposed system, an acquisition delay of 3 μs is experimentally demonstrated.**

***Index Terms*— Ultrashort echo time MRI, zero echo time MRI, MR receive chain, MR coil switching, MR data acquisition.**

I. Introduction

WITH continuously improving hardware ultrashort echo time (UTE) [1]–[3] or zero echo time (ZTE) [4], [5] have gained increasing interest as techniques that enable new applications for magnetic resonance imaging (MRI).

One of the key components for these techniques is a radio frequency (RF) front end that can rapidly switch between transmit and receive (T/R) mode, thus enabling data sampling with minimal latency and dead time. The latest generation of MRI systems has improved RF front ends, fast enough to perform ultrashort echo time imaging, if supported by the vendor. In the field however, there are many scanners of earlier generations deployed and even modern systems suffer from limited performance regarding dead time. Due to their generic design, supporting many different coil settings and a large variety of applications, current clinical system face limitations in the achievable switching speed, thereby limiting the minimal acquisition delay from the tens to hundreds of microseconds range on conventional clinical systems. Here, one problem arises from the fact that, to reduce the front end switching time, the entire receive chain has to be considered including the utilized receive coil, which is hardly feasible on a multi-purpose clinical system [6], [7].

As one potential solution to this problem, Weiger *et al.* [4] presented a modified RF front end interfaced to a 7 T whole-body system, yielding dead times below 5 µs. However, in the presented approach the whole front end including RF transmission and reception was replaced by an in-house developed system, thus raising regulatory concerns. Weiger et. al. and other groups further showed the feasibility of algebraic reconstruction for missing data points in the k-space center and the impact of the system dead time on the resulting image quality [8]–[10]. With the presented setup, the feasibility of human ZTE imaging was demonstrated on an unmodified MRI system, without the need for re-sampling k-space center as performed with point wise encoding time reduction with radial acquisition (PETRA) [11], [12] or water- and fat-suppressed proton projection (WASPI) MRI [13], [14].

Further, different fully featured MRI consoles have been introduced [15]–[17], all of them not focused on UTE/ZTE imaging. In contrast, the suggested approach makes use of a conventional clinical MRI system with no hardware modifications required. In this contribution, we propose to interface a vendor independent receive-only system (guest) to a clinical MRI system (host). This approach needs neither additional implementation of RF transmission or gradient control nor the programming of dedicated pre-scan procedures like shimming or RF power calibration, but allowing the optimization of front end switching and hence dead time. The guest is interfaced to the host by an electronically isolated trigger and a clock synchronization line. Modifications on the host system are limited to programming a trigger output signal (as available by the vendor sequence software) for guest/host

Manuscript received March 25, 2019; revised May 16, 2019; accepted June 13, 2019. Date of publication June 20, 2019; date of current version December 27, 2019. This work was supported by the German Research Foundation under Grant RA 1960/9-1. *(Corresponding author: Michael Eder.)*

M. Eder, A. Storm, and V. Rasche are with ExCaVI, University Hospital Ulm, 89081 Ulm, Germany (e-mail: michael.eder@uni-ulm.de; alexander.storm@uni-ulm.de; volker.rasche@uniklinik-ulm.de).

A. Horneff is with University Hospital Ulm, 89081 Ulm, Germany, and also Sirona Dental Systems, 64625 Bensheim, Germany (e-mail: andreas.horneff@dentsplysirona.com).

J. Paul, E. Hell, and J. Ulrici are with Sirona Dental Systems, 64625 Bensheim, Germany (e-mail: jan.paul@dentsplysirona.com; johannes.ulrici@dentsplysirona.com; erich.hell@dentsplysirona.com).

A. Wunderlich is with the Department of Radiology, University Hospital Ulm, 89081 Ulm, Germany (e-mail: arthur.wunderlich@uniklinik-ulm.de).

J. Anders is with the Institute of Smart Sensors, University of Stuttgart, 70569 Stuttgart, Germany (e-mail: jens.anders@ite.uni-stuttgart.de).

Color versions of one or more of the figures in this article are available online at http://ieeexplore.ieee.org.

Digital Object Identifier 10.1109/TMI.2019.2924057

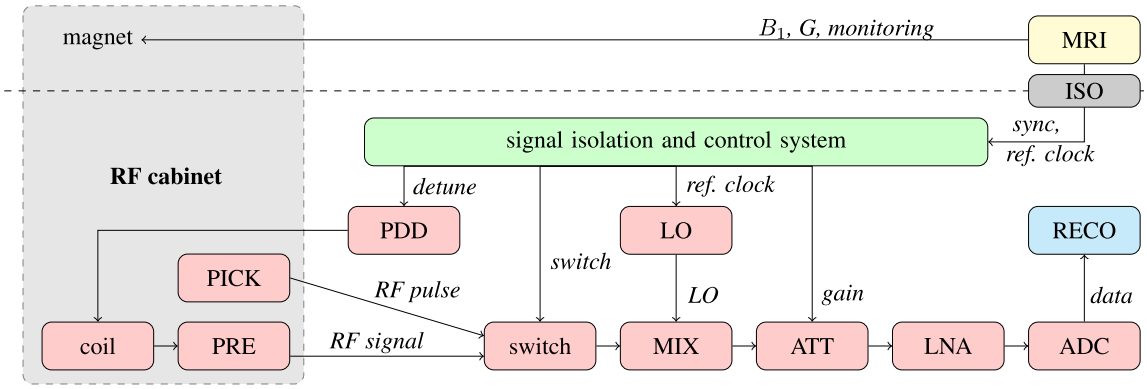

Fig. 1. Total overview of the experiment, which is hosted by a standard clinical MR system (MRI) and is only connected via two removable, isolated lines to the standard interfaces on the host side (ISO). These provide a synchronization trigger signal and a phase synchronous common time base. The systems receive coil is detuned with a PIN-diode-driver (PDD) and the received signal is amplified using a MR rated pre-amplifier (PRE). For pulse tracking a non-tuned pick-up coil (PICK) is used. An RF switch connects either the dedicated receive or the pick-up coil to the analog down conversion module (MIX), which is using the local oscillator frequency (LO). To make use of the full dynamic range of the analog to digital converter (ADC) a configurable attenuator (ATT) is introduced followed by a low noise amplifier (LNA). The digital data is processed with our in-house developed reconstruction framework (RECO).

synchronization, without the requirement for any mechanical or electrical modification of the host system. While this approach can intrinsically not overcome the limitations of procedures performed by the host system, like limited gradient strength or excitation pulse bandwidth and duration, imaging with an acquisition delay of 3 μs was reached.

II. Theory and Methods

Echo time (TE) in a conventional MRI experiment is defined as the time between the magnetic center of the RF pulse and the sampling of the k-space center. The minimal TE is limited by:

- the time of the magnetic center of the RF pulse to its end
- latency $t_{\mathbf{prop}}$, e.g. signal propagation, which can be measured and compensated
- dead time $t_{\mathbf{tune}}$, a transient state of the system where no data can be acquired

Please note that in many UTE publications, in contrast, the echo time is defined as time from the end of the RF pulse to the start of the sampling of the k-space center, which, according to the conventional definition, only comprises the system latency and front end dead time and is considered as acquisition delay $t_{\mathbf{ad}}$ in the following. In this contribution a short acquisition delay $t_{\mathbf{ad}}$ is achieved by minimizing $t_{\mathbf{tune}}$ and compensation of $t_{\mathbf{prop}}$ by respectively shifting the synchronization trigger.

As proof-of-concept, an independent receive-only system was designed and built, operating in parallel to the clinical MRI system. The proposed concept allows for development and testing of the guest without producing any regulatory issues for the host. The guest was interfaced to a Philips Achieva 3 T MRI system (Philips Healthcare, Best, The Netherlands).

The setup is based on standard industrial measurement equipment for handling transistor-transistor logic (TTL) in- and output control signals, data acquisition, data export and system control. Time critical components such as the PIN-diode-driver (PDD) are either custom built or specifically selected to meet the required performance figures.

A schematic overview of the system is provided in Fig. 1. The imaging sequence is executed on the host MR system without any modifications except the additional trigger signal as temporal reference. Pre-scan procedures like pulse power optimization and shimming, and the spin excitation during the scan are performed by the unmodified built-in body coil of the vendor. Signal reception is done by the independent guest receive-only system operating in parallel. Synchronization of the guest system is achieved by the external trigger, generated by the host system, providing a timing reference to the RF excitation pulse, and the local oscillator (LO) clock reference of the host system. Both are guided through the signal isolation and control system and distributed to synchronize and phase lock all guest system components. These are the local oscillator, the analog-to-digital converter (ADC) and the control core clocking.

As Bosshard and Wright [18] and Scott *et al.* [19] noted, phase locking all components does not necessarily result in proper phase tracking, therefore we perform additional sampling of the RF excitation pulse on the same signal processing channel and use its information for phase correction.

The internal hardware control of the guest is implemented in a field programmable gate array (FPGA), ensuring reproducible, rapid and predictable response times. For MR signal reception, a dedicated single element coil with a short ring down time was designed. The receive coil is actively detuned by a coil-optimized PDD. For pulse tracking a non-tuned pick-up coil is used. An RF switch connects either the dedicated receive or the pick-up coil to the following common processing chain. The signal is then down converted by an analog mixer (MIX) to an intermediate frequency. Before sampling, the signal is adjusted to match the optimal input range of the ADC. The ADC is implemented on the FPGA providing a sample rate of 125 MS/s (125 MHz). Analog filters are, wherever possible, replaced by digital post-processing and filtering to further minimize the guest system's latency and dead time. As the dead time of digital filters correlates with the number of samples required until a valid output is reached, this process can be speed up by using high data rates.

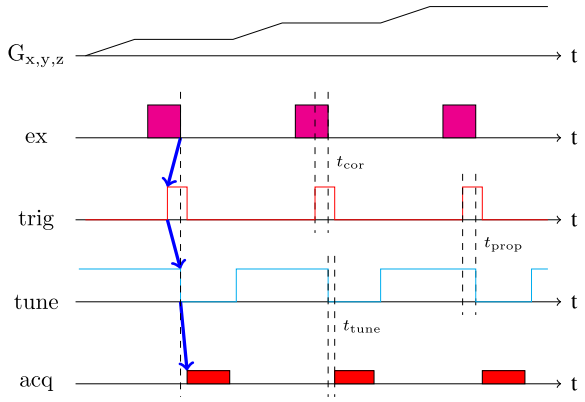

Fig. 2. Based on an exemplary ZTE sequence, the output of the trigger signal from the host sequencer is shifted by t_{cor} to compensate the propagation delay of control signals t_{prop}.

There are two remaining system specific delays that require consideration to acquire with low latency. First, there is the propagation delay t_{prop} introduced by the trigger and control signal processing chain. This delay is not a priori predictable due to component tolerances. Second, the tune delay t_{tune} required for the transition of the coil from detuned to tuned state. As all parameters of the guest system are reproducible and stable over time, both delays can be measured. Where tuning of the coil cannot be started before the end of the excitation pulse, the propagation delay can, at least partially, be compensated by shifting the trigger by a time constant t_{cor}. The acquisition delay is then $t_{ad} = t_{prop} + t_{tune} - t_{cor}$ as shown in Fig. 2. The example is based on a ZTE sequence, but the method is valid in general.

A. Control Logic and Analog-to-Digital Conversion

Instead of building a full featured MR device, meaning the implementation of RF transmit, gradient control, shimming, RF power calibration, to name only some, the guest system comprises an independent signal receive path and digitizer system operating in parallel to the host, thus replacing complex bidirectional synchronization by an one way trigger. The acquisition control and sampling unit is implemented on commercially available PCI eXtensions for Instrumentation (PXIe) components provided by NI (National Instruments, Austin, Texas, USA) equipped with a standard computer interface for programming and data storage.

To connect the PXIe components hosted in the NI-PXIe-1082 chassis, the Multisystem eXtension Interface (MXI) cards NI-PCIe-8381 and NI-PXIe-8381 are used to connect a general purpose input/output (I/O) card (NI-PXIe-6366) and an eight channel high speed digitizer card (NI-PXIe-5171R) with a user programmable FPGA core.

The trigger signal is routed from the host system through the control interface which provides electrical isolation and logic level conversion to the I/O-card of the PXIe-system. To minimize system jitter, the trigger signal is routed to the FPGA core directly in hardware via the chassis backplane. The same backplane is used to distribute the 10 MHz time base reference and phase lock all PXIe modules. The trigger starts the FPGA generation of the control signals. All derived control signals are routed through the signal isolation interface to the respective control inputs of the guest front end.

The data acquisition is triggered via the NI-PXIe-1082 internal backplane by a control signal generated by the FPGA (guest) based on the synchronization trigger (host), thus ensuring a data sampling completely independent of the host. Using NI's binary technical data management streaming (TDMS) data format, with the current configuration, the conversion unit is capable of continuously sampling and streaming with at least 250MB/s, only limited by the memory of the control computer.

The programming and execution of the data acquisition process is done with LabVIEW (17.0.1f73 32-bit and 64-bit). Further data processing is done using MATLAB (Mathworks Inc., Natick, Massachusetts, USA).

B. Control Signal Interface

A major requirement for avoiding safety hazards from or damages to the guest system is to ensure a well-defined state in case of total system or component failure. Therefore, a common interface for signal routing and electrical isolation is used, ensuring electrical safety of the guest system as well as reducing noise coupling from control logic components and cables into the RF processing chain. This configuration also provides straightforwardly access for debugging or bypassing the common interface if necessary. The interface provides the required control lines, isolation modules, power level converters and other special functions. The power supply units (PSU) are filtered (both directions to minimize background noise and RF coupling) and monitored on a dedicated printed circuit board (PCB). The central power distribution minimizes the number of required PSUs, thus minimizing power line length and related noise. The required supply sources are derived from 24 V, 10 V, 7.5 V and −15 V. Long power cables are additionally buffered by dedicated high value capacitors. The logic control signals are isolated using ADUM1200AR isolation barriers (Analog Devices, Norwood, Massachusetts, USA) and are buffered by SN74LVCC4245ADW bus drivers (Texas Instruments, Dallas, Texas, USA) on the internal signal backplane to ensure well defined signal states and to translate logic voltages as required. Especially the isolation devices are known to have a substantial propagation and chip-to-chip delay, however these are specific for each single component and stable over time and can therefore be easily compensated.

To further avoid any safety concerns, the input trigger signal is internally converted to a physical controller area network (CAN) layer to allow multiple simultaneous access of modules with override function. Only if all interfaces are in "run mode" the trigger signal can be transmitted. By design, this circuits will fall to a safe state if not all "run" conditions are met.

C. MR Receive Coil

A hexagonal shaped single-loop coil (Fig. 3) with a side length of 40 mm was built in conventional PCB technology using FR4 with a thickness of 60 µm as substrate. The copper loop track is 6 mm wide and has a thickness of 35 µm.

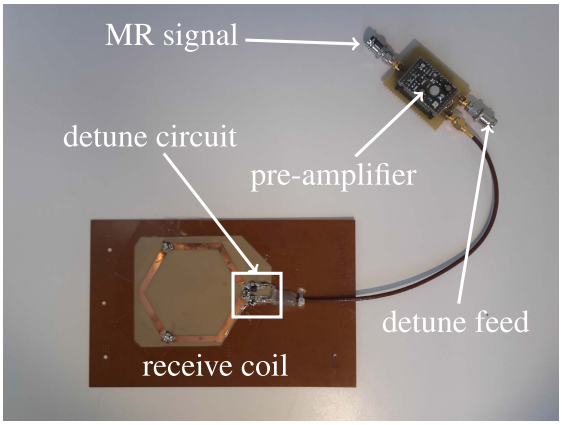

Fig. 3. Single-loop receive-only coil used for switching time optimization and subsequent imaging experiments. Attached is an MR compatible in-field LNA as signal pre-amplifier (Siemens Healthcare, Erlangen, Germany). The carrier PCB of the LNA includes a bias tee to feed the PIN-diode based detune circuit integrated in the coil.

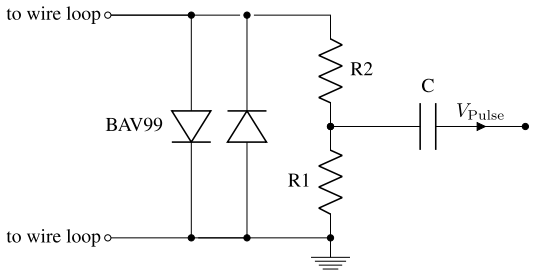

Fig. 4. Anti-parallel diodes (BAV99, NXP, Eindhoven, Netherlands) and a voltage divider are used to clamp the output of the non-tuned pick-up coil to safe values. The capacitor is used as DC block.

For detuning, two PIN-diode-driven (MADP-000235-10720T, MACOM, Lowell, USA) circuits are used to decouple the coil during excitation. The circuit is driven in series by an RF blocking inductor and fed externally by a dedicated line. The MR signal is direct current (DC) blocked and routed to an MR compatible low noise amplifier (LNA) (Siemens Healthcare, Erlangen, Germany) tuned to 127.7 MHz for proton imaging at 3 T. For more details of the MR receive coil, please refer to Horneff *et al.* [20].

D. Pulse Pick-up Coil

A quadratic copper wire loop with a side length of 5 mm is used as pick-up coil for excitation pulse tracking. To protect the following RF chain from voltage surges the output is clamped using anti-parallel diodes (BAV99, NXP, Eindhoven, Netherlands) and a voltage divider. The schematic is show in Fig. 4. A capacitor is added as DC block. No name products are used for resistors and the coupling capacitor.

E. PIN-Diode-Driver (PDD)

In the literature, different detune mechanisms aiming for rapid switching of the coil front end have been proposed. However, all approaches are relatively complex, to simultaneously achieve the demanding design goals of a high signal to noise ratio (SNR), a high linearity and a high isolation between transmit and receive mode [21], [22]. In general, there are

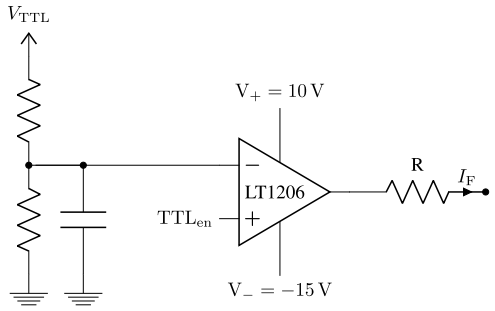

Fig. 5. The PIN-diode-driver driver uses an LT1206 operational amplifier (Linear Technology, Milpitas, California) as current source. The enable signal is provided as TTL line and compared to half of the logic supply voltage. The detune current is adjusted using a resistor as limiter.

three parameters that can be used to improve the timing behavior of the detune circuit: the diode forward current, its reverse voltage and the PIN-diode parameters [23], [24].

In imaging of ultrashort T_2^* components the critical part is the switching time from detuned to tuned state, which should be done with minimal dead time to avoid MR signal loss and thus enabling ZTE imaging. While this is, aside from signal decay, less critical for UTE it is vital for ZTE applications. Most approaches, on conventional T/R coil systems aim for high bias currents to ensure linear signal transmission and low power loss in the PIN-diode. In case of receive-only coils however, this is not necessarily advantageous for optimizing the detuned to tuned switching time. Due to the reduced RF power in a receive-only system, lower PIN-diode bias currents can be used for driving the detune circuit.

The switching time from detuned (conducting) to tuned (blocking) state is defined by [23], [24]:

$$T_{\mathrm{FR}} = \ln\left(1 + \frac{I_{\mathrm{F}}}{I_{\mathrm{R}}}\right)\tau, \tag{1}$$

with I_{F} being the forward current, I_{R} the reverse current and τ the minority carrier life time. As τ is an intrinsic property of the PIN-diode, the ratio of $I_{\mathrm{F}}/I_{\mathrm{R}}$ can be used to reduce T_{FR}.

Since the aim of the suggested method is not to provide an universal methodology for the design of receive-only PDDs, an empirical, iterative approach based on (1) for optimizing the PDD response time of the coil configuration described in section II-C was employed. A standard operational amplifier LT1206 (Linear Technology, Milpitas, California) was used as current source driving the PIN-diodes. The corresponding schematic is shown in Fig. 5.

The efficiency of the detuned state of the low I_{F} PDD was tested by analyzing the local signal (flip angle) enhancement in the vicinity of the self-built coil. This is based on the effect, that any tuned coil would enhance the local B_1 field.

MR images were acquired with the body coil used for both transmission and reception for different static values of I_{F}. For analysis a conventional gradient echo sequence was used. The intensity ratio of two region of interest (ROI) per experiment, within the same object, was evaluated. One ROI was placed in the vicinity of the self-built coil and the other in safe distance. The ratio was normalized with a reference value, acquired in the same object and ROIs, but without the self-built receive coil. The minimal diode current $I_{\mathrm{F,min}}$ required for

avoiding any local signal enhancement was identified and a fixed current including a safety margin was used for all subsequently performed experiments.

As input a TTL signal is directly used and compared to a reference of a voltage divider fed by the logic supply voltage V_{TTL} to make it universal. The LT1206 operational amplifier can provide a maximum output current of 250 mA at a frequency of 60 MHz. The current driving the PIN-diodes is limited by the resistor R. The driver circuit is powered with $V_+ = 10\,\mathrm{V}$ and $V_- = -15\,\mathrm{V}$. A value of $R = 390\,\Omega$ is used, resulting in an effective detune current of $I_F = 23\,\mathrm{mA}$. In the tuned state, the PIN-diodes are biased with the full negative supply voltage.

F. MR Signal, RF Pulse Signal and RF Processing

The 50 Ω matched receive coil is connected to a detune bias tee between the coil and an MR compatible pre-amplifier to feed the detune circuit. Two standard MR compatible RG-58 cables (supplied by Philips, Best, Netherlands) are used to guide the signal to the control room and to feed the detune current. A second bias tee is used to apply the 10 V power supply for the pre-amp to the signal cable. For phase tracking a non-tuned pick-up coil is used and the signal is guided to the control room also using a standard MR compatible RG-58 cable. The output of the pick-up coil is clamped in the control room to prevent voltage or signal surges to be passed to the following signal processing chain. A single pole double throw (SPDT) switch of the type ZYSWA-1-50DR (Mini-Circuits, Brooklyn, New York, USA) is used for coil selection. A TTL reference routes either the MR signal or, by default, the RF pulse signal forwards to the analog mixer. The used RF mixer was provided by RS2D (Mundolsheim, France) and the IF (intermediate frequency) was selected to be 20 MHz.

The required LO frequency is provided by the programmable synthesizer VALON 5009 (Valon Technology, Redwood City, California, USA). To make use of the full dynamic range of the ADC, a ZX-60-33LN+ low noise amplifier (Mini-Circuits, Brooklyn, New York, USA) is inserted before feeding the signal to the digitizer card. Optionally, a ZX76-31R5-PP+ digital step attenuator (Mini-Circuits, Brooklyn, New York, USA) can be connected between the amplifier and the ADC, for further signal conditioning.

The signal chain beyond the RF cage is based on broadband components that are selected to operate from 40 − 500 MHz, but have only been tested at 127.7 MHz (Philips Achieva 3 T) and 123.3 MHz (Siemens Skyra 3 T). The supply voltages for the different modules are generated with linear regulator circuits followed by buffers close to the RF modules.

G. Digital Data Processing and Image Reconstruction

As mentioned in section II-F the analog signal is mixed to an intermediate frequency of 20 MHz. The signal is sampled at 125 MS/s (125 MHz) and transferred as a single, continuous binary data stream during the full length of the experiment. In the digital domain, the following data processing steps are performed to extract the k-space data.

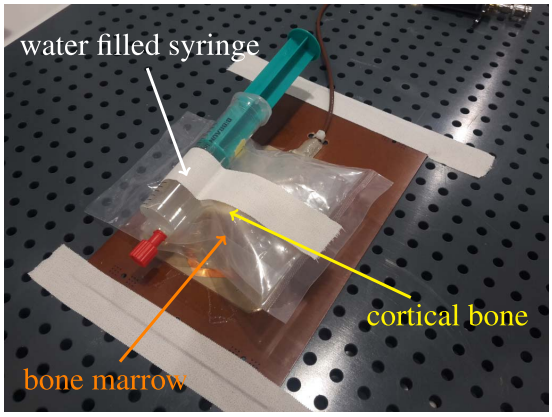

Fig. 6. Phantom setup for testing of the proposed receive-only system. A sealed piece of human femur long bone was used for imaging, providing long T_1 and T_2^* components in the bone marrow and short T_2^* components in the cortical bone. A water filled syringe was added to provide additional signal. The phantom was placed in the center of the single-loop receive-only coil shown in Fig. 3.

1) The single, continuous, binary data stream is split into individual data sets representing the spokes.
2) Each data spoke is further split into a pre-sample containing RF pulse data and the data segment representing the actual MR signal.
3) The time domain data, of the RF pulse and the MR signal, are Fourier transformed and the spectrum of 20 MHz ± 500 kHz is selected and transformed back to the time domain. This operation also converts the real ADC data into complex data and performs data reduction.
4) Phase information is calculated from the RF pulse data and applied on the MR signal data for phase correction.
5) Data are then reconstructed using a gridding method.

We used this, as a straightforward approach to perform higher order filter operations allowing for the required selectivity in the filter. However more sophisticated data analysis can be performed e.g. the method suggested by Marjanovic *et al.* [25].

H. Imaging Setup

The receive-only system was tested on the simple phantom as shown in Fig. 6. As imaging object a sealed piece of human femur long bone was used. The ethical approval is registered under number 300/12 and the specimen was anonymized for our use. A water filled syringe was attached to the phantom, placed in the center of the receive-only coil and carefully positioned in the iso-center of the magnet. This phantom was chosen because the syringe and bone marrow provide enough signal with long T_1 and T_2^* components, to be used for shimming, center frequency and pulse power determination, while the cortical bone adds some ultrashort T_2^* components.

Imaging experiments include a 3D UTE and a 3D ZTE sequence. During implementation of the sequences, the timing of the gradients was adapted to fit the timing, made possible by the proposed receive-only system, hence going beyond the capabilities of the vendor's front end.

Data were acquired with a field of view FOV = 100 mm^3, flip angle $\alpha = 4°$, length of excitation block pulse

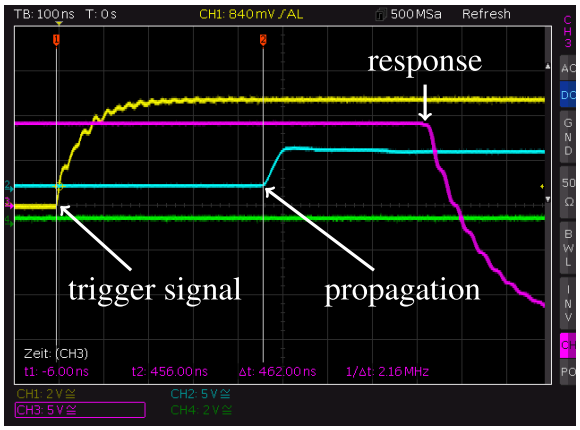

Fig. 7. Minimal response timing diagram for the control logic of the proposed system configuration. The reference trigger signal (yellow) is provided by the host MR sequencer. It takes a propagation delay of about ≈ 450 ns to pass all signal isolation modules to the FPGA (blue). The minimal response time of the FPGA logic is ≈ 350 ns, as indicated by the output voltage of the unloaded PIN-diode-driver (red). This results in a total response time t_{prop} of minimal ≈ 800 ns.

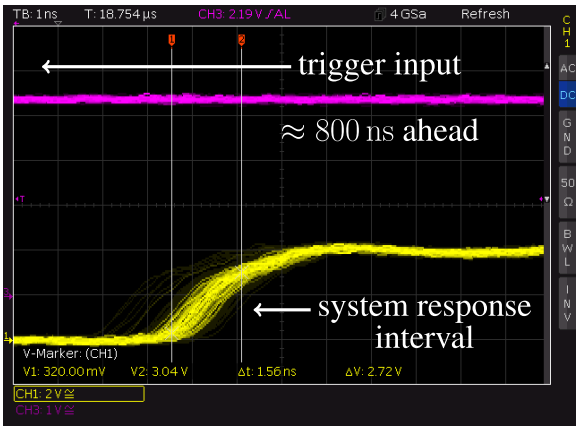

Fig. 8. Jitter measurement of the full digital trigger processing chain. The TTL input signal (red) is used as reference and can not be appreciated in this plot. The system response output (yellow) shows a jitter interval of less than 1.5 ns. Please note, that some jitter may be introduced by imperfect triggering of the oscilloscope itself, due to its limited time resolution.

$T_{\text{RF}} = 25.6\,\mu\text{s}$ ($T_{\text{RF}} = 32\,\mu\text{s}$ including ramp up and down in $3.2\,\mu\text{s}$), excitation field amplitude $B_{1,\text{max}} = 13.5\,\mu\text{T}$ and an isotropic spatial resolution of $\Delta r = 1\,\text{mm}^3$ in 79996 equi-spaced center-out spokes. The pixel bandwidth was set to PBW = 1315.4 Hz ($T_{\text{read}} = 486.1\,\mu\text{s}$, $G_{\text{read}} \approx 30\,\text{mT/m}$) for UTE and PBW = 434.1 Hz ($T_{\text{read}} = 1.3$ ms, $G_{\text{read}} \approx 10\,\text{mT/m}$) for ZTE. The repetition rate was set to TR = 4.1 ms. Anticipating the possible system response time, an acquisition delay of $t_{\text{ad}} = 3\,\mu\text{s}$ was applied. Considering the half of the excitation pulse length of 16 µs and the bandwidth for ZTE, this results in a loss of less than two Nyquist dwells, which can be compensated using an algebraic reconstruction [8], [9]. Due to the limited gradient field strength for ZTE, which is a trade of for the rather long pulse excitation, no additional acquisitions were required to measure the missing k-space center data. This constriction does not apply for UTE and the full gradient strength was applied for imaging. Reconstruction of the data was performed with an in-house developed reconstruction framework implemented in MATLAB.

III. Results

First the timing behavior of the guest system was investigated to validate its design parameters and its stable operation.

The plot in Fig. 7 shows the minimal response timing diagram for the control logic of the proposed system configuration. The reference trigger signal (yellow) is provided by the host MR sequencer. It takes a propagation delay of about 450 ns to pass all signal isolation modules to the FPGA (blue). The minimal response time of the FPGA logic of about 350 ns is indicated by the output voltage of the unloaded PIN-diode-driver (red), resulting in a total minimum response time of $t_{\text{prop}} \approx 800$ ns for the control outputs. This delay can easily be compensated by shifting the reference trigger generated by the host sequencer.

The jitter of the full digital trigger processing chain, hence the start of the signal sampling, from the TTL input to the control output, including all signal conditioning devices and digital processing steps, was measured and is plotted in Fig. 8. The TTL input trigger signal (red) is used as reference and can not be appreciated in this plot. The system response output (yellow) shows a jitter interval of less than 1.5 ns. This translates to a phase error of less than 3 % at an intermediate frequency of 20 MHz. Please note, that this measurement takes place close to the maximal sampling resolution of 250 ps of our measurement equipment. Some of the seen jitter may therefore be introduced by imperfect triggering of the oscilloscope itself.

An exemplary timing diagram of the receive-only system RF data processing is provided in Fig. 9. For this measurement a free induction decay (FID) with a flip angle of $\alpha = 25\,^\circ$ was acquired. After being started by the trigger reference from the host MR sequencer, the control logic takes over and provides all signals to activate the receive front end. The host signals the end of the RF pulse $100\,\mu\text{s}$ ahead so it is adjusted to the time point $0\,\mu\text{s}$. Immediately after the trigger input, the guest starts to acquire data received from the pick-up coil, as can be seen in the red RF pre-sampling section. The acquisition delay (black) of the system consists of three compartments. A safety wait of $1\,\mu\text{s}$ is performed before the dedicated coil is set to receive mode. After another delay of $1\,\mu\text{s}$ the signal path is switched from the pick-up to the receive coil. Again a generous $1\,\mu\text{s}$ wait is introduced for the RF switch to settle. A valid MR signal (blue) can be assumed after a total acquisition delay of $t_{\text{ad}} = 3\,\mu\text{s}$.

The minimal required detune current was evaluated as described in section II-E. Example images are shown in Fig. 10. Results are shown in Table I. The normalized image intensity ratio $\|I\|$ should be close to 1 to indicate sufficient detune capability. For I_{F} as low as 6 mA the detune is performing in the expected range, therefore choosing $I_{\text{F}} = 23$ mA was assumed to be a good compromise between a low tune delay and a sufficient buffer for operating with unforeseen high power excitation pulses.

Fig. 11a shows an UTE reference image acquired using the body coil of the host system in parallel, while also acquiring

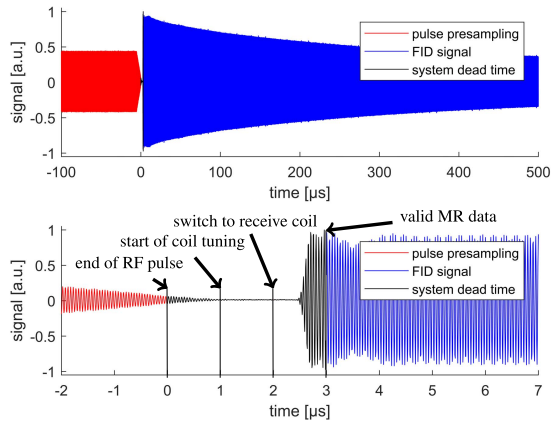

Fig. 9. Exemplary timing diagram of the RF processing chain while acquiring an FID with a flip angle $\alpha = 25°$. The host signals the RF pulse 100 μs ahead, so its end is adjusted to $t = 0\,\mu$s. Immediately after the trigger input, the guest starts to acquire data received from the pick-up coil, as can be seen in the red RF pre-sampling section. The control logic waits 1 μs, performs tuning and switches from the pick-up to the dedicated receive coil after 2 μs. A valid MR signal (blue) can be assumed after a total acquisition delay (black) of $t_{ad} = 3\,\mu$s.

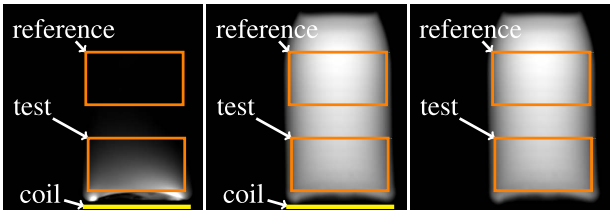

Fig. 10. The images were acquired, using the body coil of the scanner, with a gradient echo sequence. They show identical slices and ROIs to measure local signal (flip angle) enhancement, caused by a tuned receive coil in the vicinity. In Fig. (a) the self-built receive coil is tuned, while in Fig. (b) the same coil is detuned, using a static current of $I_F = 25$ mA. Fig. (c) shows the reference image, acquired without the self-built coil inside the scanner.

TABLE I
RESULTS OF NORMALIZED FLIP ANGLE ENHANCEMENT MEASUREMENT

I_F [mA]	0	6	12	25	50	75	125	200
$\|I\|$	0.17	1.02	1.02	1.01	1.01	1.02	1.01	1.02

data with the PXI system. The corresponding image reconstructed from PXI data is shown in Fig. 11b. An acquisition delay of $t_{ad} = 122\,\mu$s was applied. One can appreciate the intensity profile of the dedicated receive coil coupling into the image received by the host. In the Fig. 11c, Fig. 11d and Fig. 11e the acquisition delay was step wise reduced to the minimum of $t_{ad} = 3\,\mu$s. A clear signal enhancement can be appreciated in the short T_2^* species of the cortical bone for lower t_{ad}.

In Fig. 11f, the ZTE image acquired with the proposed hardware is shown. After setting the next gradient step, a delay of 1 ms was introduced to wait for the gradient system to settle, before applying the RF pulse. Data were acquired with an acquisition delay of $t_{ad} = 3\,\mu$s after the end of the RF pulse. The blurring of short T_2^* species, compared to UTE, is caused by the rather long read out duration due to the gradient limitation given by the RF pulse. Also this setting is deteriorating chemical shift artifacts which causes additional

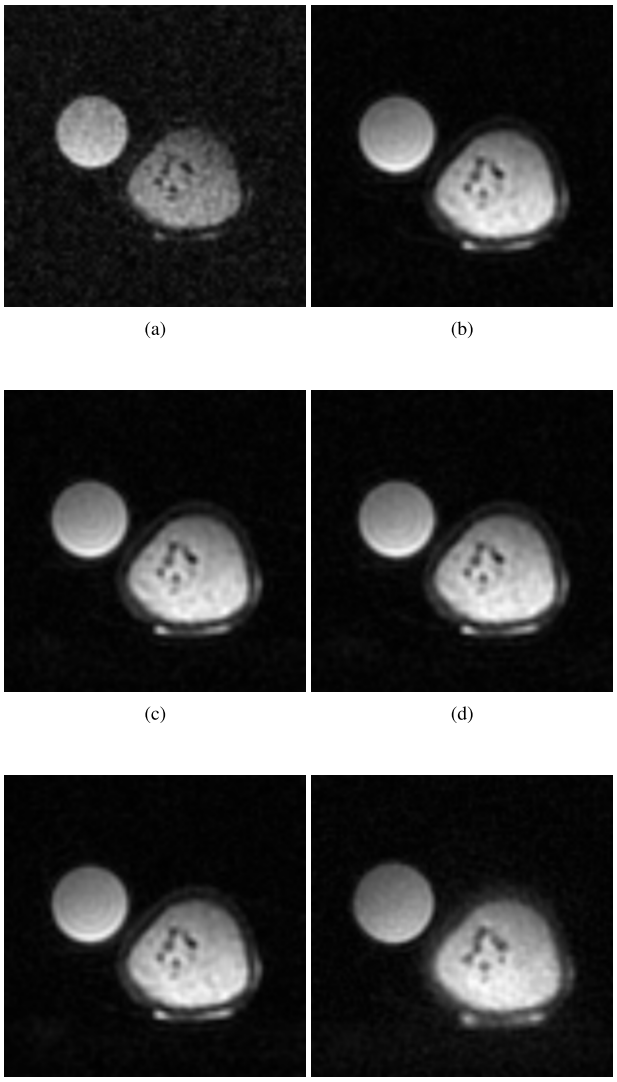

Fig. 11. Fig. (a) shows an UTE reference image acquired using the body coil of the host system in parallel, while also acquiring data with the PXI system. One can appreciated the intensity profile of the dedicated receive coil coupling into the image received by the host. The Images in Fig. (b) to (f) show identical transverse slices acquired using the configuration shown in Fig. 6. For UTE the acquisition delay was step wise reduced to from the hosts limit of $t_{ad} = 122\,\mu$s (Fig. (b)) the proposed system limit of $t_{ad} = 3\,\mu$s (Fig. (e)) A clear signal enhancement can be appreciated in the short T_2^* species of the cortical bone for lower t_{ad}. In Fig. (f) a ZTE image is shown. The blurring of short T_2^* species, compared to UTE, is caused by the long read out duration due to the gradient limitation given by the RF pulse.

blurring in the bone marrow. This is a sole limitation of the hosts RF transmission system, which the guest can intrinsically not overcome. This was required to demonstrate the feasibility to run ZTE, without the need of additional measurements to cover missed data points in the k-space center, on a standard clinical MR scanner.

IV. DISCUSSION

In this work, the feasibility to perform UTE and ZTE imaging on a standard and unmodified clinical MRI system has been shown. The implementation is robust including

fail-safety measures and the design provides an open and easy to access platform for future improvements and upgrades. The proposed approach is limited by the performance of the host system, regarding RF excitation and gradient strength. The performance of the receive chain is distinctly enhanced. In contrast to more complex transmit and receive systems, an improvement of the timing could be shown, without any modification of the hosts hardware.

The proposed system and components can provide a very short acquisition delay of 3 μs. This delay includes additional safety margins. We introduced an 1 μs pause between the end of the pulse and the start of the detune process. Also the required dead time of 800 ns for tuning was extended to 2 μs. All system control propagation delays were fully compensated.

Regarding UTE, the demonstrated ultra short echo times with acquisition delays down to $t_{ad} = 3\ \mu$s may not be required for clinical applications operating at 3 T or below, however material imaging or operating at high field system of 7 T and above may benefit due to the shortened T_2^*.

Although the guest system is capable to perform fast switching between transmit and receive in 3 μs, ZTE imaging suffers from the long excitation pulse duration and therefore possible loss of k-space center information. As mentioned this is a sole issue of the hosts RF transmission system and required us to limit the gradient strength for imaging. The long readout duration causes blurring of the short T_2^* components and deteriorates chemical shift artifacts. This constriction does not apply for UTE and the full gradient strength was applied for imaging there.

The open architecture enables further investigations of the PIN-diode-driver circuit and provides an easy-to-interface general coil front end for dedicated receive only coils.

V. Conclusion

The proposed approach is capable of interfacing an independent receive-only system to a standard and unmodified clinical MR scanner, thus enabling sampling of the MRI signal independent of the host system. The focus of the presented work was on sampling data with minimal latency and dead time after the excitation pulse, thereby improving the performance of the system for ultrashort and zero echo time imaging. Additional applications are advanced filter design, by supplying large amounts of raw data, or rapid testing of dedicated coils. The coils, or even multi channel arrays, can be tested without adapting to the often complex coil interfaces of the vendors, while keeping the full flexibility and variety of MR sequences available on the respective clinical MR system.

Acknowledgment

The authors thank the Centre for Trauma Research at the Ulm University Hospital for providing the imaging specimen. They thank the Ulm University Center for Translational Imaging MoMAN for its support.

References

[1] M. D. Robson, P. D. Gatehouse, M. Bydder, and G. M. Bydder, "Magnetic resonance: An introduction to ultrashort TE (UTE) imaging," *J. Comput. Assist. Tomogr.*, vol. 27, no. 6, pp. 825–846, Nov./Dec. 2003. [Online]. Available: https://journals.lww.com/jcat/toc/2003/11000

[2] A.-K. Bracher *et al.*, "Feasibility of ultra-short echo time (UTE) magnetic resonance imaging for identification of carious lesions," *Magn. Reson. Med.*, vol. 66, no. 2, pp. 538–545, Aug. 2011. doi: 10.1002/mrm.22828.

[3] J. H. Brittain *et al.*, "Ultra-short TE imaging with single-digit (8 μs) TE," in *Proc. Int. Soc. for Magn. Reson. Med.*, vol. 11, 2004, p. 629.

[4] M. Weiger, D. O. Brunner, B. E. Dietrich, C. F. Müller, and K. P. Pruessmann, "ZTE Imaging in Humans," *Magn. Reson. Med.*, vol. 70, no. 2, pp. 328–332, Aug. 2013. doi: 10.1002/mrm.24816.

[5] M. Weiger *et al.*, "High-resolution ZTE imaging of human teeth," *NMR Biomed.*, vol. 25, no. 10, pp. 1144–1151, Oct. 2011. doi: 10.1002/nbm.2783.

[6] D. P. Madio and I. J. Lowe, "Ultra-fast imaging using low flip angles and fids," *Magn. Reson. Med.*, vol. 34, no. 4, pp. 525–529, Oct. 1995. doi: 10.1002/mrm.1910340407.

[7] S. Hafner, "Fast imaging in liquids and solids with the Back-Projection Low Angle ShoT (BLAST) technique," *Magn. Reson. Imag.*, vol. 12, no. 7, pp. 1047–1051, 1994. doi: 10.1016/0730-725X(94)91236-P.

[8] M. Weiger, D. O. Brunner, M. Tabbert, M. Pavan, T. Schmid, and K. P. Pruessmann, "Exploring the bandwidth limits of ZTE imaging: Spatial response, out-of-band signals, and noise propagation," *Magn. Reson. Med.*, vol. 74, no. 5, pp. 1236–1247, Nov. 2015. doi: 10.1002/mrm.25509.

[9] R. Froidevaux, M. Weiger, D. O. Brunner, B. E. Dietrich, B. J. Wilm, and K. P. Pruessmann, "Filling the dead-time gap in zero echo time MRI: Principles compared," *Magn. Reson. Med.*, vol. 79, no. 4, pp. 2036–2045, Apr. 2018. doi: 10.1002/mrm.26875.

[10] D. O. Kuethe, A. Caprihan, I. J. Lowe, D. P. Madio, and H. Gach, "Transforming NMR data despite missing points," *J. Magn. Reson.*, vol. 139, no. 1, pp. 18–25, Jul. 1999. doi: 10.1006/jmre.1999.1767.

[11] D. M. Grodzki, P. M. Jakob, and B. Heismann, "Ultrashort echo time imaging using pointwise encoding time reduction with radial acquisition (PETRA)," *Magn. Reson. Med.*, vol. 67, no. 2, pp. 510–518, Feb. 2012. doi: 10.1002/mrm.23017.

[12] G. Dournes *et al.*, "Quiet submillimeter mr imaging of the lung is feasible with a PETRA sequence at 1.5 T," *Radiology*, vol. 276, no. 1, pp. 258–265, Mar. 2015. doi: 10.1148/radiol.15141655.

[13] Y. Wu *et al.*, "Water- and fat-suppressed proton projection MRI (WASPI) of rat femur bone," *Magn. Reson. Med.*, vol. 57, no. 3, pp. 554–567, Mar. 2007. doi: 10.1002/mrm.21174.

[14] Y. Wu *et al.*, "Bone mineral imaged in vivo by ^{31}P solid state MRI of human wrists," *J. Magn. Reson. Imag.*, vol. 34, no. 3, pp. 623–633, Sep. 2011. doi: 10.1002/jmri.22637.

[15] P. P. Stang, S. M. Conolly, J. M. Santos, J. M. Pauly, and G. C. Scott, "Medusa: A scalable MR console using USB," *IEEE Trans. Med. Imag.*, vol. 31, no. 2, pp. 370–379, Feb. 2012. doi: 10.1109/TMI.2011.2169681.

[16] C. J. Hasselwander, Z. Cao, and W. A. Grissom, "GR-MRI: A software package for magnetic resonance imaging using software defined radios," *J. Magn. Reson.*, vol. 270, pp. 47–55, Sep. 2016. doi: 10.1016/j.jmr.2016.06.023.

[17] M. Tsuda, D. Tamada, Y. Terada, and K. Kose, "Development of digital MRI consoles using general-purpose digital instruments and microcontroller boards," *Appl. Magn. Reson.*, vol. 47, no. 8, pp. 847–858, Aug. 2016. doi: 10.1007/s00723-016-0806-4.

[18] J. Bosshard and S. Wright, "Phase correction with asynchronous digitizers," in *Proc. Int. Soc. Magn. Reson. Med.*, no. 1787, 2015.

[19] G. Scott, F. Robb, J. Pauly, and P. Stang, "Software synchronization of independent receivers by transmit phase tracking," in *Proc. Int. Soc. Magn. Reson. Med.*, no. 4311, Apr. 2017.

[20] A. Horneff *et al.*, "An EM simulation-based design flow for custom-built MR coils incorporating signal and noise," *IEEE Trans. Med. Imag.*, vol. 37, no. 2, pp. 527–535, Feb. 2017. [Online]. Available: https://ieeexplore.ieee.org/document/8070983

[21] M. Twieg, M. A. de Rooij, and M. A. Griswold, "Active detuning of MRI receive coils with GaN FETs," *IEEE Trans. Microw. Theory Techn.*, vol. 63, no. 12, pp. 4169–4177, Dec. 2015. [Online]. Available: https://ieeexplore.ieee.org/document/7328341

[22] D. O. Brunner *et al.*, "Symmetrically biased T/R switches for NMR and MRI with microsecond dead time," *J. Magn. Reson.*, vol. 263, pp. 147–155, Feb. 2016. doi: 10.1016/j.jmr.2015.12.016.

[23] *Design With PIN Diodes*, Skyworks, Woburn, MA, USA, 2010.

[24] W. E. Doherty, Jr., and R. D. Joos, *The PIN Diode Circuit Designers Handbook*. Aliso Viejo, CA, USA: Microsemi, 1998.

[25] J. Marjanovic *et al.*, "Multi-rate acquisition for dead time reduction in magnetic resonance receivers: Application to imaging with zero echo time," *IEEE Trans. Med. Imag.*, vol. 37, no. 2, pp. 408–416, Feb. 2018. [Online]. Available: https://ieeexplore.ieee.org/document/8030133

4.3 Extended studies – An Electronically Tunable X-nuclei Surface Coil

4.3.1 Introduction

In this chapter, a new approach based on a fast electronically switchable surface coil design in combination with a custom designed broadband high impedance preamplifier is introduced. The frequency range of the proposed setup covers frequencies between 34 MHz and 104 MHz, thereby greatly simplifying the overall receive chain hardware complexity. The operating frequency of the test setup can be adjusted by commercially available, digitally tunable capacitor arrays providing a 1024-step resolution for the respective frequency range. The basic idea of using digitally controlled capacitor arrays has been previously introduced in the literature, e.g. by W.J. Turner et al. in[45]. This approach is extended by a broadband, high-input impedance LNA yielding a broadband MRI/MRS system with greatly simplified complexity compared to the state-of-the-art. The switching time between different frequencies of the proposed setup results around 60 µs. High-impedance LNA preamplifier decoupling for the tuned and non-matched coil configuration is shown.

A feasibility study showing the applicability of the suggested approach for ^{1}H imaging ($CuSO_4$ phantom at 1.43 T and 1 T) and ^{19}F imaging ($C_{15}F_{30}O_5$ phantom at 1.43 T) has been performed and compared against a conventional, state-of-the-art single-frequency receive chain, including coil sensitivity and receive chain SNR.

4.3.2 Theory and Methods

The conventional receive chain setup consists of a Rx-only coil[22, 18, 51, 25] and a conventional, off-the-shelf MRI LNA (Ref-LNA), consisting of passive matching networks and a active device, yielding four frequency selective circuits, as illustrated in Fig. 17.

1. The tuning capacitors (C_{t1}, C_{t2}), which tune the resonance frequency of the LC resonator formed by the coil and the tuning capacitors to the Larmor frequency.

2. The matching capacitors (C_{m1}, C_{m2}), which transform the impedance of the LC resonant circuit formed by the coil and the tuning capacitors to the desired value, for a single-coil Rx-chain typically $50\,\Omega$.

3. The input noise matching of the Ref-LNA, which matches the input impedance of the active element to the required impedance, here, for a single coil readout $50\,\Omega$.

4. The output gain matching network, transforming the output impedance Z_{out} to an impedance of $50\,\Omega$, which is required for a reflection-free transmission via a conventional $50\,\Omega$ transmission line.

Due to the frequency selective nature of the utilized matching networks, the reference setup is in the following referred to as the "narrowband LNA". The disadvantage of the architecture shown in Fig. 17a results from its inability to switched between different resonance frequencies. To enable multi nuclei detection, multi resonant probes[29] have to be combined with multiple LNAs[46].
As an alternative solution, a modified receive chain architecture is depicted in Fig. 17b, which displays several advantages compared to the conventional approach. In particular, the use of a custom designed broadband, high-impedance LNA (CMOS-LNA) enables time-multiplexed sampling at different resonant frequencies by adjusting the electronically tunable capacitors (c.f. chapter 2.2 – *Special aspects of X-nuclei imaging*).

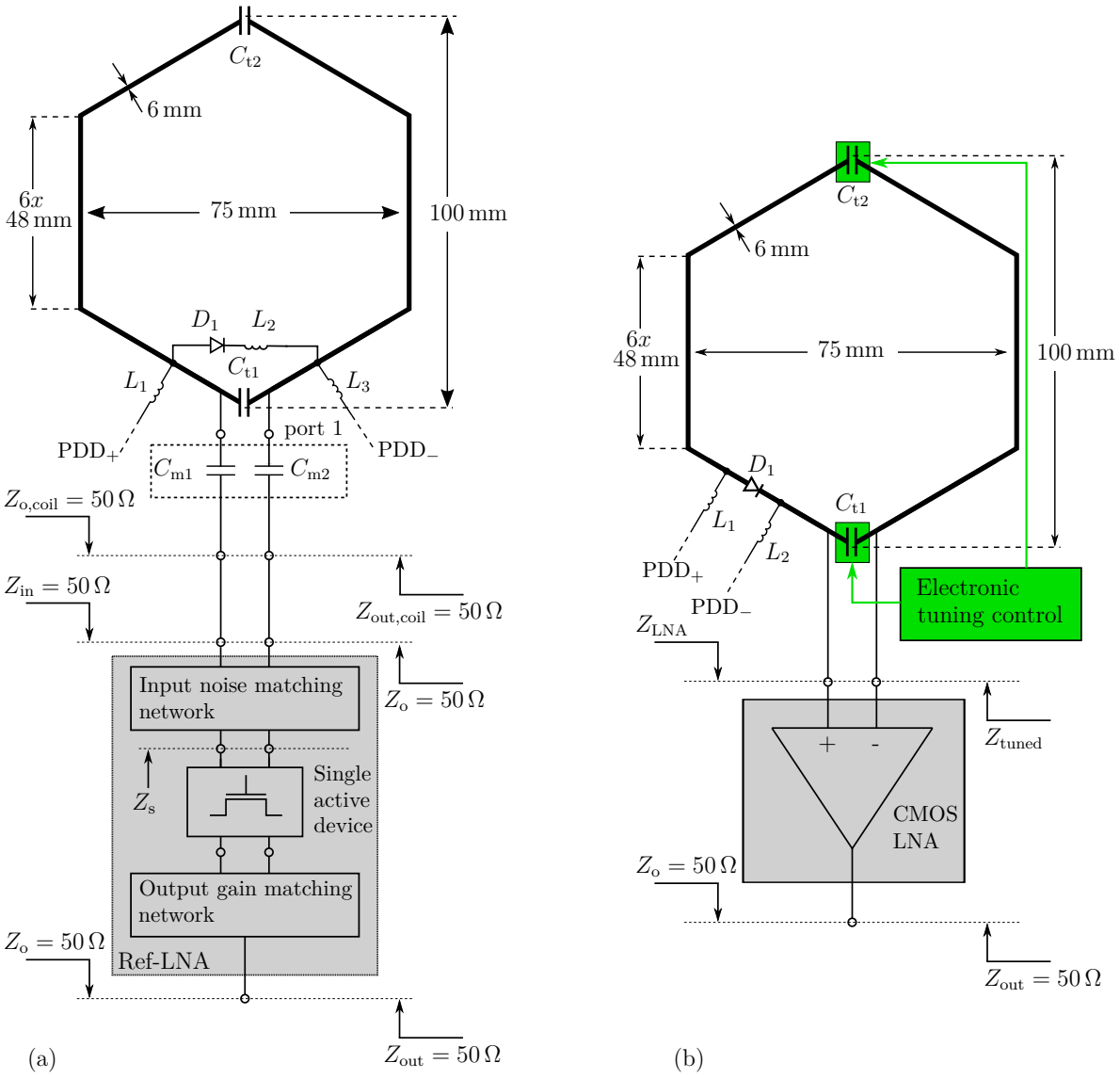

Figure 17: (a) Schematic illustration of the reference receive chain setup; the Rx-coil's configuration according to [22, 18, 51, 25], its dimensions and the conventional MRI preamplifier architecture according to [10]. (b) Architecture of the proposed receive chain setup, including the Rx-coil's geometry and configuration.

Impedance matched narrowband LNA

The architecture of the LNA used in the reference setup (Ref-LNA) is illustrated in Fig. 17a. It consists of a passive input noise matching network, a single active amplification device and the passive output gain matching network. Although the transistor is per se broadband, due to the frequency selective nature of the matching networks the impedance matched Ref-LNA architecture is narrowband. The input impedance Z_{in} of the narrowband Ref-LNA used in this paper is $Z_{\mathrm{in}} = 50\,\Omega$, enabling a simplified characterization and a very good noise figure [40]. For each investigated resonance frequency a dedicated configuration has been used to consider the narrowband nature of the LNAs. In all cases, a NF of 0.6 dB and a bandwidth of 3 MHz around their center frequencies was achieved.

High impedance broadband LNA

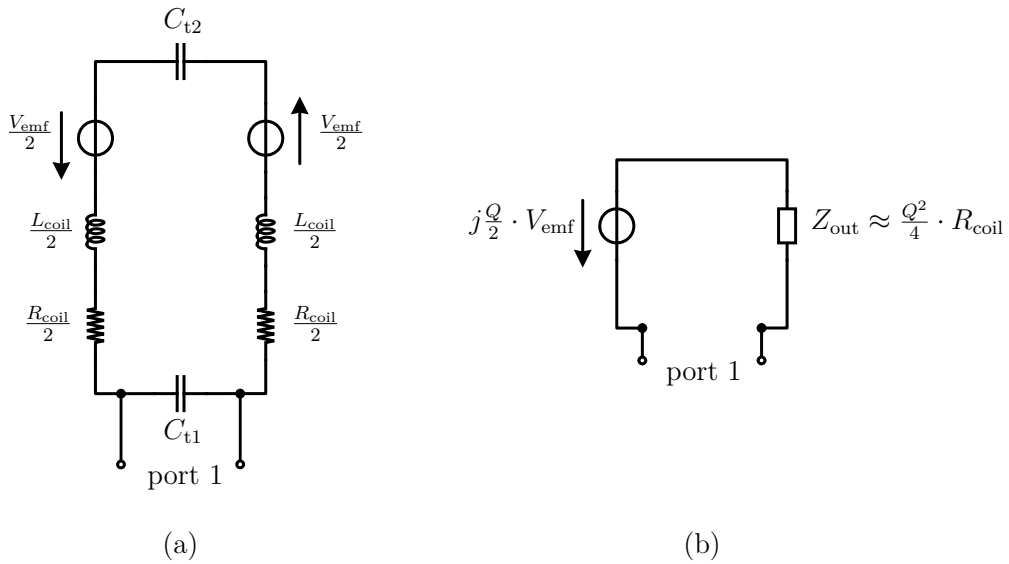

Figure 18: (b) Schematic illustration of a a split MR coil with two tuning capacitors and an induced MR voltage V_{emf}. (b) Ideal voltage source in series with an output impedance Z_{out}. Thevenin equivalent circuit of the electrical circuit illustrated in (a).

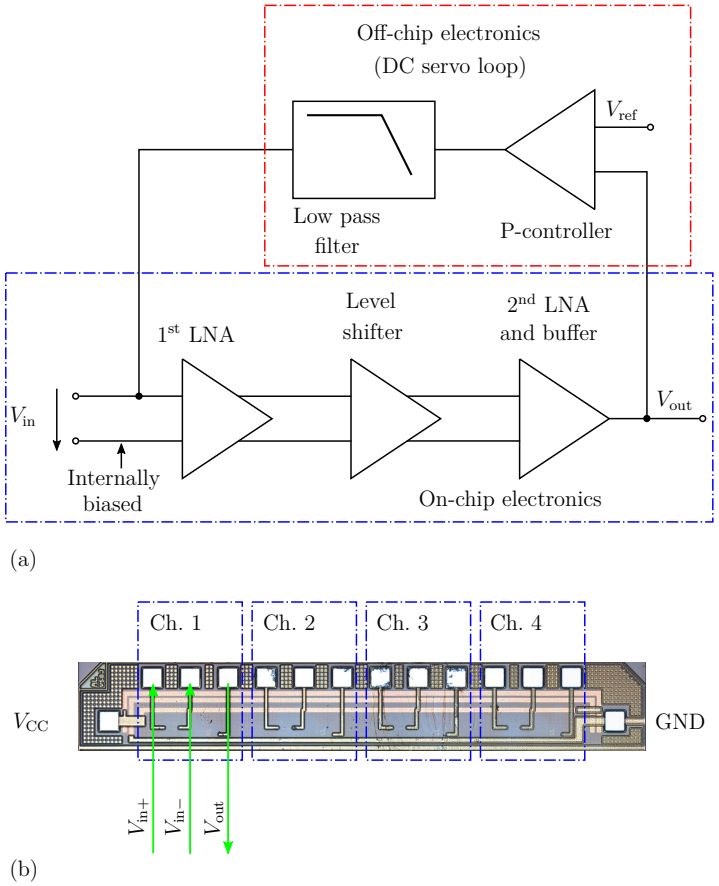

Figure 19: (a) Schematic illustration of the custom-designed high impedance broadband LNA. The components inside the blue rectangle are realized on a CMOS ASIC. (b) Micrograph of the 4-channel custom-designed LNA ASIC. Only one channel is used in this work.

To optimally exploit this additional degree of freedom in the single Rx coil case, the noise factor of a simple common source MOS LNA connected at port 1 in Fig. 18b can be considered. Assuming the drain noise to be the only noise source[1], the equivalent input resistance R_n, the equivalent noise conductance G_n, and the noise correlation admittance $Y_\mathrm{c} = G_\mathrm{c} + jB_\mathrm{c}$ are given by

$$R_\mathrm{n} = \gamma_\mathrm{nD} \cdot G_\mathrm{m}, G_\mathrm{n} = \frac{\gamma_\mathrm{nD}}{G_\mathrm{m}} \cdot (\omega C_\mathrm{GS})^2 , \tag{4.1}$$

where $G_\mathrm{c} = 0$, $B_\mathrm{c} = \omega C_\mathrm{GS}$ and γ_nD is the so-called gate noise excess factor (for a MOSFET in strong inversion and saturation $\gamma_\mathrm{nD} \approx 2/3$), ω the operating frequency, G_m the gate transconductance and C_GS the gate-to-source capacitance of the MOSFET [14]. Therefore, the optimum noise figure for such a MOSFET LNA is achieved for a source admittance with $Y_\mathrm{s,opt} = G_\mathrm{s,opt} + jB_\mathrm{s,opt}$ with $G_\mathrm{s,opt} = 0$ and $B_\mathrm{s,opt} = -\omega C_\mathrm{GS}$, resulting in a minimum noise factor of [4]

$$F_\mathrm{min} = 1 + \frac{R_\mathrm{n}}{G_\mathrm{s}} \cdot \left[G_\mathrm{s}^2 + (B_\mathrm{s} - B_\mathrm{s,opt})^2\right] = 1. \tag{4.2}$$

For the actual source admittance presented by the tuned coil with $R_\mathrm{s} = 1/G_\mathrm{s} \approx (Q_\mathrm{coil}^2/4) \cdot R_\mathrm{coil}$ and $B_\mathrm{s} = 0$, the noise factor becomes [4]

$$F = 1 + \frac{R_\mathrm{n}}{G_\mathrm{s}} \cdot G_\mathrm{s}^2 = 1 + \frac{R_\mathrm{n}}{R_\mathrm{s}} = 1 + \frac{R_\mathrm{n}}{\left(\frac{Q_\mathrm{coil}^2}{4} \cdot R_\mathrm{coil}\right)}. \tag{4.3}$$

Therefore, tuning the coil to the Larmor frequency greatly alleviates the burden on the following LNA because the intrinsic coil noise (and also sample noise) are amplified by the factor $Q_\mathrm{coil}^2/4$, allowing for a much greater value of $R_\mathrm{n} = \gamma_\mathrm{nD}/G_\mathrm{m}$ compared to the untuned case, to achieve the same noise factor (c.f. chapter 2.2.2 – *Electronically tunable/switchable RF coils*). Moreover, from the discussion above, it is clear that the simple tuning scheme is very close to noise matching for a MOSFET LNA as long as

[1] the effect of gate induced noise will be discussed later

the condition $G_s^2 \gg (\omega C_{GS})^2$ is satisfied.

Importantly, due to the location of the in-field LNA in close proximity of the MR coil and the possibility to design an unconditionally stable LNA in CMOS by simple cascoding, there is no need for power/gain matching and a simpler to achieve voltage matching is sufficient to achieve the required large LNA gain that overcomes the noise of the following mixer stage. The tuning scheme of Fig. 17 corresponds to a voltage matching, i.e. a condition where the LNA input impedance is much larger than the coil output impedance, as long as the condition $G_s \gg \omega C_{GS}$ is satisfied. This is the same condition that is required for a good noise performance close to the minimum noise factor of 1.

A direct comparison of the conventional 50 Ω LNA architecture to the proposed one reveals two major advantages of the high-impedance approach for single coil setup:

First, the noise requirements on the LNA can be greatly relaxed because, assuming even moderate coil quality factors, the impedance $(Q^2/4) \cdot R_{sample}$ (assuming sample dominated noise) is typically much greater than 50 Ω and, therefore, the corresponding (voltage) noise level V_n is much larger than that found in a 50 Ω environment. Therefore, the LNA noise figure, which is formally defined as the SNR reduction from the LNA input to its output, becomes negligible at much higher input (voltage) noise levels than in a 50 Ω environment, cf. Eq. 4.3. More specifically, the noise voltage spectral density V_n at port 1 in Fig. 17 can be written as

$$V_n = \left(\frac{Q_{coil}}{2}\right) \cdot \sqrt{4k_B T \left(R_{coil} + R_{sample}\right) \Delta f}. \tag{4.4}$$

As a point of reference, a 50 Ω environment corresponds to a noise level of approximately 0.9 nV/$\sqrt{\text{Hz}}$. Assuming a moderate quality factor of 20 and an equivalent sample resistance of 5 Ω, the boosted equivalent output impedance is 500 Ω, thus relaxing the requirement on the input LNA voltage noise by a factor of $\sqrt{Q^2/4} = Q/2 = 10$. Here, it should be noted that, depending on the active devices used in the LNA, for very large impedance levels $(Q^2/4) \cdot R_{sample}$, i.e. induced gate noise [14] can become the dominant

source of noise. The second big advantage of the high-impedance LNA is that it can be readily realized in a broadband fashion using nanometer scaled MOSFETs. These transistors provide a purely capacitive input impedance up to very high frequencies in the GHz range, which, if the devices are sized sufficiently small, results in a high LNA input impedance at all required MRI operating frequencies. This broadband high input impedance greatly facilitates X-nuclei experiments due to the absence of a narrowband, nucleus-dependent matching network. Moreover, at MRI frequencies in the tens of MHz range MOS transistors typically display very little gate induced noise, cf. [14], rendering the above drain noise only discussion accurate.

Thus, high-impedance LNAs placed in close proximity of the MR coil in combination with a simple tuning network according to Fig. 17 can provide both an excellent noise performance and the broadband capabilities necessary to perform X-nuclei MR experiments by a simple switching of said tuning network to different Larmor frequencies.

The architecture of the proposed high impedance broadband LNA is illustrated in Fig. 19a. The components inside the blue rectangle are realized on a custom-designed application specific integrated circuit (ASIC), realized in a 130 nm CMOS process. According to the figure, the on-chip electronics comprise two amplification stages and a broadband 50 Ω output buffer, requiring no external output matching network. A micrograph of this ASIC, which contains 4 identical LNA channels, is shown in Fig. 19b. Although the ASIC offers 4 identical channels for a future use with coil arrays, only one channel is used in this work. The off-chip electronics realize a DC servo loop to stabilize the DC operating points in the presence of offset voltages. The area of a single LNA channel is 300 µm × 400 µm. The input referred voltage noise of each channel is around $900\,\mathrm{pV}/\sqrt{\mathrm{Hz}}$ and the gain is about 45 dB.

The NF of the proposed setup can be measured based on its definition of $F = \mathrm{SNR}_{\mathrm{in}}/\mathrm{SNR}_{\mathrm{out}}$, where $\mathrm{SNR}_{\mathrm{in/out}}$ are the signal-to-noise ratios at the input and output of the LNA, respectively. Assuming identical gains for the signal and the noise, the noise factor can be rewritten according to $F = N_{\mathrm{out,tot}}/\left(N_{\mathrm{out,tot}} - N_{\mathrm{out,LNA}}\right)$ [53], where $N_{\mathrm{out,LNA}}$ is the measured noise power spectral density at the LNA output with zero

input. $N_{\text{out,tot}}$ is the total noise power spectral density measured at the LNA output with the coil of Fig. 17b connected to the LNA input. In this way, the measured noise factors are 1.18 (57.3 MHz and 61.0 MHz) and 1.20 (42.8 MHz). This corresponds to NFs of approximately 0.72 dB at 57.3 MHz and 61.0 MHz, respectively, and 0.79 dB at 42.8 MHz.

Measurement setup

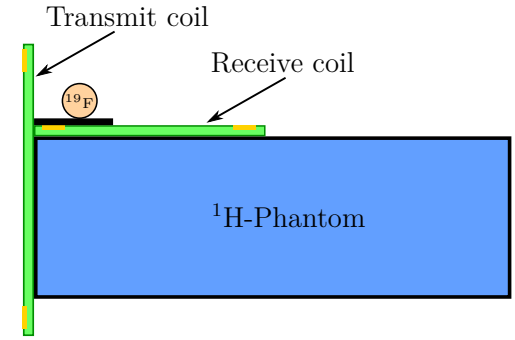

(a)

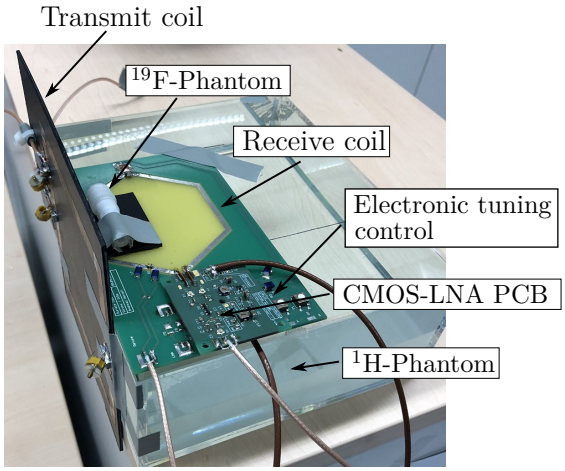

(b)

Figure 20: Illustration of the MR imaging measurement setup. (a) Schematic representation of the evaluation setup. Cuboid-shaped ^{1}H-phantom with the surface coil under test on top of the phantom. A ^{19}F-phantom is located on top of the surface coil. The transmit coil is located on the left side of the phantom. (b) Photo of the measurement setup.

A schematic illustration of the measurement setup is given in Fig. 20a. The ^{1}H-phantom is a cuboid (225 mm × 195 mm × 85 mm) made of acrylic glass, filled with $CuSO_4$ and NaCl (1 liter H_2O, 3.6 g NaCl and 1.25 g of pure $CuSO_4$). The receive coil was located on top of the cuboid-shaped ^{1}H-phantom. Due to the thickness of the Printed Circuit Board (PCB) and the wall thickness of the cuboid, the distance between the coil and the liquid was about 10 mm. Additionally, a ^{19}F-phantom was placed on top of the receive coil. It consists of pure Perfluoro-15-crown-5-ether $C_{15}F_{30}O_5$ inside a cylindrical container.

To the left of the ^{1}H phantom, a surface transmit coil was located. This coil is manually tuned and matched to the different Larmor frequencies (42.6 MHz, 57.3 MHz, 61.0 MHz) before each image acquisitions. The square coil has a size of 110 mm × 110 mm and is divided into two coil segments by the tuning capacitors. It is tuned by a PIN diode (MADP-000235-10720T, MACOM, Lowell, USA) during the excitation pulse, which is placed in series with one of the coil traces.

An image of the measurement setup is shown in Fig. 20b. Since the CMOS-LNA is a bare silicon die, it is non-magnetic, however some parts on the CMOS-LNA PCB (e.g. trimmer, DC/DC converter) are not strictly non-magnetic.

The setup has been designed such that it can be reassembled with very small positioning errors. Both, the Rx-coil of the reference setup as well as the Tx-coil were thoroughly tuned and matched before each measurement.

4.3.3 Results

Coil sensitivity maps

The coil sensitivity map has been evaluated for the two different setups and the two different field strengths, respectively. The mean and the standard deviation of the relative error between the coil sensitivity map of the reference setup and the coil sensitivity

map of the proposed digitally tuned setup were found to be less than $\mu = 0.45\,\%$ and $\sigma = 1.2\,\%$.

^{1}H and ^{19}F SNR

The results illustrated in Fig. 21 show the SNR of the coil/phantom setup of Fig. 20, measured with the reference setup and the digitally tuned setup, respectively. The images of the cuboid hydrogen phantom clearly display the sensitivity profile of the utilized surface coil, with a peak SNR of 160 close to its surface at 61.0 MHz. At a Larmor frequency of 42.6 MHz, the peak SNR is about 110 and 98 for the reference and the digitally tuned setup, respectively.
The ^{1}H image mean SNR of the reference setup within the ROI (blue square) is about 47.8 at 61.0 MHz and 32.5 at 42.6 MHz, compared to a mean SNR of about 44.5 and 29.3 measured with the newly proposed setup.
The mean SNR of the ^{19}F image within the ROI (green circle) of the reference setup is about 81.5, whereas the mean SNR of the digitally tuned setup is about 75.3.

4.3.4 Discussion

In this chapter, a novel scheme for broadband X-nuclei NMR that utilizes linear digitally controlled capacitor banks for tuning in combination with custom designed broadband, high-impedance, low noise CMOS preamplifiers was proposed. The setup allows for time multiplexed X-nuclei experiments between 34 MHz and 104 MHz with a single readout channel by switching only two (nominally identically) frequency dependent tuning elements.

The proposed architecture has been benchmarked against a conventional single-frequency 50 Ω narrowband receive chain for two different nuclei (^{1}H and ^{19}F) at two different field strengths of 1 T and 1.43 T.

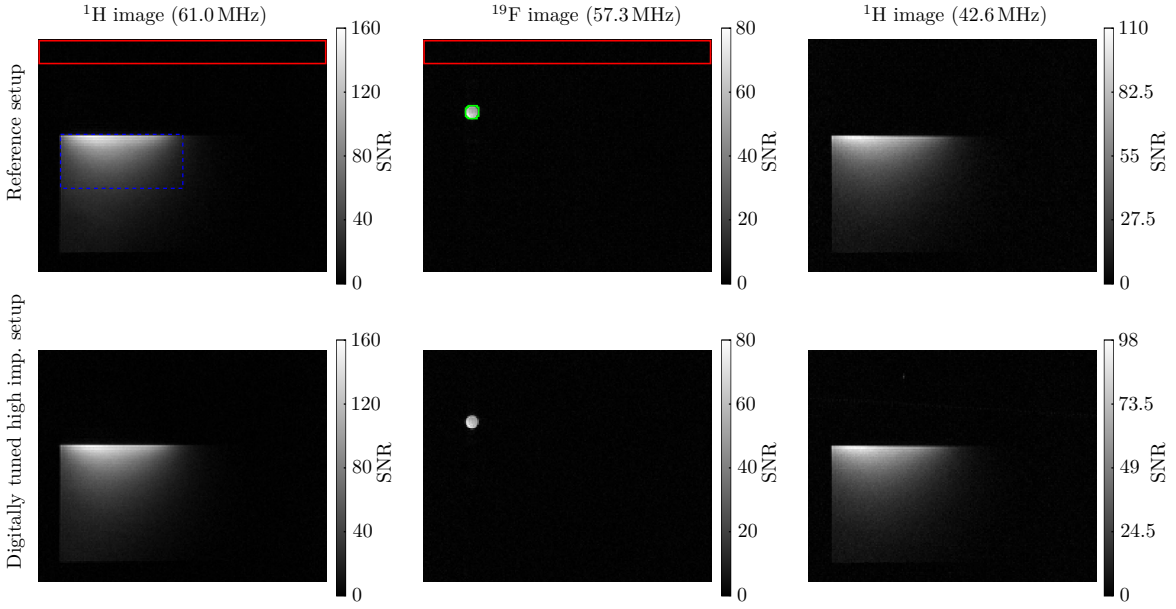

Figure 21: MR images acquired with the setup of Fig. 20 and the two different Rx chains (reference and proposed chain). Measurements have been performed at 61.0 MHz (^{1}H at $B_0 = 1.43\,\mathrm{T}$), at 57.3 MHz (^{19}F at $B_0 = 1.43\,\mathrm{T}$) and at 42.6 MHz (^{1}H at $B_0 = 1.0\,\mathrm{T}$). The signal ROIs are indicated by a blue square and a green circle, respectively. The noise ROIs are highlighted by red squares.

In these experiments the measured loaded quality factor Q of the proposed chain was found to be approximately 11 % – 13 % lower than the value measured with the reference design. This difference can be attributed to the finite series resistance of the utilized capacitor arrays and a simplified, broadband detuning scheme compared to the reference design.

The SNR performance of the digitally tuned high impedance receive chain has been compared against a state-of-the-art 50 Ω reference receive chain. In these measurements, the performance degradation was always less than 10 %. This performance loss can mostly be attributed to a lower quality factor in the proposed setup due to the Q-factor of the digitally switchable capacitor arrays, a different detune method in the proposed setup and LNA noise of our custom designed LNA. In the future, the SNR degradation of the proposed setup can be further reduced by (i) custom designing a capacitor array with a better quality factor (ii) incorporating a different detuning scheme

(possibly at the expense of a higher complexity for the X-nuclei experiments) and (iii) redesigning our custom LNA with a lower input referred noise by increasing its input transconductance.

Here, in particular the Q-factor decrease by the digitally tunable capacitors needs further investigations because it could lead to even more severe performance degradation for smaller coil loads. However, in practical applications, a surface coil is typically placed directly on the patient, which leads to significant coil loadings.

The difference between the coil sensitivity maps of the digitally tuned receive chain and the reference design is very small with a mean and a standard deviation of the relative error of $\mu = 0.45\,\%$ and $\sigma = 1.2\,\%$, respectively. This small difference can probably be attributed to positioning errors.

Apart from using the proposed setup for X-nuclei imaging, it can also be used as a general-purpose, easy-to-operate receive chain solution for different B_0-fields. Due to the use of a microcontroller for the array programming, the reprogramming can be directly implemented and triggered from the scanner control software.

4.4 High Impedance CMOS LNA with an Input Referred Voltage Noise Spectral Density of $200\,\mathrm{pV}/\sqrt{\mathrm{Hz}}$

This article [24] was published as

Horneff, A., Schlecker, B., Häberle, M., Hell, E., Ulrici, J., Rasche, V. and Anders, J. A New CMOS Broadband, High Impedance LNA for MRI Achieving an Input Referred Voltage Noise Spectral Density of $200\mathrm{pV}/\sqrt{\mathrm{Hz}}$. *IEEE International Symposium on Circuits and Systems*: 1–5, 2019

Own contribution:

Definition of the necessary LNA optimizations. Design of a schematic and a PCB which is optimized for the broadband, high-impedance preamplifier assembly. Assembly and implementation of the designed PCB. Characterization and optimization of the amplifier module. Design, construction, adaptation and implementation of the switchable X-nuclei Rx coil/receive chain. Execution of MR imaging experiments with different nuclei. Analysis and interpretation of the measured data (together with all co-authors). Collaboration in the manuscript preparation, incorporating the comments of the co-authors and incorporating the revisions.

A new CMOS broadband, high impedance LNA for MRI achieving an input referred voltage noise spectral density of $200\,\mathrm{pV}/\sqrt{\mathrm{Hz}}$

A. Horneff[1,2], B. Schlecker[4], M. Häberle[3], E. Hell[1], J. Ulrici[1], V. Rasche[2], J. Anders[4,5]
Email: jens.anders@iis.uni-stuttgart.de
[1]Sirona Dental Systems, Bensheim, Germany
[2]University Hospital Ulm, Ulm, Germany
[3]Institute of Microelectronics, University of Ulm, Ulm, Germany
[4]Institute of Smart Sensors, University of Stuttgart, Stuttgart, Germany
[5]Center for Integrated Quantum Science and Technology (IQST)

***Abstract*—In this paper, we present a new architecture for the receive-chain in clinical X-nuclei magnetic resonance imaging (MRI) experiments. The proposed architecture requires only a single tuning capacitor to tune the MRI receive coil to the Larmor frequency of the nucleus of interest. The tuning capacitor provides a noise-free preamplification of the MR signal, allowing for relaxed noise constraints in the design of the following high impedance low noise amplifier (LNA). Together with the new architecture, we present a custom designed CMOS LNA with a passband between $1.5\,\mathrm{MHz}$ and $90\,\mathrm{MHz}$, covering all clinically relevant nuclei in a $1.5\,\mathrm{T}$ MRI system. The custom designed LNA comprises two amplification stages providing a measured total gain of $44\,\mathrm{dB}$ and an on-chip DC servo loop to mitigate the effect of offsets in the presence of the large on-chip DC gain. The DC servo loop introduces a measured lower passband frequency at $1.5\,\mathrm{MHz}$. The LNA displays a measured low input referred voltage noise spectral density of $200\,\mathrm{pV}/\sqrt{\mathrm{Hz}}$. X-nuclei MRI experiments performed on proton and fluor samples demonstrate the excellent performance of the proposed architecture and LNA implementation.**

I. Introduction

Magnetic resonance imaging (MRI) is one of the prime modalities in medical diagnostics today because it offers an excellent soft tissue contrast without harmful radiation for the patient [1], [2]. In its simplest form, MRI uses the density of hydrogen nuclei, i.e. protons, and their associated nuclear spins to produce an image. In the presence of a static magnetic field, the so-called B_0-field, the energy levels of the proton spins display a distinct energy difference $\Delta E = \hbar\omega_{L,^1\mathrm{H}} = \hbar\gamma_{^1\mathrm{H}}B_0$, where $\hbar$ is the reduced Planck constant, $\omega_{L,^1\mathrm{H}}$ is the proton Larmor frequency, and $\gamma_{^1\mathrm{H}} \approx 2\pi \cdot 42\,\mathrm{MHz/T}$ is the proton gyromagnetic ratio. The MRI signal is produced by exciting the protons with a (small) resonant RF magnetic field B_1, whose frequency matches the proton Larmor frequency and recording the resulting precessing spin magnetization as an induced electromotive force (emf) in a coil. Imaging can then be performed by introducing a gradient in the B_0-field to make the Larmor frequency of the protons position dependent.

Especially over the past ten years, advances in MRI hardware have continuously improved the achievable image quality in a given imaging time and/or extended the application range of MRI. To name just a few examples, dedicated receive (RX) coils for a large variety of body parts (wrist MRI, knee MRI) have greatly reduced the imaging time to achieve a certain image signal-to-noise ratio (SNR) [4], large scale arrays of RX coils [5] have tremendously improved the achievable image quality in brain and thorax MRI and the availability of high performance multi nuclei (X-nuclei) MRI systems [3] has fostered research towards in vivo MR spectroscopy and functional ^{31}P imaging for cancer staging.

Despite the great progress in MRI hardware over the past ten years, conventional receive chains still utilize discrete transistor based low-noise amplifiers (LNAs) with their corresponding lumped element matching networks, turning the design of multi-nuclei MR systems into a relatively cumbersome task.

As a potential solution to this problem, a number of CMOS in-field receivers have been published in the literature [4]. However, despite the great additional flexibility that these systems can provide especially for the generation of receiver arrays, the realizations aiming at conventional MRI, i.e. not MR microscopy, cf. e.g. [7], [8], all employed a standard $50\,\Omega$ input impedance to be compatible with conventional MR hardware. In contrast, in this paper, we present a new broadband in-field CMOS LNA topology that makes full use of the capacitive, high impedance input provided by CMOS input devices. Moreover, by using a differential input, the proposed topology is intrinsically immune against magnetoresistive effects as well as the Hall effect that can easily deteriorate the performance of in-field single-ended LNA realizations.

Both electrical and MRI measurements demonstrate the excellent performance achievable with the proposed approach as well as its superior flexibility both for the design of simplified X-nuclei MR experiments and the formation of multi-channel receive chains.

978-1-7281-0397-6/19/$31.00 ©2019 IEEE

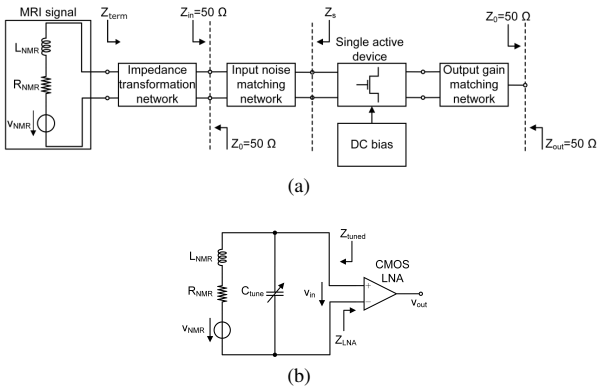

Fig. 1: (a) Conventional MRI preamplifier architecture according to [9] and (b) proposed in-field MRI preamplifier architecture.

II. LNA Architecture and Chip Realization

A. System Level Architecture

Conventional MRI preamplifiers are designed using to the architecture shown in Fig. 1a, cf. [9]. Here, a single transistor – typically a high performance, very low noise GaAs FET – is used as the sole active component and the noise figure and the gain are optimized by employing two passive matching networks – one at the input and another one at the output – around the transistor. Frequently, a third matching network is used between the MR coil and the noise matching network to either avoid standing waves on the connecting cable for a remotely located LNA ($Z_{\rm in} = Z_0 = 50\,\Omega$) or to minimize the coil current in an array of receive coils (typically $Z_{\rm in}$ small and $Z_{\rm term}$ large).The disadvantage of the architecture of Fig. 1a lies in the fact that it cannot be easily extended to X-nuclei MR experiments because each matching network displays a narrowband characteristic and a multitude of components would need to be adapted – typically including inductors – to change the operating frequency. As a solution to this problem, in this paper, we propose to use the architecture shown in Fig. 1b for the design of broadband, X-nuclei in-field MRI receive chains. In the proposed architecture, the NMR coil, $L_{\rm NMR}$ is tuned to the desired operating frequency by a single variable capacitor, which can easily be implemented by commercially available digitally programmable capacitors such as IXYS' NCD2100 (IXYS, CA, USA). The tuning capacitor provides a noise-free preamplification of both the signal and the noise level of the NMR coil by the coil's quality factor, $Q_{\rm coil} = \omega_{\rm L}\, L_{\rm NMR}/R_{\rm NMR}$, provided that the LNA input impedance $Z_{\rm LNA}$ is sufficiently larger than the boosted coil impedance $Z_{\rm tuned} = Q_{\rm coil}^2 \cdot R_{\rm NMR}$, i.e. $Z_{\rm LNA} \gg Z_{\rm tuned}$, cf. Fig. 1b. Thereby, the burden on the noise performance is greatly relaxed, because, in order to achieve a good noise figure, the input referred voltage noise of the LNA, $v_{\rm n,LNA}$ has to satisfy only the relaxed requirement of $v_{\rm n,LNA} \ll Q_{\rm coil} \cdot v_{\rm n,NMR}$, where $v_{\rm n,NMR}$ is the combined voltage noise of the NMR coil and the sample, cf. [10]. With intrinsic equivalent NMR noise resistances around $R_{\rm NMR} \approx 0.5\,\Omega$ and typical coil quality factors around $Q_{\rm coil} \approx 50$, using this approach, input referred LNA noise voltages in the range of a few $\rm nV/\sqrt{Hz}$ are required to achieve good noise figures. Another advantage of this architecture is the differential readout of the NMR coil, which renders the circuit of Fig. 1b significantly more robust against electromagnetic interference (EMI) than the single-ended architecture of Fig. 1a. Since modern CMOS technologies can provide the required input voltage noise levels, intrinsically display a relatively high impedance at the typical MRI frequencies below $130\,\rm MHz$ and ideally lend themselves to differential LNA realizations, broadband, high impedance CMOS LNAs are an ideal excellent for the LNA in the architecture of Fig. 1b.

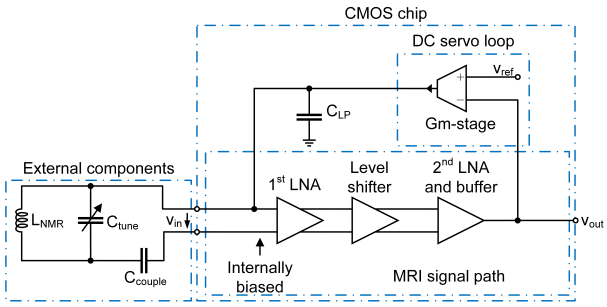

Fig. 2: Architecture of the proposed CMOS in-field MRI LNA.

B. Chip Architecture and circuit realization

The block level diagram of the proposed CMOS in-field MRI LNA to be used in the system level architecture of Fig. 1b is shown in Fig. 2. The circuit prototype has been realized in a conventional 130 nm CMOS technology. According to the figure, the proposed LNA chip consists of two gain stages which are DC coupled by an appropriate DC level shifting block. In the current realization, the signal path provides a total (DC-coupled) gain of $44\,\rm dB$ to remove the need for another gain stage before the mixer and thereby reduce the complexity when forming large scale receiver arrays. However, this large DC coupled gain makes the design susceptible to DC offsets. To mitigate this problem and still avoid the large on-chip AC coupling capacitors that would be required in view of the smallest envisioned operating frequencies around $1\,\rm MHz$ associated with low-gamma nuclei at low B_0-fields, the LNA chip contains a DC servo loop that appropriately adjusts the second input DC level of the LNA in the presence of offsets. In order to not interfere with the signal path, the bandwidth of the servo loop is kept small by using a small Gm-value to avoid large on-chip capacitances, cf. Fig.2.

The schematics of the first and the second LNA stage are shown in Fig. 3. Here, the first stage is designed for a very low input referred voltage by using a substantial bias current of $16\,\rm mA$ in the input differential pair in combination with input transistors in weak inversion (WI) and using an NMOS/PMOS current reuse technique (MOSFETs $M_{\rm n1,2}$ and $M_{\rm p1,2}$), cf. [6]. Thereby, an input referred voltage noise as low as $200\,\rm pV/\sqrt{Hz}$ is achieved in the white noise region. Moreover, the large input transistors required for operation

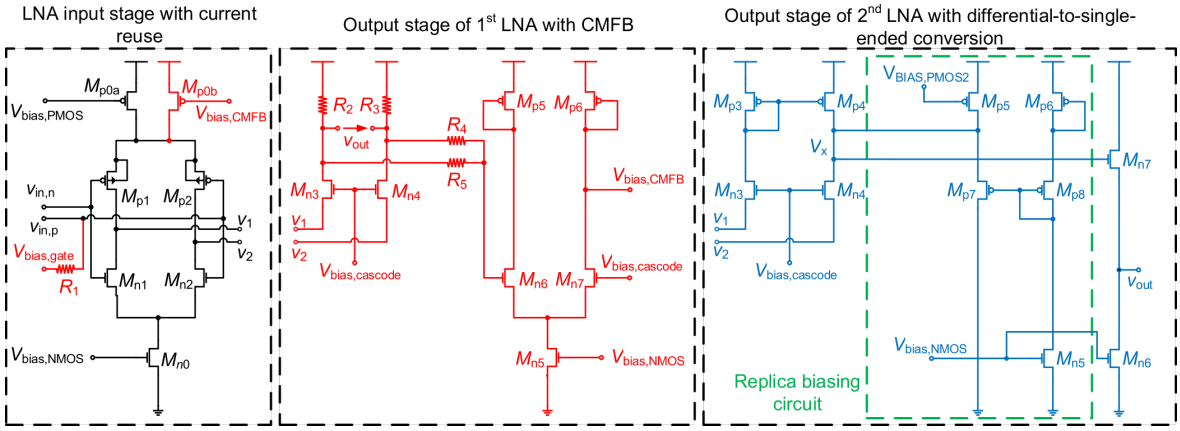

Fig. 3: Schematics of the two LNA stages. Both stages use the same input stage topology, but with scaled bias currents. The output stages differ due to the need to provide a broadband, single ended $50\,\Omega$ output in the second LNA to be compatible with conventional MRI mixers.

in WI at elevated current levels render the size of the input devices sufficiently large to produce a sufficiently small 1/f-noise corner. To avoid problems due to mismatches in the large NMOS/PMOS bias currents of the first LNA, a common mode feedback loop is used to adjust the PMOS pair bias current and ensure a proper bias current in the folded cascode branch through transistors $M_{\mathrm{n3,4}}$ and load resistors $R_{2,3}$. The first and second LNA are DC coupled by a simple source follower based level shifting circuit. The input of the second LNA utilizes the same current reuse architecture as the first LNA but at a significantly reduced bias current of $1.5\,\mathrm{mA}$, removing the need for a feedback loop to control the PMOS pair bias current. Instead, the output stage utilizes a PMOS current mirror formed by devices $M_{\mathrm{p3,4}}$ to convert the differential MR signal into a single-ended signal that is compatible with standard MRI scanner interfaces. Since the current mirror provides a too large output impedance for an open loop operation, the output voltage/the output impedance is controlled by a replica biasing circuit, cf. Fig. 3, which reduces the output impedance at node V_{x} to $\approx 1/G_{\mathrm{m,p7}}$. The required broadband output $50\,\Omega$ matching, which is needed to drive the long cable connecting the in-field LNA to the external electronics in a reflection free manner, is then provided by a two stage source follower (second stage not shown in Fig. 3).

III. Measurements

A. Electrical measurements

Before assessing the performance achievable with the proposed architecture in real MRI experiments, we have performed some electrical characterizations to validate the overall chip performance. Here, we have first measured the gain as a function of frequency using a network analyzer in combination with a 180° power splitter and a broadband (AC) $50\,\Omega$ input termination at the LNA input. In this way, we have measured a passband voltage gain of $44\,\mathrm{dB}$ from the differential LNA input into a $50\,\Omega$ load. The lower and upper passband corner frequencies were measured as $1.5\,\mathrm{MHz}$ and $90\,\mathrm{MHz}$, respectively.

The passband input referred voltage noise spectral density was then assessed by measuring the output voltage noise density using a spectrum analyzer and dividing it by the previously measured passband gain. In this way, we have measured an input referred voltage noise density of approximately $200\,\mathrm{pV}/\sqrt{\mathrm{Hz}}$, corresponding to an equivalent noise resistance of $2.4\,\Omega$ at $T = 300\,\mathrm{K}$. To minimize the LNA's input capacitance, RF pads with minimum ESD protection have been used, resulting in an LNA input capacitance of approximately $1\,\mathrm{pV}$.

An electrical assessment of the noise figure achievable in the final MRI application was performed by recalling the definition of the noise factor according to $F = \mathrm{SNR_{in}}/\mathrm{SNR_{out}}$, where $\mathrm{SNR_{in/out}}$ are the signal-to-noise ratios at the LNA input and output, respectively. Then, the noise factor can be calculated according to $F = N_{\mathrm{out,tot}}/(N_{\mathrm{out,tot}} - N_{\mathrm{out,LNA}})$, where $N_{\mathrm{out,LNA}}$ is the measured noise power spectral density at the LNA output due to the LNA only and $N_{\mathrm{out,tot}}$ is the total noise power spectral density, i.e. due to the source noise and the LNA noise. These two quantities can be assessed by measuring the LNA output with a shorted input and the external MRI coil and the additional circuitry shown in Fig. 2 connected to the LNA input, respectively. In this way, by using a tuning capacitor that tunes the input LC circuit to the different Larmor frequencies of fluor and protons at $1.43\,\mathrm{T}$, i.e. $57.3\,\mathrm{MHz}$ and $61.0\,\mathrm{MHz}$, respectively, and loading the coil with the MR phantom that was also used for the MRI experiments described in the following section, we have measured at both frequencies a noise factor of $F = 1.1$, corresponding to a noise figure of $\mathrm{NF} = 0.45\,\mathrm{dB}$. As discussed in [11], due to the large value of the LNA's input Gm and the relatively large input impedance, the LNA input noise contains both contributions from the drain noise and the so-called gate-induced noise.

In all experiments, the LNA was operated from a $1.8\,\mathrm{V}$ supply with a bias current of $30\,\mathrm{mA}$, corresponding to a power consumption of $55\,\mathrm{mW}$.

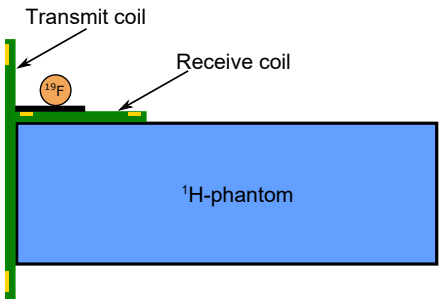

(a)

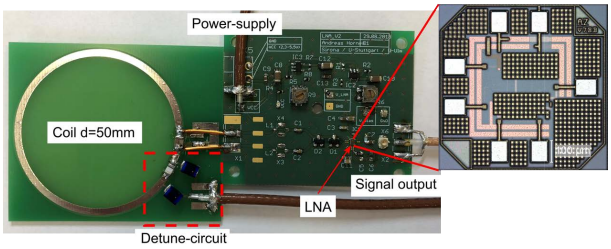

(b)

Fig. 4: (a) Experimental setup for the multinuclei MRI experiments and (b) PCB-based probe head with a micrograph of the manufactured LNA ASIC as inset.

B. MRI experiments

The multi-frequency MRI capability of the proposed CMOS LNA is demonstrated in multi-nuclei MRI experiments using the experimental setup illustrated in Fig. 4a and the PCB-based probe head shown in Fig. 4b. In this setup, the presented LNA is connected on the probe head to a planar, circular receive coil with a diameter of $50\,\mathrm{mm}$, which is in turn located on top of the ^{1}H-phantom. The ^{1}H-phantom is an acrylic glass cuboid with dimensions of $225\,\mathrm{mm} \times 195\,\mathrm{mm} \times 85\,\mathrm{mm}$ filled with $CuSO_4$ and NaCl dissolved in water (1 liter H_2O, $3.6\,\mathrm{g}$ NaCl and $1.25\,\mathrm{g}$ of pure $CuSO_4$). Due to the thickness of the PCB and the acrylic glass of the phantom, the distance between the coil and the liquid of the ^{1}H-phantom is about $10\,\mathrm{mm}$.
Above the receive coil, an additional cylindrical ^{19}F phantom is placed, which is filled with pure Perfluoro-15-crown-5-ether $C_{15}F_{30}O_5$. As shown in Fig. 4a, a separate transmit coil for the ^{19}F experiments is located to the left of the ^{1}H-phantom. All measurements have been performed on our custom built MR-Scanner with a B_0-field strength of $1.43\,\mathrm{T}$, resulting in proton and ^{19}F Larmor frequencies of approximately $57.3\,\mathrm{MHz}$ and $61.0\,\mathrm{MHz}$, respectively. The acquisition parameters of the applied gradient echo sequence (GRE) are: $T_\mathrm{E} = 5\,\mathrm{ms}$, $T_\mathrm{R} = 60\,\mathrm{ms}$, flip angle $\alpha = 12°$, $\mathrm{BW} = 100.16\,\mathrm{kHz}$, field of view $\mathrm{FOV} = 200\,\mathrm{mm} \times 200\,\mathrm{mm} \times 5\,\mathrm{mm}$ and image resolution of $1\,\mathrm{mm}$ ($200\,\mathrm{px} \times 200\,\mathrm{px} \times 1\,\mathrm{px}$).
The corresponding MR images are shown in Fig. 5. Here, Fig. 5a shows the MR image of the cuboid proton phantom. The image clearly shows the sensitivity profile of the utilized MR surface coil, displaying a peak SNR of 200 closest to its surface. Fig. 5b shows the MR image of the cylindrical fluor phantom and Fig. 5c shows the superposition of the proton and fluor images to demonstrate the proper reconstruction of the phantoms' positions in the MR images and compare the relative SNR values in a single image. Fig. 5d finally shows the proton MR image of a tangerine to demonstrate the full imaging capabilities of the proposed MR receive chain on a phantom with internal structure. The achieved SNR values in the MR imaging experiments are in very good agreement with the electrically measured noise figure.

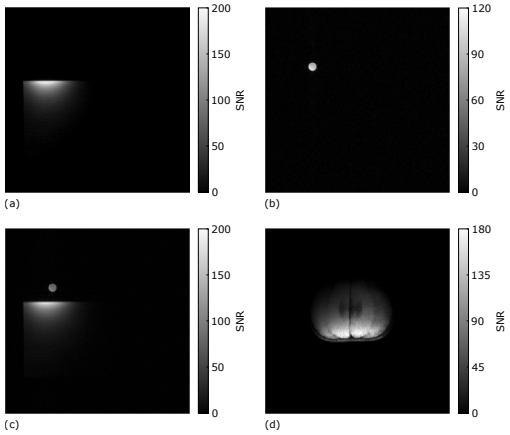

Fig. 5: (a) MR image of the proton phantom, (b) MR image of the fluor phantom, (c) superimposed MR image of the proton and fluor phantom and (d) MR image of tangerine.

IV. Conclusion and Outlook

In this paper, we have presented a new architecture for the receive chain LNA in clincial MRI that can both achieve a very good noise performance and at the same time requires only a single tunable capacitor to allow for X-nuclei MR imaging. A prototype realization of the required broadband, high impedance LNA realized in a conventional $130\,\mathrm{nm}$ CMOS technology validates the feasibility of the proposed architecture. The presented prototype displays a passband gain of $44\,\mathrm{dB}$ between $1.5\,\mathrm{MHz}$ and $90\,\mathrm{MHz}$, allowing for X-nuclei MRI in conventional $1.5\,\mathrm{T}$ clinical systems on all clinically relevant nuclei, including ^{31}P,^{23}Na,^{13}C and even ^{17}O. The measured noise figure of the presented LNA is as small $0.45\,\mathrm{dB}$, corresponding to a mere $10\,\%$ degradation in image SNR introduced by the LNA, which is comparable to state-of-the-art GaAs MRI LNAs. The large passband gain of $44\,\mathrm{dB}$ efficiently suppresses all noise from the following mixing stage and thereby removes the need for additional RF gain stages. Proton and fluor MRI experiments demonstrate the X-nuclei capabilities and the excellent achievable performance in the target application. As our next steps, we will conduct further X-nuclei MR experiments on different nuclei by designing appropriate transmit coils at the required frequencies and extend the high impedance LNA architecture to coil arrays by incorporating a suitable preamplifier decoupling network between the MR coil and the high impedance LNA.

REFERENCES

[1] A.M. Aisen et al., MRI and CT evaluation of primary bone and soft-tissue tumors, *American journal of roentgenology, 1987, vol. 146, no. 4, p. 749–756*.

[2] M. Sundaram and R.A. McLeod, MR imaging of tumor and tumorlike lesions of bone and soft tissue, *American journal of roentgenology, 1990, vol. 155, no. 4, p. 817–824*.

[3] M. Augath et al., In vivo 39k, ^{23}Na and ^{1}HMR imaging using a triple resonant RF coil setup, *Journal of Magnetic Resonance, 2009, vol. 200, no. 1, p. 134–136*.

[4] B. Sporrer et al., A Fully Integrated Dual-Channel On-Coil CMOS Receiver for Array Coils in 1.5-10.5 T MRI, *IEEE Transactions on Biomedical Circuits and Systems, 2017, vol. 11, no. 6, p. 1245–1255*.

[5] C.J. Hardy et al., 128-channel body MRI with a flexible high-density receiver-coil array, *Journal of Magnetic Resonance Imaging, 2008, vol. 28, no. 5, p. 10219–1225*.

[6] J. Anders and G. Boero, A low-noise CMOS receiver frontend for MRI, *2008 IEEE Biomedical Circuits and Systems Conference, p. 165–168*.

[7] J. Anders et al., A low-power high-sensitivity single-chip receiver for NMR microscopy, *Journal of Magnetic Resonance, 2016, vol. 266, p. 41–50*.

[8] M. Grisi et al., NMR spectroscopy of single sub-nL ova with inductive ultra-compact single-chip probes, *Scientific Reports, 7, 44670, 2017*.

[9] X. Cao et al., The design of a low-noise preamplifier for MRI, *Science China Technological Sciences, 2011, vol. 54, no. 7, p. 1766–1770*.

[10] A. Horneff et al., An EM Simulation-Based Design Flow for Custom-Built MR Coils Incorporating Signal and Noise, *IEEE Transactions on Medical Imaging, 2018, vol. 37, no. 2, p. 527–535*.

[11] J. Anders et al., A quadrature receiver for μNMR applications in 0.13 μm CMOS, *IEEE 2010 Proceedings of ESSCIRC, 2010, p. 394–397*.

5 Summarized Results

In this chapter an overview of the principal findings and specific comments of the presented topics is offered.

In the first part of this work, an Electro-Magnetic (EM) simulation based design flow for custom-built MR coils, providing an a priori prediction of the coils' sensitivity pattern ($\vec{B}_{\mathrm{u}}^{+}$- and $\vec{B}_{\mathrm{u}}^{-}$-maps) and their SNR performance, is introduced. The proposed simulation-driven design flow was validated using a manufactured prototype coil, whose performance was optimized regarding its SNR performance, based on the presented design flow by comparing the coil's measured performance against the simulated results. For simulation and the experiments, a Gradient Echo Sequenze (GRE) was used. (Here it should be noted that the approach can be used for any sequence type as long as the signal equation is known.) The echo time of the sequence was set to $T_{\mathrm{E}} = 15\,\mathrm{ms}$, the repetition time to $T_{\mathrm{R}} = 1000\,\mathrm{ms}$ and the flip angle was set to 90°.

Fig. 22a shows the measured phantom image whereas Fig. 22b shows the simulated phantom image, both normalized to relative intensities between 0 %–100 %. The corresponding SNR values are $\mathrm{SNR}_{\mathrm{sim}} = 56$ for the simulated and $\mathrm{SNR}_{\mathrm{measured}} = 54$ for the measured image. For this simulation, the thermal noise of the coil and the phantom, the attenuation of the cable between the LNA and the coil and the LNA's NF were taken into account.

The comparison of the intensity pattern of the simulated and the measured MR image was evaluated by subtracting the normalized simulated image from the normalized measured image. The resulting mean and the standard deviation of the difference between the simulated and the measured signal intensities are $\mu = 1.79\,\%$ and $\sigma = 3.15\,\%$,

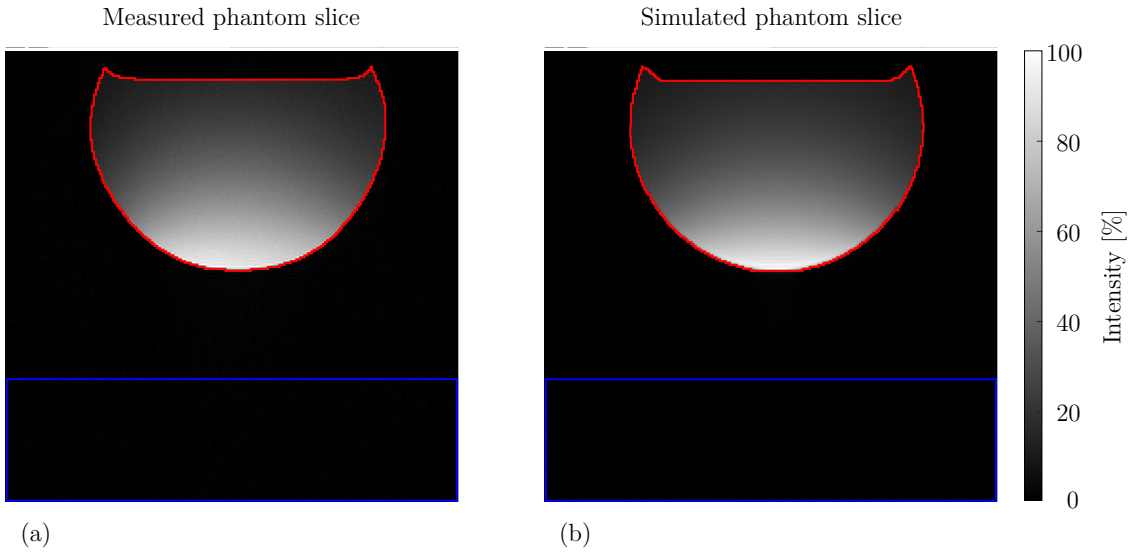

Figure 22: Measured (a) and a simulated (b) phantom slice image. The signal ROIs are indicated by a red line, the noise ROIs by blue squares, respectively. – [25], copyright © 2018 IEEE.

whereat the largest mismatches occur in the border region of the phantom, which is affected by the manufacturing tolerances of the glass phantom container.

Since custom designed and manufactured coils/receive chains can not be connected plug and play to a clinical MR system, an independent receive-only system operating in parallel to any clinical MR system has been developed. The acquisition control and sampling unit is implemented on commercially available Peripheral Component Interconnect eXtensions for Instruments (PXIe) components provided by NI (National Instruments, Austin, Texas, USA), connected to a standard computer for programming and data storage. All PXIe components of the system (Multisystem eXtension Interface cards NI-PCIe-8381 and NI-PCIe-8381, general purpose input/output card NI-PXIe-6366 and an eight channel high speed digitizer card NI-PXIe-5171R) are mounted in a NI-PXIe-1082 chassis. The programming and execution of the data acquisition process is done with LabVIEW (National Instruments, Austin, Texas, USA) and MATLAB (Mathworks Inc., Natick, Massachusetts, USA). The receive-only system can be attached to every clinical MR system without any hardware modifications. In this con-

nection, the excitation part of the sequence (RF puls, gradients, etc.) is still performed by the vendor's hardware and has thus not been considered separately.

Notwithstanding that the main intent of this system was on sampling data with minimal latency and dead time after the excitation pulse, it was used in this thesis as a simple to implement receive-only system for imaging experiments.

An an alternative realization of a multi-nuclei receive chain a adjustable RF coil in combination with a broadband, high impedance LNA is introduced. The design is based on a fast electronically switchable surface coil, equipped with digitally controllable capacitance arrays (NCD2400M, IXYS, Milpitas, USA) and a custom designed broadband, high impedance CMOS LNA. The proposed setup allows for time multiplexed X-nuclei experiments between 34 MHz and 104 MHz (which depends in turn on the geometry of the coil and the number of the used tuning elements) with a single readout channel by switching only two frequency dependent tuning elements. The custom designed broadband, high impedance LNA covers a frequency range between 1 MHz and approximately 200 MHz. The ASIC of LNA is realized in a 130 nm CMOS process. Its gain factor is around 45 dB and its input referred voltage noise is around $900\,\mathrm{pV}/\sqrt{\mathrm{Hz}}$, resulting in a measured noise figure of approximately 0.72 dB.

The performance of the proposed setup is validated in hydrogen (61.0 MHz at 1.43 T and 42.6 MHz at 1.0 T) and fluorine (57.3 MHz at 1.43 T) imaging experiments by comparing against a state-of-the-art reverence surface coil setup, which is tuned to a fix Larmor frequency in combination with a low noise figure 50 Ω LNA.

From this follows a maximum mean and standard deviation of the relative error between the coil sensitivity map of the reference setup and the coil sensitivity map of the proposed digitally tuned setup of less than $\mu = 0.45\,\%$ and $\sigma = 1.2\,\%$. The measured SNR performances of a coil/phantom setup at different Larmor frequencies ω_0 are listed at Table 3.

Because of the nonexistent matching network of the X-nuclei receive chain approach of this thesis, the impedance of the coil/sample combination directly affects the NF of the

Table 3: Resulting measured SNR values of the reference setup in combination with a narrowband 50 Ω LNA and the proposed setup including a broadband, high impedance LNA in combination with a electronically switchable coil.

	SNR_{narrow}	SNR_{broad}	Diff
Peak SNR ^{1}H ($\omega_0 = 61.0\,\mathrm{MHz}$)	110	98	10 %
Mean SNR ^{1}H ($\omega_0 = 61.0\,\mathrm{MHz}$)	47.8	44.5	7 %
Mean SNR ^{1}H ($\omega_0 = 42.6\,\mathrm{MHz}$)	32.5	29.3	10 %
Mean SNR ^{19}F ($\omega_0 = 57.3\,\mathrm{MHz}$)	81.5	75.3	8 %

LNA, according to Eq. 2.38. Therefore, in the last part of this work, the performance of the custom designed, broadband high impedance LNA was enhanced to achieve a better NF, which results in turn in a enhanced image SNR. The revised version is realized in a 130 nm CMOS process, as well. Its input referred voltage noise is reduced to around $200\,\mathrm{pV}/\sqrt{\mathrm{Hz}}$, whereas its gain is still about 45 dB. This in turn results in a measured NF of 0.45 dB.

6 Discussion and Conclusion

In this thesis, the feasibility of a broadband X-nuclei receive chain (including a X-nuclei Rx coil) to circumvent the limitations of current X-nuclei coil designs has been investigated.

As a part of this work, a simulation-driven design flow which allows to simulate the expected signal pattern as well as the image noise and thereby also the the final SNR performance of a coil in the ROI was introduced. Its applicability was validated using a self-built prototype coil, whose SNR performance was optimized based on the presented design flow by comparing the coil's measured performance against the simulated results. These measurements were performed using a dedicated stand-alone receive-only system which is based on standard industrial measurement equipment. It can be connected to any clinical MR system without any mechanical or electrical modifications required on the host system. Hereby, custom-built MR coils/receive chains can be connected and evaluated using any MR system without any restrictions concerning the vendor's connectors and protocols.

The simulation-driven design flow was validated using a manufactured prototype coil, whose SNR performance was optimized based on the presented design flow by comparing the coil's measured performance against the simulated results. The simulation of custom-made receive coils including the coil geometry, the sample tissue properties, as well as the thermal sample and coil noise were shown to be feasible, thus allowing an a priori estimation of the final MR image and its SNR for specific applications. The difference in the SNR estimation was found to be around 4 %, which may be attributed to the missing information on the NF of the sampling unit and the B_1+ non-uniformity

during Tx caused by mutual coupling into the surface coil. The difference between the simulated and the measured coil sensitivity is very small with a mean of $\mu = 1.79\,\%$ and a standard deviation of $\sigma = 3.15\,\%$. This remaining inaccuracies can be attributed to the mismatches at the border of the handmade phantom, which was not perfectly spherical. This enables the design of coils and receive chains for a dedicated application without the need for costly hardware iteration cycles, which greatly speeds up the developing process and reduces the total development costs.

Using this new simulation based design flow, the requirements towards a broadband, high impedance LNA in combination with a non resonant coil were simulated. As a start condition, a surface coil with a diameter of 60 mm and a mean sample conductivity of $\sigma_{\mathrm{avg}} = 1.0\,\mathrm{S/m}$ (cf. Fig. 15) was assumed. From this follows a required input referred voltage noise spectral density of the LNA in a range of $50\,\mathrm{pV}/\sqrt{\mathrm{Hz}}$ to $60\,\mathrm{pV}/\sqrt{\mathrm{Hz}}$ to achieve a NF between 0.4 dB to 0.5 dB in order to provide the same performance as a state-of-the-art tuned surface coil in combination with a nowadays used narrowband LNA.

Therefore, a custom designed broadband high impedance CMOS-LNA (realized in a 130 nm process) was used, which covers a frequency range between approximately 1 MHz and 200 MHz. In spite of the fact that the gain of the CMOS-LNA is about 45 dB, the input referred voltage noise spectral density of this LNA is around $900\,\mathrm{pV}/\sqrt{\mathrm{Hz}}$. This is not sufficient, since it is 18 times higher than the required input referred voltage noise spectral density.

An alternative approach towards X-nuclei imaging based on an electronic switchable coil in combination with a broadband high impedance LNA is introduced, relaxing greatly the requirements concerning the LNA's input referred voltage noise. The proposed setup may enable time multiplexed X-nuclei experiments with a single readout channel by switching only two frequency dependent tuning elements (digitally controlled capacitor banks), improving greatly the complexity of a multi-nuclei coil/receive chain. The operation frequency of the setup covers a range of 34 MHz to 104 MHz which

in turn depends on the setup and can be shifted to higher and lower frequencies by additional capacitors.

For performance evaluations, the proposed architecture has been benchmarked against a conventional single-frequency state-of-the-art 50 Ω narrowband receive chain for ^{1}H and ^{19}F nuclei at two different field strengths of 1.0 T or 1.5 T. The NF of the proposed setup was found to be approximately 0.72 dB at 57.3 MHz and 61.0 MHz, respectively, and 0.79 dB at 42.8 MHz compared to the NF of the reference setup of about 0.5 dB. Furthermore, the SNR performance degradation was found to be less than 11 %. This performance loss can mostly be attributed to a lower Q-factor of the utilized capacitor arrays, the LNA's voltage noise spectral density of $900\,\mathrm{pV}/\sqrt{\mathrm{Hz}}$ and a different detune method of the electronic switchable coil compared to the reference setup. Here, in particular, the Q-factor decrease caused by the digitally tunable capacitors needs further investigations, because it could lead to even more severe performance degeneration for smaller coil loads.

The mean and the standard deviation of the relative error between the coil sensitivity map of the reference state-of-the-art 50 Ω narrowband receive chain and the coil sensitivity map of the proposed architecture were found to be $\mu = 0.45\,\%$ and $\sigma = 1.2\,\%$. This small difference can probably be attributed to positioning errors.

As previously discussed, the input referred voltage noise spectral density of the broadband, high impedance LNA mainly affects the overall SNR performance of the presented switchable X-nuclei receive chain. Thus, the input referred voltage noise spectral density is optimized resulting in $U_{\mathrm{n,LNA}} = 200\,\mathrm{pV}/\sqrt{\mathrm{Hz}}$, corresponding to an equivalent noise resistance of 2.4 Ω at $T = 300\,\mathrm{K}$. On that account, the NF of the presented LNA in the experimental setup is as small as 0.45 dB, which is an improvement of almost 0.35 dB compared to the LNA used in the previous experiments. Due to this noise optimization, the lower and upper passband corner were measured as 1.5 MHz and 90 MHz, respectively. This in turn results in a decrease of the usable frequency range compared

to the aforementioned version of the broadband, high impedance LNA, but still covers all diagnostically relevant nuclei frequencies.

7 Bibliography

[1] Ahlbom, A ; Bergqvist, U ; Bernhardt, JH ; Cesarini, JP ; Grandolfo, M ; Hietanen, M ; Mckinlay, AF ; Repacholi, MH ; Sliney, David H. ; Stolwijk, J A. ; others: Guidelines for limiting exposure to time-varying electric, magnetic, and electromagnetic fields (up to 300 GHz). *Health physics* 74 (1998), 494–521.

[2] Anders, J. ; Handwerker, J. ; Ortmanns, M. ; Boero, G.: A low-power high-sensitivity single-chip receiver for NMR microscopy. *Journal of Magnetic Resonance* 266 (2016), 41-50.

[3] Augath, Mark ; Heiler, Patrick ; Kirsch, Stefan ; Schad, Lothar R.: In vivo39K, 23Na and 1H MR imaging using a triple resonant RF coil setup. *Journal of Magnetic Resonance* 200 (2009), 134–136.

[4] Bashore, Frank: Microwave Transistor Amplifiers: Analysis and Design. *Microwave Journal* 40 (1997), 181–182.

[5] Bernstein, M.A. ; King, K.F. ; Zhou, X.J.: *Handbook of MRI pulse sequences*. 1st edition. Amsterdam; Boston : Academic Press, 2004.

[6] Blencowe, M.: *Designing High-Fidelity Tube Preamps*. Bd. 1. Merlin Blencowe, 2016. – p. 192.

[7] Bogatin, Eric: *Signal and power integrity–simplified*. Pearson Education, 2010.

[8] Brown, R.W. ; Cheng, Y.-C.N. ; Haacke, E.M. ; Thompson, M.R. ; Venkatesan, R.: *Magnetic Resonance Imaging: Physical Principles and Sequence Design*. 2nd edition. Hoboken, New Jersey : John Wiley & Sons, Inc, 2014.

[9] C., Collins ; Z., Wang: Calculation of radiofrequency electromagnetic fields and their effects in MRI of human subjects. *Magnetic Resonance in Medicine* 65 (2011), 1470–1482.

[10] Cao, XueMing ; Zu, DongLin ; Zhao, XuNa ; Fan, Yang ; Gao, JiaHong: The design of a low-noise preamplifier for MRI. *Science China Technological Sciences* 54 (2011), 1766–1770.

[11] Caruthers, Shelton D. ; Neubauer, Anne M. ; Hockett, Frank D. ; Lamerichs, Rolf ; Winter, Patrick M. ; Scott, Michael J. ; Gaffney, Patrick J. ; Wickline, Samuel A. ; Lanza, Gregory M.: In vitro demonstration using 19F magnetic resonance to augment molecular imaging with paramagnetic perfluorocarbon nanoparticles at 1.5 Tesla. *Investigative radiology* 41 (2006), 305–312.

[12] Edelstein, WA ; Glover, GH ; Hardy, CJ ; Redington, RW: The intrinsic signal-to-noise ratio in NMR imaging. *Magnetic resonance in medicine* 3 (1986), 604–618.

[13] Eder, Michael ; Horneff, Andreas ; Paul, Jan ; Storm, Alexander ; Hell, Erich ; Ulrici, Johannes ; Anders, Jens ; Rasche, Volker: A signal acquisition setup for ultrashort echo time imaging operating in parallel on unmodified clinical MRI scanners achieving an acquisition delay of 3 µs. *IEEE transactions on Medical Imaging* 39 (2020), 218-225.

[14] Enz, Christian C. ; Vittoz, Eric A.: *Charge-based MOS transistor modeling: the EKV model for low-power and RF IC design.* John Wiley & Sons, 2006.

[15] Fitzsimmons, Jeffrey R. ; Beck, Barbara L. ; Ralph Brooker, H: Double resonant quadrature birdcage. *Magnetic resonance in medicine* 30 (1993), 107–114.

[16] Food, US ; Administration, Drug: Criteria for significant risk investigations of magnetic resonance diagnostic devices. *Rockville, MD: Center for Devices and Radiological Health, US Food and Drug Administration* (2014).

[17] Fox, Matthew S. ; Gaudet, Jeffrey M. ; Foster, Paula J.: Fluorine-19 MRI contrast agents for cell tracking and lung imaging. *Magnetic resonance insights* 8 (2015), MRI–S23559.

[18] Gareis, Daniel ; Wichmann, Tobias ; Lanz, Titus ; Melkus, Gerd ; Horn, Michael ; Jakob, Peter M.: Mouse MRI using phased-array coils. *NMR in Biomedicine: An International Journal Devoted to the Development and Application of Magnetic Resonance In vivo* 20 (2007), 326–334.

[19] Garroway, A N. ; Grannell, P K. ; Mansfield, P: Image formation in NMR by a selective irradiative process. *Journal of Physics C: Solid State Physics* 7 (1974), L457.

[20] Geddes, Leslie A. ; Baker, Lee E.: The specific resistance of biological material—a compendium of data for the biomedical engineer and physiologist. *Medical and biological engineering* 5 (1967), 271–293.

[21] Gilbert, K.M. ; Scholl, T.J. ; Chronik, B.A.: RF Coil Loading Measurements Between 1 and 50 MHz to Guide Field-Cycled MRI System Design. *Magnetic Resonance Engineering* 33 (2008), 177-191.

[22] Gruber, Bernhard ; Froeling, Martijn ; Leiner, Tim ; Klomp, Dennis W.: RF coils: A practical guide for nonphysicists. *Journal of Magnetic Resonance Imaging* (2018).

[23] Ha, Seunghoon ; Hamamura, Mark J. ; Nalcioglu, Orhan ; Muftuler, L T.: A PIN diode controlled dual-tuned MRI RF coil and phased array for multi nuclear imaging. *Physics in Medicine & Biology* 55 (2010), 2589.

[24] Horneff, A. ; Schlecker, B. ; Häberle, M. ; Hell, E. ; Ulrici, J. ; Rasche, V. ; Anders, J.: A New CMOS Broadband, High Impedance LNA for MRI Achieving an Input Referred Voltage Noise Spectral Density of $200\mathrm{pV}/\sqrt{\mathrm{Hz}}$. *IEEE International Symposium on Circuits and Systems (ISCAS)* (2019), 1–5.

[25] Horneff, Andreas ; Eder, Michael ; Hell, Erich ; Ulrici, Johannes ; Felder, Jörg ; Rasche, Volker ; Anders, Jens: An EM Simulation-Based Design Flow for Custom-Built MR Coils Incorporating Signal and Noise. *IEEE transactions on Medical Imaging* 37 (2018), 527–535.

[26] Hoult, DI: The principle of reciprocity in signal strength calculations—a mathematical guide. *Concepts in Magnetic Resonance: An Educational Journal* 12 (2000), 173–187.

[27] Hwang, F ; Hoult, DI: Automatic probe tuning and matching. *Magnetic resonance in medicine* 39 (1998), 214–222.

[28] Ibrahim, Tamer S. ; Tang, Lin: Insight into RF power requirements and B1 field homogeneity for human MRI via rigorous FDTD approach. *Journal of Magnetic Resonance Imaging: An Official Journal of the International Society for Magnetic Resonance in Medicine* 25 (2007), 1235–1247.

[29] Isaac, Gamaliel ; Schnall, Mitchell D. ; Lenkinski, Robert E. ; Vogele, Katherine: A design for a double-tuned birdcage coil for use in an integrated MRI/MRS examination. *Journal of Magnetic Resonance (1969)* 89 (1990), 41–50.

[30] J Mispelter, Jo ; Lupu, Mihaela ; Briguet, Andre: *NMR probeheads for biophysical and biomedical experiments: theoretical principles & practical guidelines.* Imperial College Press, 2015.

[31] Jin, J.: *Electromagnetic Analysis and Design in Magnetic Resonance Imaging.* Taylor & Francis, 1999 (Biomedical Engineering).

[32] Jin, Jianming ; Chen, Ji: On the SAR and field inhomogeneity of birdcage coils loaded with the human head. *Magnetic resonance in medicine* 38 (1997), 953–963.

[33] Joseph, Peter M. ; Lu, Dongfeng: A technique for double resonant operation of birdcage imaging coils. *IEEE transactions on medical imaging* 8 (1989), 286–294.

[34] Lauterbur, P.C.: Image formation by induced local interactions: examples employing nuclear magnetic resonance. *Nature* 242 (1973), 190–191.

[35] Lim, Heeseung ; Thind, Kundan ; Martinez-Santiesteban, Francisco M. ; Scholl, Timothy J.: Construction and evaluation of a switch-tuned 13C-1H birdcage radiofrequency coil for imaging the metabolism of hyperpolarized 13C-enriched compounds. *Journal of Magnetic Resonance Imaging* 40 (2014), 1082–1090.

[36] Myers, Whittier ; Slichter, Daniel ; Hatridge, Michael ; Busch, Sarah ; Mößle, Michael ; McDermott, Robert ; Trabesinger, Andreas ; Clarke, John: Calculated signal-to-noise ratio of MRI detected with SQUIDs and Faraday detectors in fields from 10 μT to 1.5 T. *Journal of Magnetic Resonance* 186 (2007), 182–192.

[37] National Electrical Manufacturers Association (NEMA): Determination of Signal-to-Noise Ratio (SNR) in Diagnostic Magnetic Resonance Imaging. *NEMA Standards Publication MS 1-2008 (R2014)* (2015).

[38] Ocali, Ogan ; Atalar, Ergin: Ultimate intrinsic signal-to-noise ratio in MRI. *Magnetic Resonance in Medicine* 39 (1998), 462–473.

[39] Pang, Yong ; Wong, Ernest W. ; Yu, Baiying ; Zhang, Xiaoliang: Design and numerical evaluation of a volume coil array for parallel MR imaging at ultrahigh fields. *Quantitative imaging in medicine and surgery* 4 (2014), 50.

[40] Reykowski, Arne ; Wright, Steven M. ; Porter, Jay R.: Design of matching networks for low noise preamplifiers. *Magnetic resonance in medicine* 33 (1995), 848–852.

[41] Roemer, Peter B. ; Edelstein, William A. ; Hayes, Cecil E. ; Souza, Steven P. ; Mueller, Otward M.: The NMR phased array. *Magnetic resonance in medicine* 16 (1990), 192–225.

[42] Slichter, C.P.: *Principles of Magnetic Resonance Imaging*. 3rd edition. Berlin : Springer, 1990. – p. 19.

[43] Stöcker, Tony ; Vahedipour, Kaveh ; Pflugfelder, Daniel ; Shah, N J.: High-performance computing MRI simulations. *Magnetic resonance in medicine* 64 (2010), 186–193.

[44] Stoy, Richard D. ; Foster, Kenneth R. ; Schwan, Herman P.: Dielectric properties of mammalian tissues from 0.1 to 100 MHz; a summary of recent data. *Physics in Medicine & Biology* 27 (1982), 501.

[45] Turner, Walker J. ; Bashirullah, Rizwan: A 4.7 T/11.1 T NMR compliant 50 nW wirelessly programmable implant for bioartificial pancreas in vivo monitoring. *IEEE Journal of Solid-State Circuits* 51 (2016), 473–483.

[46] Vaughan, J T. ; Griffiths, John R.: *RF coils for MRI*. John Wiley & Sons, 2012.

[47] Vaughan, JT ; Adriany, G ; Garwood, M ; Yacoub, E ; Duong, T ; DelaBarre, L ; Andersen, P ; Ugurbil, K: Detunable transverse electromagnetic (TEM) volume coil for high-field NMR. *Magnetic Resonance in Medicine* 47 (2002), 990–1000.

[48] Vaughan, Thomas ; DelaBarre, Lance ; Snyder, Carl ; Tian, Jinfeng ; Akgun, Can ; Shrivastava, Devashish ; Liu, Wanzahn ; Olson, Chris ; Adriany, Gregor ; Strupp, John ; others: 9.4 T human MRI: preliminary results. *Magnetic Resonance in Medicine* 56 (2015), 1274–1282.

[49] Wang, Chunsheng ; Li, Ye ; Wu, Bing ; Xu, Duan ; Nelson, Sarah J. ; Vigneron, Daniel B. ; Zhang, Xiaoliang: A practical multinuclear transceiver volume coil for in vivo MRI/MRS at 7 T. *Magnetic resonance imaging* 30 (2012), 78–84.

[50] Weber, J.: Fluctuation Dissipation Theorem. *Physical Review* 101 (1956), 1620-1626.

[51] Wiggins, Graham C. ; Triantafyllou, C ; Potthast, A ; Reykowski, A ; Nittka, M ; Wald, LL: 32-channel 3 Tesla receive-only phased-array head coil with soccer-ball element geometry. *Magnetic Resonance in Medicine: An Official Journal of the International Society for Magnetic Resonance in Medicine* 56 (2006), 216–223.

[52] Wundrak, Stefan: *Tiny golden angles and nonuniform self-gating: MRI of nonuniform motion*, Ulm University, Diss., 2016. – http://dx.doi.org/10.18725/OPARU-3963.

[53] Zwick, Albrecht ; Zwick, Jochen ; Nguyen, Xuan P.: *Signal-und Rauschanalyse mit Quellenverschiebung: elektronische Schaltungen grafisch gelöst*. Springer-Verlag, 2014.

List of Figures

List of Tables

Acknowledgments

Content from this page was removed due to privacy reasons.

Curriculum Vitae

Content from this page was removed due to privacy reasons.

Content from this page was removed due to privacy reasons.